UiT The Arctic University of Norway

Faculty of Science and Technology
Department of Physics and Technology

Optical Waveguides for Infrared Spectroscopic Detection of Molecular Gases

Marek Vlk

A dissertation for the degree of Philosophiae Doctor May 2021

This thesis document was typeset using the *UiT Thesis LaTeX Template*.

Abstract

Fields like medical diagnostics, urban and industrial environmental monitoring or basic microbiological research greatly benefit from advances in chemical and biological sensing. These applications require rapid sample analysis, reduced needs for sample handling, or good sensor network. Such demands can be met with miniaturised sensors utilising methods which secure sufficient sensitivity and selectivity. Laser absorption spectroscopy in the mid-infrared spectral domain has an excellent performance when it comes to these two figures of merit. The research community is well aware of its potential, and significant effort is being invested into reducing the size of the instrumentation to construct portable low-power laser absorption spectroscopy detectors, in particular its subclass, which utilises tuneable diode lasers. Maximum size reduction will be achieved by integrating all components onto a single chip of only few cm^2.

The integration requires to implement optical waveguides with tailored designs that can operate in the mid-infrared. Some applications demand high sensitivity, e.g. below parts per million in atmospheric sensing, which is achieved in waveguides in two ways: Long paths, and strong interaction between the light and the analyte. These are not readily satisfied with methods and characteristics of the well-developed near-infrared nanophotonics, which has opened a space for novel research. Light–analyte interaction in sensing scenarios typically happens outside of the waveguide core, the element that otherwise confines and guides light, and it needs to be increased through a diligent design. Long paths can be realised if losses in the waveguide are sufficiently low, which is yet a challenge in the mid-infrared due to limited material transparency, which is both intrinsic and residue-related, e.g. water.

The focus of this thesis is on waveguides for trace gas detection. The work mainly involved designing, processing, and characterisation of free-standing waveguides made from tantalum pentoxide (Ta_2O_5). Correct quantification of the light–analyte interaction was implemented in order to find optimal dimensions. Suitable fabrication methods were found and implemented for realising the free-standing design. This was done with fluorine-based etching of silicon from below the membrane, where the combination of the methods and Ta_2O_5 has never been explored before. Finally, an outstanding $107(2)\,\%$ interaction strength was confirmed in an experiment with the fabricated waveguides. Moreover, sensing with porous TiO_2 was explored along with this work, showing that sensing is possible within the volume of a waveguide core material too.

Acknowledgements

In this place, I would like to thank thank both my supervisors, Jana Jágerská and Astrid Aksnes, for being patient with me and supportive in overcoming the challenges in this project. And there were many. The learning curve in scientific writing was steep, but it would not be so without the Jana and Astrid. Thank you, both.

There are many more people to thank to. The rest of our group at UiT, who were setting up the laboratory. My colleagues at ORC in Southampton and at NTNU in Trondheim. This work would not be possible without you all.

All my friends, simply just for being around.

I cannot forget about Senthil Ganapathy Murugan, who taught me the first steps in waveguide fabrication during my stay in Southampton, UK. Thank you, Senthil.

Lastly, I want to thank my parents, for always being there.

Contents

List of Figures

List of Tables

1

Introduction

1.1 Trace Gas Detection with Miniaturised Sensors

In 1958, the first microchip has been manufactured. It was made of germanium and looked very improvised. Nonetheless, it revolutionised computers forever and over the course of several decades, they have been developed from room-sized machines into pocket-sized gadgets of increasing computational power. It is a great example of what miniaturisation can bring, and by far not the only technology with such potential. It will probably hardly become so wide-spread, but instruments based on tuneable diode laser absorption spectroscopy (TDLAS) are seeing a dramatic size reduction as well.

This work has been a part of projects which aim to develop miniaturised trace gas sensors with a focus on TDLAS. Although the target is on trace gases, it does in fact encompass gas detection in general. I hope this will be clear from the applications below as it is highly important to monitor gas concentrations for many reasons.

Trace gases are defined as all gases that are present in the atmosphere in concentrations below 1 %. On Earth, the atmosphere is made up of roughly 78 % nitrogen, 21 % oxygen and the rest are all trace gases. These include noble gases, with argon being the most abundant one, carbon dioxide (CO_2), methane (CH_4), and others. In particular, CO_2 and CH_4 are classified as greenhouse gases because they absorb a significant portion of the radiation incoming from the Sun. The largest greenhouse effect originates from water vapour. CO_2 is on a second place followed by ozone (O_3), and the rest comes from CH_4 and nitrous oxide (N_2O). The greenhouse effect is priceless for life on Earth—it keeps the average temperature by 33 °C higher than it would be otherwise (1). It would seem that the effects of gases other than water vapour are negligible, but the steady increase of CO_2, CH_4, and N_2O concentrations from anthropogenic sources most likely causes global warming. According to the World Meteorological Organization (WMO), the concentrations of CO_2, CH_4, and N_2O are respectively 48 %, 160 %, and 23 % higher than they were during the preindustrial era (reference year 1750) (2). This affects our environment; Sea levels are rising as the polar ice cap is melting, permafrost are thawing and releasing even more methane trapped in the soil, weather is becoming more extreme, and the list goes on. Monitoring certain gases is thus important in order to reliably model the future development and to plan the counter-actions. Miniature sensors could be implemented anywhere from remote locations like permafrosts to cities, where large amounts of CO_2, N_2O, and NO are produced, presenting risks to people's health.

Besides monitoring gases directly in the atmosphere, gas detection is of relevance to other fields such as microbiology or medical health monitoring where it allows to study metabolic processes by isotopic labelling (3; 4; 5). Some of the microbiology processes are also related to greenhouse gases. In particular, a recent study has confirmed that the bacterium *Methylocapsa Gorgona* oxidises CH_4 into CO_2. The investigation has been done by exposing the bacterium only ^{13}C-labelled methane ($^{13}CH_4$) and monitoring the production of $^{13}CO_2$. Moreover, this bacterium metabolises atmospheric CH_4, CO, and H_2 to harvest energy (6). On the other hand, some microorganisms have the ability to metabolise soil organic carbon into CH_4, and it has been shown that they adapt to different temperatures, significantly contributing to production of both CH_4 and CO_2 above 7 °C (7). Such studies are often conducted in laboratory conditions with discrete, sparse sampling due to complex gas analysis. Supplementing this kind of research with miniature sensors, which are able to operate online, would simplify the studies and potentially allowed new insights by continuous measurements.

Isotopic labelling is also used in medicine as a noninvasive diagnostic method. For example, *Helicobacter Pylori* metabolises urea into ammonia and CO_2. Administering the patient a suitable substrate enriched with a carbon isotope ^{13}C, a change in CO_2 isotope concentration can be detected in human breath and directly used as an indicator of the bacterial infection (8). Moreover, breath analysis can be also performed without isotope detection targeting different compounds. Humans exhale a number of volatile organic compounds (VOCs) (9) which can serve as bio-markers for several conditions such as diabetes, cellular damage, lung cancer, or liver cirrhosis (10).

The interest in gas detection extends beyond bacteria, humans, and even Earth. As a consequence of the definition of trace gases, different gases will conform to the it on different planets. The atmosphere of Mars composes of 96 % of CO_2, followed by argon and nitrogen and then there are trace gases topped by acetylene (C_2H_2) and further including carbon monoxide

(CO), krypton, CH_4 and more.[1] Extraterrestrial exploration has started and miniaturisation of scientific equipment is crucial for successful expeditions due to a limited cargo. Mars Curiosity rover of NASA has landed on Mars on 5 August 2012, carrying sophisticated spectroscopic instrumentation, the Sample Analysis at Mars (SAM). The SAM suite is equipped with a tuneable laser spectrometer, quadrupole mass spectrometer, and gas chromatography for analysis of the Mars atmosphere, rocks, and soils (11). Interestingly, the entire SAM suite weighs 40 kg in total.

Gas detection is further applicable in industrial process control and work environment safety. Acetylene (C_2H_2) presents combustion hazard, hydrofluoric acid (HF solution) is highly toxic in both liquid and gas phase, and CH_4 leaks in the industry are better to be avoided for economical as well as environmental reasons. Aquatic environments are receiving growing attention as gases can be dissolved in water (12; 13; 14), and it is desirable to study biological and chemical samples in their natural environments (15).

1.2 State-of-the-Art and Beyond

The motivation for (trace) gas detection is ample and so are the methods and instruments to choose from. In the closing remarks of the FLAIR2018 conference, Francesco D'Amato, general chair, noted that no method is better than the others. They all have advantages, be it resolution, specificity, size or power consumption, but they may be lacking in other ways and there are often trade-offs between the characteristics. We chose TDLAS because it allows high specificity and low limits of detection. We also see a potential for TDLAS to become smaller, and we endeavour to explore this potential.

TDLAS is readily capable of achieving extreme resolution[2] below units of ppb (parts per billion) (17). This is achieved by two means. Firstly, long optical paths directly give stronger signal by increasing the interaction volume. This is principally simple: The beam is folded between two mirrors to pass through the gas cell multiple times. Secondly, particularly strong absorption features are typically targeted. As Fig. 1.1 shows on N_2O, CH_4, and CO_2, the strongest absorption occurs between 3 and 5 µm, and e.g., the absorption coefficient of CH_4 is a 100 times higher around 3.3 µm than around 1.6 µm. This short range is just a small part of the mid-infrared (MIR) domain spanning from 2 to 20 µm. Fig. 1.1 does not reveal that the bands are composed of narrow absorption lines, which are visible in the detail of the 3.3 µm band of CH_4 in Fig. 1.2. Although there are typically some overlaps, the structure of the whole band is unique to every molecule, for which the MIR absorption spectra are called *molecular*

---

[1] It is worth to mention that Mars has only about 1 % of atmosphere of Earth in total.

[2] Also limit of detection.

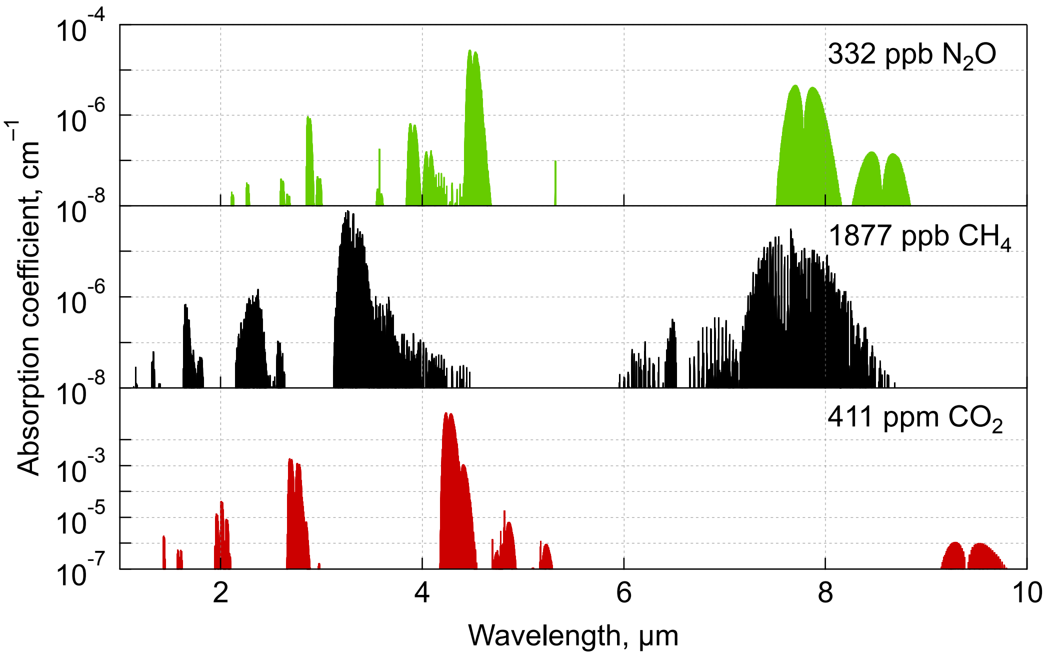

Figure 1.1: Absorption coefficient spectra of greenhouse gases CO_2, CH_4, and N_2O in their respective atmospheric concentrations as of 2019 (2). The spectra were modelled at atmospheric pressure and 20 °C with data from HITRAN (16).

fingerprints.

The MIR spectral range has become increasingly accessible in the past two decades due to the advent of quantum cascade and interband cascade laser (QCL and ICL) diodes (18; 19). There are other sources of coherent light for this wavelength range, such as gas lasers and lasers using nonlinear processes, but these can be limited to a specific wavelength or be bulky and sensitive to alignment. Diode lasers are compact, robust, and their wavelength can be engineered to match the gas absorption. Moreover, the technology has matured and allows continuous wave operation at room temperature with low power consumption below 1 W.

Currently, majority of TDLAS devices rely on navigating the beam over an open path inside a tens of centimetres long gas cell. This facilitates paths of several tens of metres but the use of the volume of the gas cell is highly inefficient (20). Large sample volumes are required to fill the volume of the cell and although they can be operated outside laboratories, their wide-scale deployment is impractical. Nevertheless, significant efforts have been under way to provide small rugged TDLAS gas sensors. The most notable one came from IBM, with a laser, an optical waveguide, and detector on a single board (21) for methane detection around 1650 nm wavelength.

Optical waveguides, building blocks of integrated photonics, are crucial in the true miniaturisation of TDLAS technology, which requires integration of all components. Waveguides confine

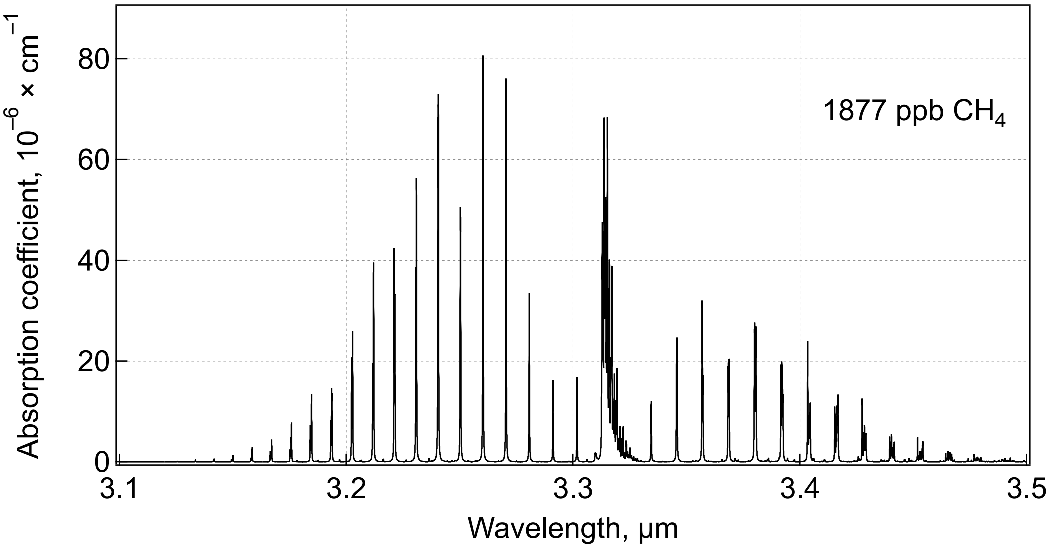

Figure 1.2: CH_4 absorption coefficient within the 3.3 µm spectral band at the atmospheric concentration as of 2019 (2). The spectrum was modelled at atmospheric pressure and 20 °C with data from HITRAN (16).

light to cross sections comparable to the wavelength of light, and guide it along predefined paths, most often within a single plane. This allows to conveniently squeeze long paths onto small footprint chips.

There is still a volume of work ahead in integrated TDLAS system development. Lasers and waveguides will eventually need to be integrated together on the same chip and the options are being extensively investigated; QCLs and ICLs are being integrated both homogeneously (22), and heterogeneously with waveguides. Homogeneous integration relies on building both components on a single substrate while heterogeneous integration requires transfer of the active device onto the same substrate as waveguides. Moreover, QCLs and ICLs usually emit at a single wavelength, which limits the spectral coverage of the envisioned devices. Attempts have been thus made in the direction of multiplexing several lasers into a single waveguide via arrayed waveguide gratings (AWG) (23). Integration of detectors is necessary as well, and other devices can potentially be added such as microfluidics and micropumps, or driving/processing electronics.

Lastly, miniature gas sensors exist but they are based on different technologies (20), and typically applicable to combustion detection, which means relatively high concentrations. Pellistors are one of the technologies but they operate at elevated temperature around 500 °C, requiring anti-explosive sealing, and suffer from a baseline drift. The latter is also a disadvantage in semiconductor devices. These, and electrochemical sensors are moreover prone to cross–response to other gases and they are affected by humidity. There has been progress towards room-temperature chemiresistive sensors (24), however, they still pose challenges in terms of gas–solid interactions, changes in semiconducting properties, and influence of ambient humidity. Particular disadvantage is a slow recovery time. Optical sensors respond faster and hence they are better suited for fast process monitoring such as combustion or burning (25).

1.3 Aim of the Thesis

The application space of TDLAS gas sensors is extensive, however, small low-cost instrumentation is still lacking. Moreover, MIR waveguides for spectroscopic applications are still in their infancy. With a miniature gas sensor in mind, the objective of the thesis has been development and characterisation of MIR waveguides. The main contributions of this thesis are summarised as follows:

- Design of optical waveguides for gas sensing in MIR with particular focus on engineering of light–matter interaction. Two designs were studied theoretically: silicon slot waveguides, and air-suspended dielectric waveguides.

- Implementation and development of processing for air-suspended optical waveguides particularly suited for gas sensing in MIR. Two dry etching methods were studied and implemented for the under-etching.

- First experimental demonstration of more than 100 % strong light–matter interaction in optical waveguides with the air-suspended design. The figure results from no other than waveguide dispersion and the field distribution in the waveguide. This effect has been predicted but never observed until this work.

In addition to the design, fabrication and characterisation, the work involved creating suitable mask designs for lithography, and in particular implementation of adiabatic curves for coupling waveguide terminals with different curvatures.

The waveguide fabrication imposed a major challenge in processing feasibility. The envisioned waveguides need to be under-etched selectively, which was not possible with the first under-etching method tested. Two ways of solving this challenge were found.

It was found during this work that the MIR photonics is strongly limited by material transparency. Although there is a range of materials with no intrinsic losses in parts of the MIR range, the transparency can be strongly affected by impurities in the materials, such water in oxides. Water was in fact identified as the main contributor to propagation loss around 3 µm wavelength.

1.4 Structure of the Thesis

The thesis is organised so as to provide the necessary understanding of the results presented herein and mainly in the appended publications.

In the first chapter, the focus is on optical waveguides fundamentals. Electromagnetism, captured in Maxwell equations, applied on optical waveguides allows to analytically find the optical field distribution in very basic systems, and it can be qualitatively extended to more complex waveguide geometries. Then, fundamentals of molecular absorption spectroscopy are given to clarify the origin of the molecular fingerprints. Moreover, absorption saturation is explained, showing its relevance to the waveguide-based spectroscopy because of the high light intensities occurring in waveguides.

The following chapters are then concerned with methods behind this work. First, it is a waveguide modelling in chapter 3, followed by a brief summary of fabrication methods in chapter 4, and finally waveguide characterisation and mainly TDLAS experimental details in chapter 5.

1.5 Publications

The research is captured in three papers that were finalised towards the end of this work. The laboratory at UiT, where most characterisation was done, was being established during my PhD period. Publishing was therefore not possible until the experiments were well-understood, which happened thanks to a good work of our group. I did all fabrication in nanofabrication foundries at the Optoelectronics Research Centre (ORC) in Southampton, UK, and at Nanolab, NTNU, Trondheim, Norway during my research stays in these places.

The first paper reports on the spectroscopy performance of the free-standing Ta_2O_5 waveguide. Model of the waveguide predicted very high light–analyte interaction strength of 107 % and we confirmed this figure in an experiment by detecting a known concentration of acetylene.

Paper I: M. Vlk, A. Datta, S. Alberti, H. D. Yallew, V. Mittal, G. S. Murugan, and J. Jágerská, "Extraordinary Evanescent Field Confinement Waveguide Sensor for Mid-Infrared Trace Gas Spectroscopy," *Light: Science & Applications*, Vol. 10(1), p. 26, 2021.

Author contributions: J.J. conceived the idea and together with G.S.M. designed the research. M.V. simulated and fabricated the waveguide sensor and performed loss characterisation. V.M. conducted the membrane under-etching. A.D., H.D.Y., and S.A. constructed the setup, and A.D. performed all spectroscopic measurements. J.J. supervised the work, while G.S.M. led the fabrication. M.V. and J.J. mainly wrote the paper. All authors reviewed the manuscript and provided editorial input.

We explored the possibility of gas detection in a waveguide core, which is a subject of the second paper. TiO_2 device layer was prepared by the sol-gel process, and it was deliberately porous, in order for the gas to diffuse in.

Paper II: S. Alberti, A. Datta, M. Vlk, and J. Jágerská, "Single-Mode Porous Waveguides through Sol-Gel Chemistry: A New Platform for Gas Sensing," *Optics Letter*, submitted

Author contributions: S.A. conceived the idea, designed the waveguide, processed and characterised the porous material, and performed loss characterisation. A.D. and M.V. designed the mask. M.V. contributed to the waveguide processing. A.D. and S.A. constructed the setup, and performed spectroscopic measurements. J.J. supervised the work. S.A. mainly wrote the paper. All authors reviewed the manuscript and provided editorial input.

The third and last paper presents the methodology of free-standing waveguide fabrication. We compared two approaches to the under-etching, namely XeF_2 molecular gas and SF_6 plasma. Although both can be used, there are significant differences, and we identified the latter as more suitable.

Paper III: Marek Vlk, Anurup Datta, Sebastián Alberti, Ganapthy Senthil Murugan, Astrid Aksnes, and Jana Jágerská, "Free-Standing Waveguides for Sensing Applications in the Mid-Infrared," *Optical Materials Express*, submitted

Author contributions: M.V. simulated, fabricated, and characterised the waveguide. A.D. contributed to material characterisation. S.A. prepared the sol-gel material. J.J. conceived the idea and together with G.S.M. designed the research. J.J., G.S.M., and A.A. supervised the work. M.V. mainly wrote the paper. All authors reviewed the manuscript and provided editorial input.

2

Background

This chapter covers the fundamental theory behind this thesis. It opens with the elementary building block of integrated optics, that is optical waveguides, and follows with an introduction into molecular spectroscopy.

2.1 Optical Waveguides

Optical waveguides confine light and guide it along predefined paths. In order to analyse the operation, it is illustrative to first consider ray tracing. Then, a more rigorous approach will be taken though electromagnetism, which is crucial for elaborating on some theory later on. The electromagnetic field distribution in waveguides is unique and susceptible to interfaces between materials. This will be illustrated on planar waveguides first and then expanded to other, more intriguing, waveguides geometries. With the fundamental theory of waveguides provided, it is imperative to introduce light–matter interaction and its quantification via a confinement factor. Propagation losses are an integral part of optical waveguides and they are thus given space in this section as well. In particular, material loss, lateral leakage in rib waveguides, and substrate leakage were identified as the most concerning contributors in this work.

2.1.1 Planar Waveguides

2.1.1.1 Total Internal Reflection – The Simple Picture

The operation principle of optical waveguides can be understood by ray tracing. The most simple waveguide one can imagine is likely a planar waveguide formed of two parallel mirrors. The light is reflected back and forth between the two mirrors and effectively only propagates within the plane. There is an important condition, which the light has to obey; After every single roundtrip between the mirrors, the light wave has to interfere constructively with itself. In other words, the phase shift experienced by the wave has to be an integer multiple of 2π. Assuming a single monochromatic wave, this gives rise to a discrete finite set of modes. This simple guiding effect has been leveraged for example in hollow-core fibres (26; 27) or hollow waveguides (28; 29). Nevertheless, it is more important for this work to elaborate on dielectric waveguides rather than guiding with mirrors.

A dielectric planar waveguide is formed of layers of different refractive indices as shown in Fig. 2.1. Light guiding requires that the light is confined to the core region, which is consistent with total reflection. From the *Snell's law*

$$n_1 \sin(\theta_1) = n_2 \sin(\theta_2), \tag{2.1}$$

where θ_1 is the angle of incidence, and θ_2 the angle of refraction, one can infer that the condition for total reflection is

$$\sin(\theta_c) = \frac{n_2}{n_1} \tag{2.2}$$

for $n_2 > n_1$ with θ_c being the critical angle. In a dielectric slab, the total reflection needs to take place on both the top and bottom interfaces, and we speak of *total internal reflection*. For the refractive indices, this means that the core refractive index has to be larger than those of the surrounding media (see Fig. 2.1), mathematically $n_c > \max\{n_{tc}, n_{bc}\}$. Again, the plane waves have to interfere constructively after completing a roundtrip, which is schematically shown in Fig. 2.1. This self-consistency condition is given by the phase shift $2k_y a \cos\theta$ acquired by the wave during a roundtrip plus a shift ϕ_r due to reflections

$$2k_y \cos\theta - 2\phi_r = 2\pi m, \tag{2.3}$$

where m is an integer, and has a meaning of the mode order with $m = 0$ marking a fundamental mode. Therefore, the guided modes have to obey two conditions given by eq. (2.2), wherein $n_f > \max\{n_s, n_c\}$, and (2.3). The result is again a finite discrete set of modes due to (2.2). Importantly, just like bulk media are characterised by a phase refractive index, guided modes are characterised by an effective index n_{eff} or propagation constant β as

$$\beta_m = n_{eff,m} k_0 = n_1 k_0 \cos\theta_m. \tag{2.4}$$

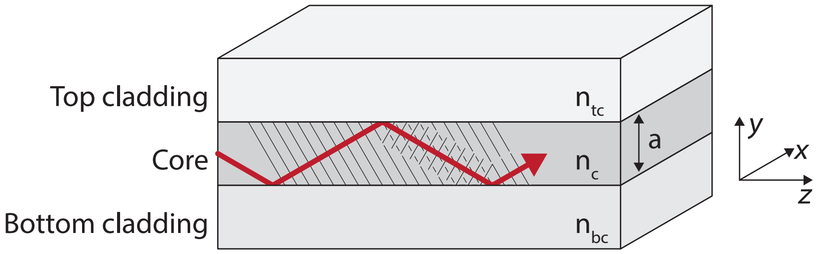

Figure 2.1: Schematics of a planar waveguide with a beam following a zig-zag path within the core region. Lines perpendicular to the beam designate planes of equal phase.

The propagation constant is basically the z component of the wave vector. Finally, the number of guided modes, each labelled with an integer m, depends on dimensions and refractive indices. Once the propagation constant value becomes smaller than phase velocities in the claddings, kn_bc and kn_tc, it will radiate out from the waveguide. This is called the cut-off condition:

$$\beta = k_0 \max\{n_{bc}, n_{tc}\}. \tag{2.5}$$

In addition, each mode is characterised by their field distribution within the waveguide, which does not follow from ray tracing. Therefore, the next section deals with basics of electromagnetism in order to understand the field distribution in waveguides.

2.1.1.2 Electromagnetic Optics – The Rigorous Picture

Electromagnetism reveals more about optical waveguides than ray tracing. The two independent polarisations of light come naturally out of the Maxwell equations when dealing with planar waveguides, and it is easily shown that the guided modes have sinusoidal field profiles over the core, followed by an evanescent tail in the claddings. The latter is particularly important in optical sensing.

It is sufficient for this thesis to consider only *dielectric*, *nonmagnetic*, and *isotropic* media. The current density $\mathbf{J}$ and charge density ρ are therefore zero, the permeability μ is equal to that of vacuum ($\mu = \mu_0$), and the permittivity ϵ is only a scalar function of position ($\epsilon = \epsilon(\mathbf{r})$). With respect to *homogeneity* of materials, the discussion will be more general, even though the only non-homogeneity is represented by a step change in ϵ across an interface of two materials. With these simplifications, the Maxwell equations read

$$\nabla \times \mathbf{H} - \epsilon \frac{\partial \mathbf{E}}{\partial t} = 0, \tag{2.6}$$

$$\nabla \times \mathbf{E} + \mu_0 \frac{\partial \mathbf{H}}{\partial t} = 0, \tag{2.7}$$

$$\nabla \cdot \mathbf{E} = 0, \tag{2.8}$$

$$\nabla \cdot \mathbf{H} = 0. \tag{2.9}$$

where **H** is a magnetic field intensity, and **E** an electric field intensity.

As mentioned above, the electromagnetic treatment of light allows to determine field distributions in the planar waveguide (Fig. 2.1). It is trivial to show that the first two of Maxwell equations can be decoupled into two independent triplets of field components. The system is homogeneous in x direction, which implies $\partial/\partial x = 0$ for plane waves. With this observation, it remains that components E_x, H_y, and H_z depend on each other but not the other three. This is the transverse electric (TE) polarisation. In the same manner, components H_x, E_y, and E_z are coupled together and comprise the transverse magnetic (TM) polarisation. The field distributions for monochromatic plane waves with phase $\phi = i(\beta z - \omega t)$ are captured in

$$\frac{\partial^2 \mathrm{E}_x}{\partial y^2} - \left[\beta^2 - \epsilon_r \left(\frac{\omega}{c}\right)^2\right] \mathrm{E}_x = 0 \tag{2.10}$$

and

$$\frac{1}{\epsilon_r}\frac{\partial}{\partial y}\left(\epsilon_r \frac{\partial \mathrm{H}_x}{\partial y}\right) - \left[\beta^2 - \epsilon_r \left(\frac{\omega}{c}\right)^2\right] \mathrm{H}_x = 0 \tag{2.11}$$

respectively. These are actually wave equations for the particular components E_x and H_x, where the time and z dependence was factored out, otherwise known as Helmholtz equations. Remaining field components can be obtained from Maxwell equations (2.6) and (2.7).

The solutions to equations (2.10) and (2.11) can be found in many textbooks. Depending on the factor $[\beta^2 - \epsilon_r(\omega/c)^2]$, the solutions are either harmonic for $\beta^2 < \epsilon_r(\omega/c)^2$ or exponential for $\beta^2 > \epsilon_r(\omega/c)^2$ functions. But the condition on the oscillatory solutions is actually the cut-off condition (2.5) discussed in the ray optics approach, while exponential solutions are obtained in cladding regions. The latter could be both exponential decay and growth if boundary conditions are imposed. It can be shown that electromagnetic field at interfaces has to obey (30)

$$\mathbf{n} \cdot (\epsilon_{r2}\mathbf{E}_2 - \epsilon_{r1}\mathbf{E}_1) = 0, \tag{2.12}$$

$$\mathbf{n} \cdot (\mathbf{H}_2 - \mathbf{H}_1) = 0, \tag{2.13}$$

$$\mathbf{n} \times (\mathbf{E}_2 - \mathbf{E}_1) = 0, \text{and} \tag{2.14}$$

$$\mathbf{n} \times (\mathbf{H}_2 - \mathbf{H}_1) = 0, \tag{2.15}$$

where the indices 1 and 2 refer to two different media, and the fields are taken at the interface. These conditions require that the field only decays into claddings, forming the *evanescent field*. An example in Fig. 2.2 shows a model which supports just 3 TE modes: The fundamental TE_0, first-order TE_1, and second-order TE_2 mode. The harmonic and evanescent parts can be clearly distinguished. The mode order m is equal to the number of nodes of the harmonic component. Note that can be stated for E_x and H_y but not for H_z because $H_z \propto \partial E_x/\partial y$, and it therefore contains $m + 1$. The results for TM modes are similar.

It can be further seen that all components of TE polarisation are continuous across the interface in the configuration of Fig. 2.1. The situation in TM polarisation is, however, quite

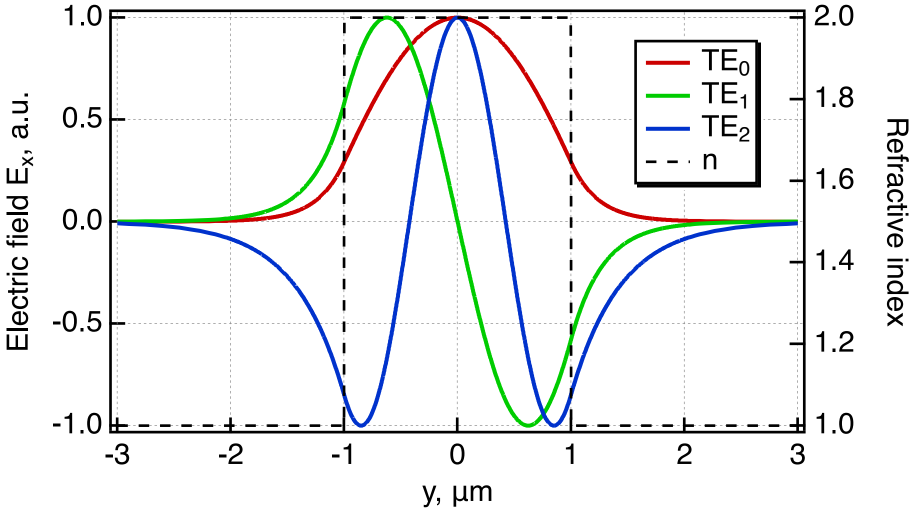

Figure 2.2: A numerical model of a planar waveguide supporting just 3 TE modes. The core with refractive index 2 is surrounded by air claddings ($n = 1$), thickness is set $a = 2$ µm, and wavelength is 2.5 µm

different. H_x and E_z are continuous according to (2.14) and (2.15) respectively, but E_y has a discontinuity because of the step change in ϵ_r as captured in (2.12). Electric field profiles of both TE and TM polarisations in a planar waveguide, obtained by a finite difference method (MODE, Lumerical), are plotted in Fig. 2.3 for comparison. This is an important result for certain waveguide geometries as will be shown later.

Guided modes are thus characterised by oscillatory profiles in the core, high refractive index region, and evanescent tail in the claddings. Planar waveguides are simple and can be solved analytically but they are not so practical in majority of applications. Rectangular and other geometries are far more common, and they will be qualitatively discussed in the next section.

2.1.2 Rectangular and Other Waveguide Geometries

Firstly, pure TE and TM polarisations are not supported by other than planar waveguides. This is easy to understand considering that a rectangular waveguide has four sides, such as the examples in Fig. 2.4, and boundary conditions (2.12)–(2.15) have to be fulfilled simultaneously. This can only only happen if all 6 components of the electromagnetic field are excited in each mode. Nevertheless, modes of rectangular waveguides usually have one dominant polarisation fraction and we speak of quasi-TE and quasi-TM modes. This notation is often omitted and the modes are simply called TE and TM modes instead. Higher order modes are possible, and there are in fact two numbers labelling the order, say m and n with the mode notation being $\mathrm{TE}_{\mathrm{mn}}$.

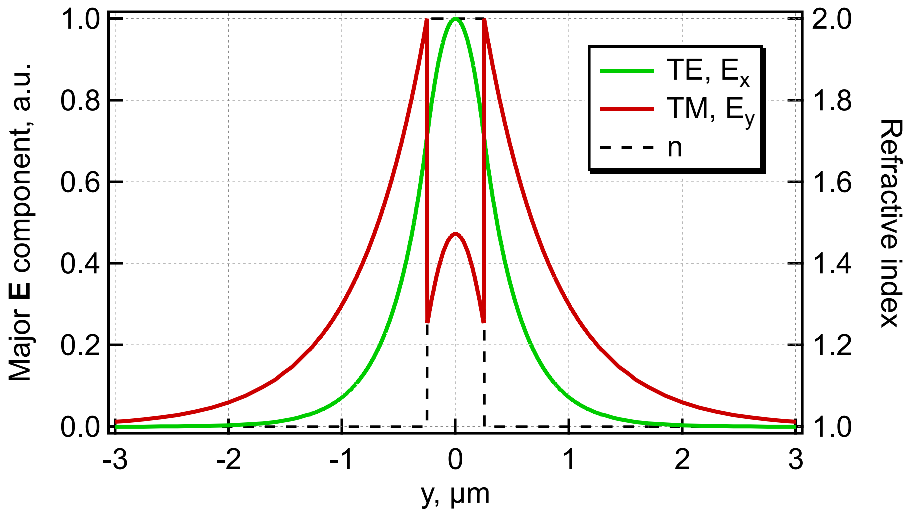

Figure 2.3: Simulated field profiles of the two orthogonally polarised modes in a planar waveguide. The parameters are a =500 nm, λ =2500 nm, $n_c = 2$, and $n_tc = n_bc = 1$.

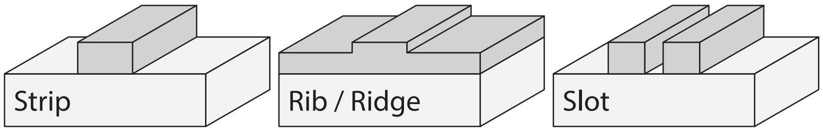

Figure 2.4: Schematics of selected rectangular waveguides.

The analytical treatment of rectangular waveguides is a little more complicated compared to the planar waveguide and requires some approximations.[1] This is done via the *Marcatili's method* or *Effective index method*, but both have some limitations as to the situations they can be applied to (31). Similarly, waveguides with graded refractive indices are solved under some approximations. Nowadays, these approaches are obsolete because of the available computational power. It is far more beneficial to use rigorous methods like the finite difference method (FDM) or the finite element method (FEM) with a sufficiently fine mesh.

Field distributions of fundamental modes TE_{00} and TM_{00} in waveguides of Fig. 2.4 are shown in Fig. 2.5. They were modelled with FDM-based solver (MODE, Lumerical), and the fields exhibit patterns we saw in planar waveguides. Field discontinuities discussed in the previous section (see Fig. 2.3) are apparent in those modes which have a major **E** field component perpendicular to the interface. This is valid for both TE and TM polarisations of the strip waveguide, while it is more pronounced only in the TM_{00} and TE_{00} modes of the rib and slot waveguides respectively. This has important implications for achieving efficient light–matter interaction in gas sensing as discussed in Papers I and II.

Other specific waveguide types exist besides waveguides which are invariant in the direction of propagation z, such as those discussed until now. Photonic crystals, materials with a periodically

---

[1] We are still talking only about examining modes of waveguides, and not about solving light propagation.

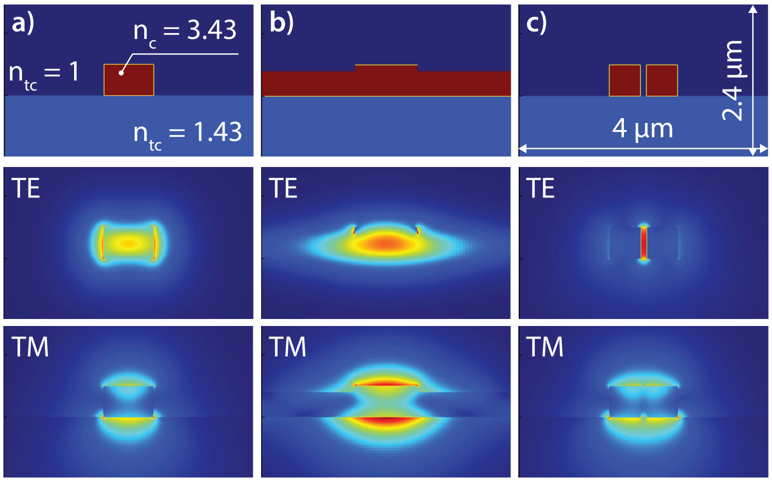

Figure 2.5: Field distributions of fundamental modes of different rectangular waveguides introduced in Fig. 2.4. The images show $|\mathbf{E}|^2$ in both orthogonal polarisations of the rectangular **(a)**, rib **(b)**, and the slot waveguides **(c)**.

modulated permittivity, can achieve guiding along defects (32), and subwavelength gratings act as effective media, which do allow light confinement (33). They are of great interest in integrated optics but further discussion is outside the scope of this thesis.

2.1.3 The Confinement Factor

The confinement factor, labelled with Γ, is a measure of the light–matter interaction. While a beam in a non-dispersive medium has Γ of $100\,\%$, the situation in optical waveguides is not straightforward. Originally it was a source of some confusion (34): Waveguide modes partly occupy different media which can exhibit gain or loss. Researchers have used either power or **E** fraction to quantify the modal gain or loss but it is not a correct measure. Unfortunately, this still happens in some cases and e.g., Ranacher *et al.* (35; 36) have used the power fraction repeatedly in recent years despite of the confinement factor being introduced in 1997 (34). Although it was initially discussed mainly in the context of gain media, the optical sensing community started adopting it too.

Confinement factor can be defined as proportionality constant between a modal loss α_m and bulk loss α_i coefficients as

$$\alpha_m = \sum_i \Gamma_i \alpha_i \tag{2.16}$$

where Γ_i is the confinement factor, and i runs over all the materials constituting the waveguide, that is the core, the cladding, and potentially others. The task is therefore to determine the correct expression for Γ.

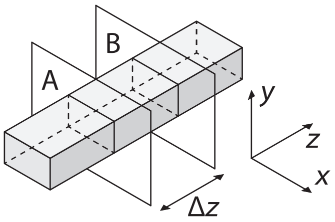

Figure 2.6: Schematics of a waveguide for determination of the confinement factor. Integrations in the Poynting theorem are done over the section restricted by planes A and B.

Visser *et al.* have derived Γ from the Poynting theorem

$$\iint_S (\mathbf{E}\times\mathbf{H})\cdot\mathbf{n}dS = \iiint_V (j\omega\epsilon^*\mathbf{E}\cdot\mathbf{E} - j\omega\mu\mathbf{H}\cdot\mathbf{H})dV, \tag{2.17}$$

which relates the power passing through a surface S to the energy density in a volume V enclosed by S. A guided mode propagating in the z direction is given as

$$\{\mathbf{E},\mathbf{H}\}(x,y,z) = \{\tilde{\mathbf{E}},\tilde{\mathbf{H}}\}(x,y)\exp[-j\beta z] \tag{2.18}$$

where $\beta = \beta' - j\beta''$ is a complex propagation constant related to the modal absorption coefficient:

$$\alpha_m = 2\mathrm{Im}\{\beta\}. \tag{2.19}$$

For a guided mode in the system pictured in Fig 2.6, the surface integral in (2.17) reduces to

$$-\iint_A (\mathbf{E}\times\mathbf{H}^*)\cdot\mathbf{e}_z dxdy + \iint_B (\mathbf{E}\times\mathbf{H}^*)\cdot\mathbf{e}_z dxdy \tag{2.20}$$

Recognising that the factor $\mathbf{E}\times\mathbf{H}^*$ decreases as $\exp[-\alpha_m\Delta z]$, (2.20) further simplifies to

$$\iint_A (\mathbf{E}\times\mathbf{H}^*)\cdot\mathbf{n}dS = (\exp[-\alpha_m\Delta z]-1)\iint_A (\tilde{\mathbf{E}}\times\tilde{\mathbf{H}}^*)\cdot\mathbf{e}_z dS. \tag{2.21}$$

With the expression (2.18) for fields, the volume integral in (2.17) can be integrated in z, yielding

$$\begin{aligned} j\omega\iiint_V (\epsilon^*|\mathbf{E}|^2 - \mu|\mathbf{H}|^2)dV &= j\omega\int_0^{\Delta z}\exp[-\alpha_m z]dz\iint_A (\epsilon^*|\tilde{\mathbf{E}}|^2 - \mu|\tilde{\mathbf{H}}|^2)dxdy \\ &= \frac{j\omega}{\alpha_m}(\exp[-\alpha_m\Delta z]-1)\iint_A (\epsilon^*|\tilde{\mathbf{E}}|^2 - \mu|\tilde{\mathbf{H}}|^2)dxdy, \end{aligned} \tag{2.22}$$

where the limits of integration over z can be chosen arbitrarily. Combining (2.17), (2.21), and (2.22), gives

$$-\alpha_m\iint_A (\mathbf{E}\times\mathbf{H}^*)\cdot\mathbf{e}_z dS = j\omega\iint_A (\epsilon'|\tilde{\mathbf{E}}|^2 - \mu|\tilde{\mathbf{H}}|^2)dxdy - \omega\iint_A \epsilon''|\tilde{\mathbf{E}}|^2 dxdy. \tag{2.23}$$

Equation (2.23) relates the modal absorption coefficient to the distribution of the electromagnetic field of the mode and the material constants, ϵ and μ. Recalling relation (2.16), this is only one step away from expressing Γ. For the modal absorption coefficient, we get

$$\alpha_m = \frac{\omega \iint_A \epsilon'' |\tilde{\mathbf{E}}|^2 dxdy}{\mathrm{Re}\{\iint_A (\tilde{\mathbf{E}} \times \tilde{\mathbf{H}}^*) \cdot \mathbf{e}_z dxdy\}}. \tag{2.24}$$

This equation is a useful tool for calculating the waveguide mode loss/gain from the field distribution. Visser *et al.* (34) have not derived the general confinement factor formula but presented it for special cases of planar waveguide modes. To obtain Γ_i, one only needs to compare (2.24) to a beam propagating in a bulk of a material, where the loss is given as $\alpha = 2n''k_0$. Adding that permittivity can be written as a product of a relative and a vacuum permittivity, $\epsilon = \epsilon_r \epsilon_0$, and that $\epsilon_r = (n' - jn'')^2$, we get $\epsilon_r'' = 2n'n''$, and (2.24) can be rewritten as

$$\alpha_m = 2k_0 c\epsilon_0 \frac{\iint_A n'n'' |\tilde{\mathbf{E}}|^2 dxdy}{\mathrm{Re}\{\iint_A (\tilde{\mathbf{E}} \times \tilde{\mathbf{H}}^*) \cdot \mathbf{e}_z dxdy\}}. \tag{2.25}$$

For the case of separate media, which is nowadays common in optical waveguides, with constant n_i' and n_i'', we can change the integration limits in (2.25), isolate bulk absorption coefficient α_i and write

$$\alpha_m = \sum_i \alpha_i c\epsilon_0 n' \frac{\iint_A |\tilde{\mathbf{E}}|^2 dxdy}{\mathrm{Re}\{\iint_A (\tilde{\mathbf{E}} \times \tilde{\mathbf{H}}^*) \cdot \mathbf{e}_z dxdy\}}. \tag{2.26}$$

We see that we have obtained essentially the same equation as (2.16). This means that anything besides the absorption coefficients in (2.26) is in fact the confinement factor. We can thus write

$$\Gamma_i = \frac{c\epsilon_0 n_i' \iint_i |\tilde{\mathbf{E}}^2| dxdy}{\mathrm{Re}\{\iint_{-\infty}^{\infty} (\tilde{\mathbf{E}} \times \tilde{\mathbf{H}}) \cdot \mathbf{e}_z dxdy\}}. \tag{2.27}$$

The absorption is therefore proportional to the square of the electric field, and (2.27) can be thought of as "*...the amount of intensity overlapping the gain medium per unit input power.*" (37). As such, Γ is not normalised to unity, which might appear rather odd. It can be calculated from a modelled field distribution, and it really does not add up to 100 % as shown further.

Equation (2.27) allows one to calculate the confinement factor directly from the electromagnetic field distribution and material constants. However, it does not make it clear why it does not amount to unity. Robinson *et al.* (37) have taken a different approach to derive (2.27), but more importantly, the authors also derived more intuitive formula for Γ. Starting from a variation theorem for dielectric waveguides (see Appendix A for more details)

$$\Delta\beta = \frac{2\omega \iint_{-\infty}^{\infty} \Delta\epsilon |\tilde{\mathbf{E}}|^2 dxdy}{\mathrm{Re}\{\iint_{-\infty}^{\infty} (\tilde{\mathbf{E}} \times \tilde{\mathbf{H}}^*) \cdot \mathbf{e}_z dxdy\}} \tag{2.28}$$

By using (2.16) and (2.19) we again arrive to expression (2.27) for the confinement factor. One can think of the energy stored per unit length

$$\frac{E}{l} = \frac{1}{2} \iint\limits_{-\infty}^{\infty} \epsilon |\tilde{\mathrm{E}}|^2 dxdy. \tag{2.29}$$

But in a propagating electromagnetic wave, or mode in this case, energy travels with the group velocity v_g. The same quantity can be also expressed with the energy flux, that is the Poynting vector, as

$$\mathrm{Re}\left\{ \iint\limits_{-\infty}^{\infty} (\tilde{\mathrm{E}} \times \tilde{\mathrm{H}}^*) \cdot \mathbf{e}_z dxdy \right\} = v_g \iiint\limits_{-\infty}^{\infty} \epsilon |\tilde{\mathrm{E}}|^2 dxdy. \tag{2.30}$$

Combining (2.30) with (2.27) then provides more intuitive formula

$$\Gamma_i = \frac{n_g}{n_i} \frac{\iint_i \epsilon |\tilde{\mathrm{E}}|^2 dxdy}{\iint_{-\infty}^{\infty} \epsilon |\tilde{\mathrm{E}}|^2 dxdy} \tag{2.31}$$

where the first fraction is related to dispersion, and the second is simply the energy density fraction. Γ can obviously run over 100 %. I emphasise that equations (2.27) and 2.31 are only applicable to waveguides with a continuous translational symmetry. One can expect that periodic structures like photonic crystals and their subclass of subwavelength gratings will be integrated over a volume of a unit cell rather than the cross section. This leads to an expression (38; 39)

$$\Gamma_i = \frac{n_g}{n_i} \frac{\iiint_i \epsilon |\tilde{\mathrm{E}}|^2 dxdydz}{\iiint_{-\infty}^{\infty} \epsilon |\tilde{\mathrm{E}}|^2 dxdydz}. \tag{2.32}$$

There are therefore two ways to enhance the confinement factor. One is through strong light localisation/delocalisation, the other is through engineering the dispersion.

2.1.4 Losses in Optical Waveguides

All optical components suffer from losses, which may significantly limit the optical system but not always. In bulk optical components like lenses or mirrors, the loss can arise from intrinsic material absorption or surface roughness. The same is true for optical waveguides but additional loss mechanisms exist, and some of them can become more prominent in MIR, which is of particular concern in this thesis. On the other hand, scattering loss is not considered here; It is proportional to λ^{-4}.

2.1.4.1 Material Absorption

Optical waveguides rely on relatively long propagation paths, spanning from millimetres in telecom and datacom (40), and up over several centimetres (41) to even metres in integrated

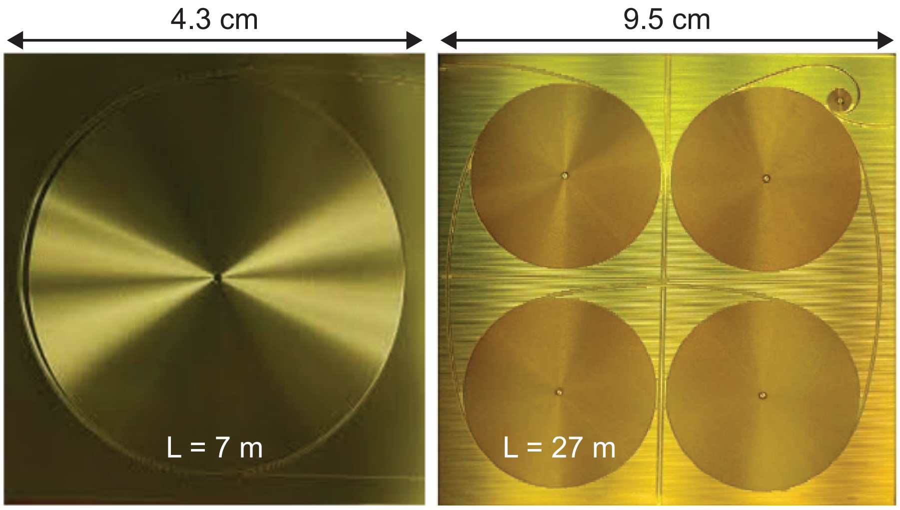

Figure 2.7: Optical micrographs of integrated optical delay lines. The waveguides were coiled into spirals to achieve pathlengths L in the order of metres.

delay lines (42; 43) as shown in Fig. 2.7. Optical transparency of some materials in MIR has been reviewed several times (44; 45; 46; 47) and Fig. 2.8 summarises information about many of these and it allows an easy selection of optical materials for waveguide engineering.

Si and SiO_2 are likely the most common materials in nanophotonics since they constitute the silicon-on-insulator (SOI) platform. Si is a semiconductor and hence its transparency is limited by the absorption due to excitation of electrons into the conductive band below 1.1 µm. Phonon absorption limits the transparency at longer wavelengths. This occurs around 7 µm in Si, albeit Soref (44) marks the transparency edge around 8.5 µm with a 2 dB cm^{-1} cut-off as opposed to 1 dB cm^{-1} used by Lin *et al.* (46). Germanium, another group IV semiconductor besides silicon, exhibits even broader transparency from 2 µm to 14 µm.

SiO_2, the main component of common glass, is transparent from 300 nm up to 3.5 µm. This is clearly not sufficient to cover the whole MIR wavelength range and other materials have been explored. Compounds with heavier elements, compared to SiO_2, have broader transparency (46). These are for example TiO_2, Al_2O_3, or Ta_2O_5, and all of them have been used for optical waveguides manufacturing. However, residual water, and OH groups absorb within parts of the MIR range as seen on the OH bond stretch bands in Fig. 2.8 and water absorption spectrum in Fig. 2.9.

OH groups are in particular found in amorphous oxides. They can be removed from silica by annealing: Yongheng and Zhenan studied the effect of annealing silica at temperatures from 800 to 1200 °C, and found that the content can be substantially reduced. It seems that to date, other oxides have not been studied in such detail as silica. The applicability of annealing to other amorphous oxides is thus a matter of further investigations while crystallisation needs to be avoided (e.g., Ta_2O_5 crystallises around 600 °C).

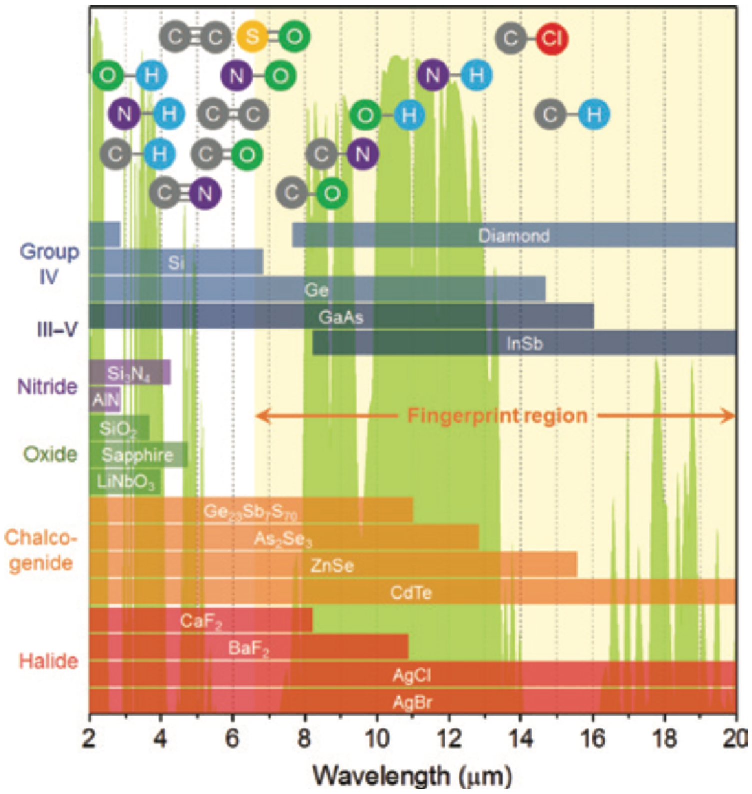

Figure 2.8: Material transparency. Bars represent optical transparency windows (1 dB cm^{-1}) of various materials, the top panel depicts the spectral locations of the primary absorption bands of different chemical bonds, and the background shows the infrared atmospheric transmission spectrum. Taken from (46).

2.1.4.2 Substrate Leakage

Substrate leakage occurs when the thickness of the bottom cladding is insufficient to isolate the guided mode from the substrate. The evanescent tail spans across the whole cladding and overlaps with the substrate. At the same time, one condition has to be fulfilled for the leakage to occur: The refractive index of the substrate n_s has to be larger than the effective index of the guided mode n_{eff}. This becomes more relevant at longer wavelengths because the light occupies a larger area and standard wafers might not be able to mitigate it.

Different strategies have been used to avoid this problem. An obvious one is making a thicker cladding, but this can become costly especially in SOI wafers because the price is proportional to the wafer oxidation time, which increases exponentially with the oxide thickness. Nevertheless, this loss has been minimised even in a standard SOI platform in MIR by structuring a slot waveguide with strong localisation (49). Other approaches rely on replacing the silicon substrate with sapphire, which serves as the cladding at the same time (50; 51; 52). Germanium on silicon (53) and germanium on SiGe (54) waveguides have the same capability. Another approach is to remove the bottom cladding completely, and structure free-standing waveguides,

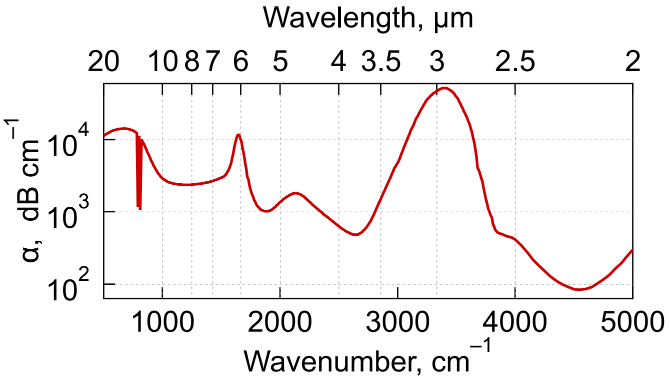

Figure 2.9: Absorption coefficient α of water. Data were taken from (48).

which has been done e.g., with Si, Ge, or diamond (55; 56; 57; 58; 59). Not only the substrate leakage is reduced or even removed, but the absorption in silica (discussed above) is solved too.

2.1.4.3 Lateral leakage in rib waveguides

This loss mechanism is very specific to the geometry and only occurs for TM-polarised modes. It is relevant in this work because of the air-suspended rib waveguide in Papers I and II. The rib waveguide is essentially surrounded by planar waveguides on both sides, which do support planar modes. Rib-guided TE modes are effectively confined, because their effective indices are always higher than any planar modes as illustrated in Fig. 2.10. This is not true for the rib-"guided" TM modes, which cross-couple into planar TE modes.

This may rise a question about how the cross-coupling can happen. The phenomenon is easy to understand considering that the modes of such waveguides are always hybridised as discussed in section 2.1.2, and thus the leakage occurs through the minor TE component of the TM-like mode. The effect is resonant, meaning that the light leaking into the planar modes has to interfere constructively, similarly to the self-consistency condition discussed for planar waveguides in section 2.1.1.1. Webster *et al.* (60) have experimentally verified the leakage in silicon rib waveguides as seen Fig. 2.10. The by targeting appropriate dimensions.

2.2 Absorption Spectroscopy

Spectroscopy is a study of the interaction between electromagnetic radiation and matter. The sample under study can be probed for example by EM radiation to induce fluorescence or record absorption spectrum, by electron beam to induce X-ray radiation, or it can be coupled to a flame to detect emission spectra. As outlined in the introduction, the focus of this thesis

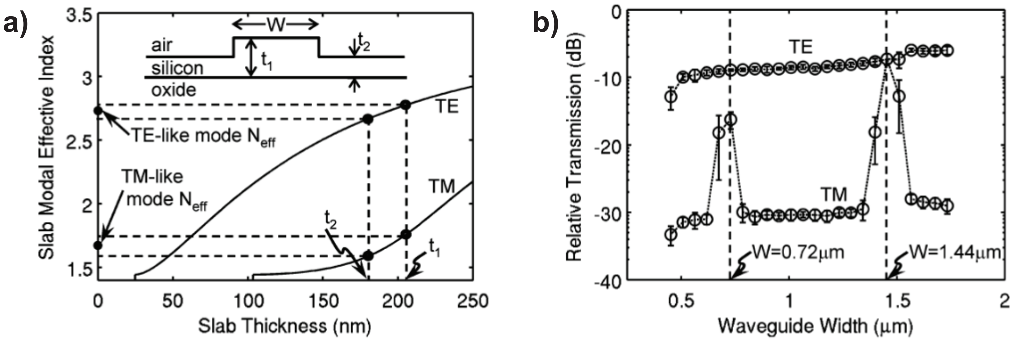

Figure 2.10: Theoretical analysis and experimental demonstration of lateral leakage in rib waveguides. **a)** Effective indices for varying thickness of the slab. Solid curves show effective indices for planar waveguide modes for **b)** Experimental demonstration of the effect. Taken from (60).

is on MIR absorption spectroscopy for molecular gas sensing because it allows high-resolution specific detection.

Light absorption, but also emission, occurs at resonant frequencies/energies, which are given by differences between energy levels of the considered system. There are three types of transitions: electronic, vibrational, and rotational in the order of decreasing energy, that is

$$\Delta E_{el} > \Delta E_{vib} > \Delta E_{rot}. \tag{2.33}$$

The transitions occur separately as well as in different combinations. Simultaneous changes in rotational and vibrational states are grouped under ro-vibrational transitions. Molecules in a gas phase feature unique ro-vibrational spectra, also called *molecular fingerprints*, which allow to distinguish many different molecular species. Specific detection is therefore achieved by targeting these transitions, which are located in the MIR domain.[2]

The next section provides more insight into molecular fingerprints and clarify why they are unique and how they help to achieve high limits of detection. Each transition has an associated spectral line with a particular profile or lineshape. Fundamentals behind lineshapes will be discussed, including the most common shapes and the dependence on ambient conditions. Many absorption spectra have been recorded directly or in terms of model parameters, and they are available through spectral databases PNNL and HITRAN, which are briefly introduced. After providing all necessary information regarding absorption spectroscopy, our experimental tuneable diode laser absorption spectroscopy setups is described together with the methodology of gas absorption measurement. The setups have been used to conduct the gas absorption experiments in papers I and II. The last section is dedicated to absorption saturation, which

---

[2] Ro-vibrational transitions occupy also the NIR part of the electromagnetic spectrum. However, the absorption in NIR is one to two orders of magnitude weaker than in MIR as will be discussed further.

requires caution in optical waveguides due to small field areas and thus relatively high light intensities.

2.2.1 Molecular Ro-Vibrational Spectra

The goal of this section is to give a brief explanation of how the rotational and vibrational states of molecules result in distinct spectral signatures in the infrared. First, heterogeneous diatomic molecules will be considered for their simplicity. They are also very illustrative. Then, the discussion will qualitatively extend to polyatomic molecules.

2.2.1.1 Diatomic Molecules

In order to illustrate the properties of the **vibrational transitions**, a simple model of a diatomic molecule is first considered. The simplest oscillating system is a linear harmonic oscillator (LHO), where the atoms of the molecule can be imagined connected by a spring. The potential energy of LHO is

$$U = \frac{1}{2} k_s (r - r_e)^2 \tag{2.34}$$

where k_s is the spring constant and r_e the equilibrium distance between the two atoms. The potential, which reflects attraction and repulsion between the atoms, is thus parabolic. This is of course an approximation which for example does not account for molecule dissociation.[3] From quantum mechanics, the energy of LHO is quantised:

$$E_{vib} = c_0 \tilde{\nu}_{vib} \left(v + \frac{1}{2} \right), \tag{2.35}$$

where c_0 is the vacuum velocity of light, $\tilde{\nu}$ is a fundamental frequency, and $v = 0, 1, 2, 3, \ldots$ is a quantum number associated with the vibrational states. The quantum number v is moreover restricted by a selection rule, $\Delta v = 1$ for LHO, and energy levels given by (2.35) are equally spaced.

Table 2.1: Absorption/emission bands of heterogeneous diatomic molecules.

Transition name	Transition
Fundamental band	$\Delta v = 1$
First overtone	$\Delta v = 2$
Second overtone	$\Delta v = 3$ and so on

More accurate models allow anharmonic oscillations and the selection rule changes to allow other then unitary transitions. For example the CO molecule is very close to LHO but in reality,

---

[3] More accurate model is provided by Morse potential but its shape is parabolic near the minimum. The use of a linear harmonic oscillator is thus justified for low energies.

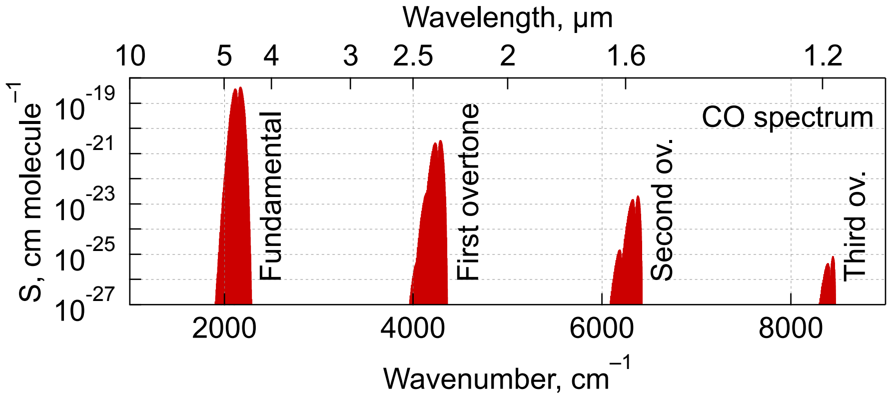

Figure 2.11: Vibrational spectral bands of CO modelled at atmospheric pressure, 20 °C and 100 %. The spectrum is modelled at atmospheric pressure, 20 °C and 100 % with data from HITRAN (16).

there are other than unitary transitions, which can be seen in its infrared spectrum in Fig. 2.11. The transitions appear as bands because of the simultaneous rotational transitions, which are discussed further in this section. Diatomic molecules thus features several simple bands distinguished by the change in v and they are listed in Table 2.1.

The higher order bands are by 1 to 2 orders of magnitude weaker than the fundamental ones (Fig. 2.11), which typically lie in the MIR domain. This is a strong argument for performing the absorption spectroscopy at MIR within the fundamental bands.

Rotational transitions have much lower energies, in the microwave domain, and they are responsible for the fine structure of the infrared spectra. Rotational states of a diatomic molecule can be modelled by a rigid rotor, where the atoms are just connected point masses with a fixed distance in between them. When spinning, the system has energy

$$E = \frac{1}{2} L\omega \tag{2.36}$$

where L is angular momentum. In the a quantum-mechanical rotating system, L is quantised and so is the energy, which then reads

$$E = BJ(J+1) \tag{2.37}$$

where $J = 0, 1, 2, 3...$ is a quantum number associated with total angular momentum and $B = h/8\pi^2 Ic$ is a rotational constant. The selection rule requires that $\Delta J = \pm 1$. J can only change by $+1$ due to absorption because the energy of the system has to increase. When ro-vibrational transitions are considered, J can change by both $+1$ and -1 as long as $\Delta v \leq 1$ because the energy increases in both cases.

Changes in E are even multiples of B; $2B$, $4B$, $6B$ according to (2.37) and hence the line spacing is uniform with a distance of $2B$. This uniformity breaks down for some molecules because of

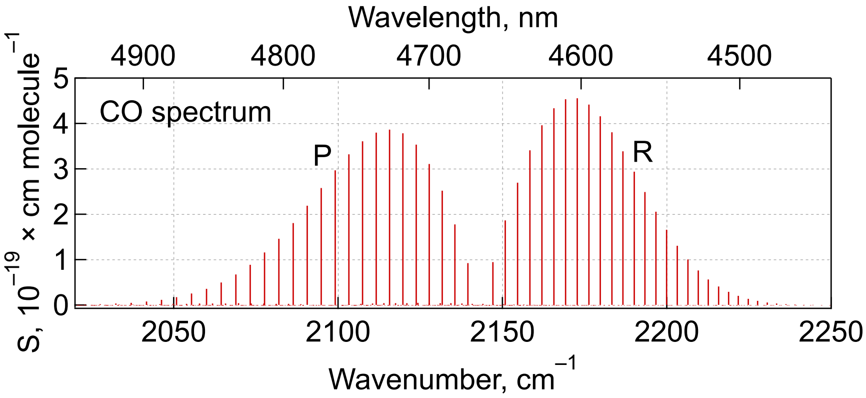

Figure 2.12: Rotational transition lines of CO in the fundamental vibrational mode. The spectrum shows the two branches P and R for ΔJ of −1 and +1 respectively. The spectrum is modelled at atmospheric pressure, 20 °C and 100 % with data from HITRAN (16).

centrifugal distortion, and more accurate models are again required. Nevertheless, CO behave almost ideally and the near-uniform spacing is apparent in the fundamental band in Fig. 2.12. The graph also shows two branches, P and R, which are associated with changes in J of −1 and +1 respectively.

The spectral lines of rotational transitions in Fig. 2.12 have a smooth envelope given almost entirely by Boltzmann distribution. Line intensity is a product of a transition probability and a population of the state N_J. All probabilities happen to be nearly constant (61) and the populations of states are given by Boltzmann distribution, hence the envelope of the spectral lines.

The positions of the spectral lines depend on the atomic masses and bond strengths but they are not fixed. Pressure and temperature can induce shift in the line position but the effect can be ignored at standard conditions (see section 2.2.3 for explanation) and it is not relevant for this work because all experiments were done at or near standard conditions.

To summarise the spectra of diatomic molecules, the **ro-vibrational transitions** are composed of vibrational transitions, with energies in the infrared, and rotational transitions, with energies in the microwave domain. The result is absorption bands across the infrared domain, with the strongest fundamental transitions lying particularly in the mid-infrared as indicated in Fig. 2.11. Different atomic masses and bond strengths result in unique positions and spacings of the spectral bands and lines. This is the origin of the molecular fingerprints.

2.2.1.2 Polyatomic Molecules

The molecular spectra become a lot more complex in polyatomic molecules. Such molecules a number of vibrational modes and for the total of N atoms, linear molecules have $3N-5$ modes while nonlinear ones have $3N-6$. These various modes can be excited simultaneously resulting in combination bands in addition to those found in diatomic molecules. The possible bands are listed in Table 2.2.

Table 2.2: Absorption/emission bands of polyatomic molecules.

Transition name	Label	Transition	
Fundamental bands	v_i	$\Delta v_i = 1$	
First overtone	$2v_i$	$\Delta v_i = 2$	
Second overtone	$3v_i$	$\Delta v_i = 3$	
Combination bands	$v_i + v_j$	$\Delta v_i = 1, \Delta v_j = 1$	
	$2v_i + v_j$	$\Delta v_i = 2, \Delta v_j = 1$	etc
Difference bands	$v_i - v_j$	$\Delta v_i = 1, \Delta v_j = -1$	

Rotational transitions can now be associated with up to all 3 orthogonal axes. There are therefore up to 3 different rotational constants B depending on the symmetries of the molecule (61).

Fig. 2.13 gives an example of the fundamental band of CH_4, showing few notable features which were not present in the CO spectrum (Fig. 2.12). There are the familiar P and R branches but in addition, there is a whole new Q branch associated with no change in the total angular momentum, that is $\Delta J = 0$. The inset also reveals that there are many overlapping finely spaced lines of the rotational transitions. The absorption spectra thus grow in complexity with the increasing number of atoms in the molecule.

2.2.2 Spectral Lineshapes

The discussion above revolved only around the origin of the infrared absorption spectra of molecules while showing examples of CO and CH_4. Graphs in Figs. 2.11–2.13 show the spectra in terms of spectral lines, which have particular intensities but they are represented only by discrete points. This section is concerned with the lineshapes associated with the spectral lines; Each spectral line is modulated by a frequency-dependent lineshape function $\phi(\tilde{v})$, which enters the Lambert–Beer law describing light attenuation

$$I = I_0 \exp\{S^*_{ij} n_i \phi(\tilde{v}) L\} = I_0 \exp\{S p_i \phi(\tilde{v}) L\} = I_0 \exp\{\alpha(\tilde{v}) L\}. \tag{2.38}$$

n_i denotes a molecular density in molecule cm^{-1}, S^* spectral line intensity in cm $\mathrm{molecule}^{-1}$, p_i partial pressure, S is a line strength in $\mathrm{cm}^{-1}\,\mathrm{atm}^{-1}$, $\alpha(\tilde{v})$ absorption coefficient in cm^{-1} and

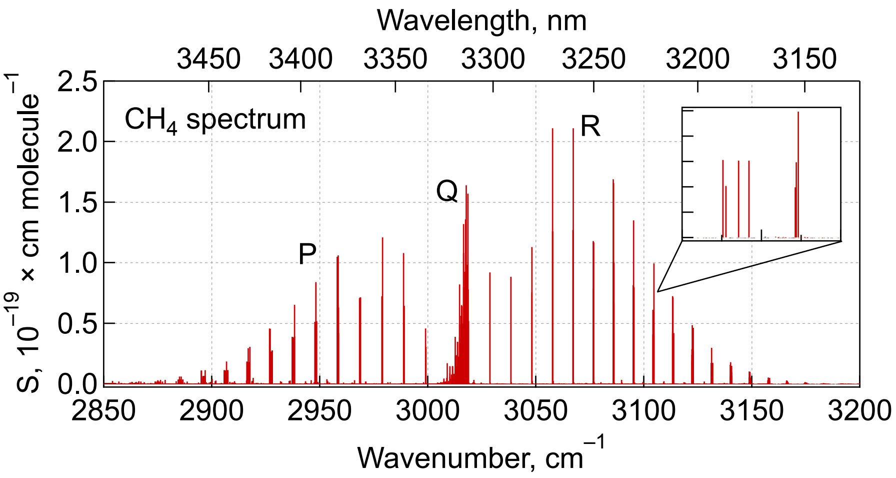

Figure 2.13: Spectral lines of the CH$_4$ fundamental vibrational band at atmospheric pressure, 20 °C, and 100 % concentration with data from HITRAN (16).

L is the light pathlength through the gas. The transition happens between a low energy state i and a high energy state j.

Besides line positions, the lineshape $\phi(\tilde{\nu})$ also depends on external conditions, namely pressure, partial pressure, and temperature. These conditions cause line broadening, which is either *homogeneous*, *inhomogeneous*, or a combination of both. The kind of broadening then determines the lineshape.

Homogeneous broadening is characteristic by a Lorentzian lineshape

$$\phi_C(\tilde{\nu}) = \frac{1}{\pi} \frac{\Delta\tilde{\nu}/2}{(\tilde{\nu}_{ij} - \tilde{\nu})^2 + (\Delta\tilde{\nu}/2)^2}, \tag{2.39}$$

and there are two mechanisms. Every quantum system, such as a molecule, exhibits *natural broadening*, which follows from the Heisenberg relations of uncertainty between lifetime τ_i of the energy level i and its energy $\Delta E_i = h\Delta\tilde{\nu}_N$. Since the transition involves two levels i and j, the broadening depends on both lifetimes as

$$\Delta\tilde{\nu}_N = \frac{1}{2\pi}\left(\frac{1}{\tau_i} + \frac{1}{\tau_j}\right). \tag{2.40}$$

The second mechanism involves energy transfer from one molecule to another during collisions (hence the subscript C in (2.39)) and the lifetimes are effectively shortened. Line profiles then broaden according to (2.40). The effect increases with pressure and this mechanism is called *pressure/collisional broadening* ($\Delta\tilde{\nu}_C$) and it is captured in collisional half-widths γ_{B--A},[4] for species A acting on B. The γ parameters are related to the lineshape FWHM as

$$\Delta\tilde{\nu} = p\sum_A X_A 2\gamma_{B-A}, \tag{2.41}$$

---

[4] More precisely, the parameter are specified as half-width and half maximum (HWHM) (16).

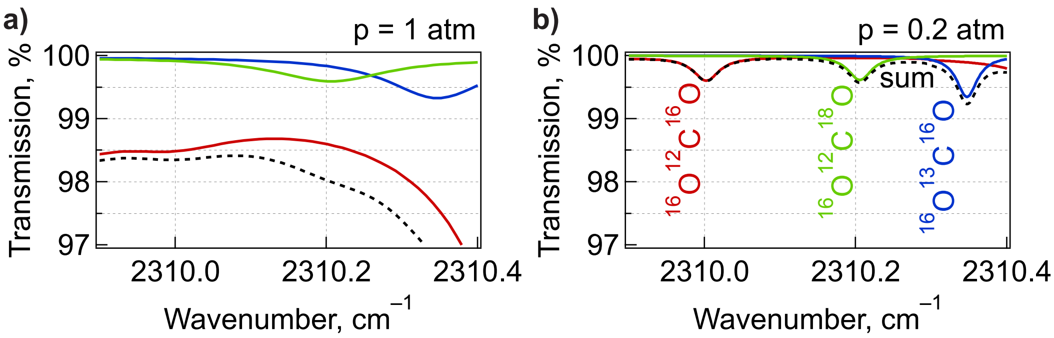

Figure 2.14: Transmission spectra of the three most abundant isotopes of CO_2 at pressures of 1 atm and 0.2 atm over a 1 cm path. The spectra were modelled at 20 °C, 1 % total CO_2 concentration with isotope abundances of 98.4 % ($^{16}O^{12}C^{16}O$), 1.1 % ($^{16}O^{13}C^{16}O$), and 0.4 % ($^{16}O^{12}C^{18}O$). The data were taken from HITRAN (16).

where X_A is a molar fraction of species A. Collisional broadening has a noteworthy property of keeping the line amplitude constant with respect to pressure variations, which aids differentiation of finely spaced spectral lines such as those of CO_2 isotopes in Fig. 2.14.

The lineshape resulting from inhomogeneous broadening is Gaussian,

$$\phi_D(\tilde{\nu}) = \frac{1}{\sqrt{2\pi}\Delta\tilde{\nu}_D} \exp\left\{-\frac{(\tilde{\nu}-\tilde{\nu}_{ij})^2}{\Delta\tilde{\nu}_D^2}\right\} \tag{2.42}$$

and it is represented by *Doppler broadening*. The profile results directly from a Gaussian distribution of velocities, where molecules moving along the light propagation direction experience a red shift in the line position and vice versa. This type of broadening is directly proportional to frequency, that is $\Delta\tilde{\nu}_i \propto \tilde{\nu}$.

Lorentzian profiles are dominant in high pressure environments due to collisional broadening. This situation is typical for lower atmosphere. Gaussian profiles conversely prevail in low pressure environments, such as higher atmosphere, where collisions are scarce and the effect of Doppler broadening is stronger.

Although one type of broadening is often dominant, true lineshapes are combinations of both. The most common lineshape is the Voigt function, which is a convolution of Doppler and collisional broadening,

$$\phi_V(\tilde{\nu}) = \int_{-\infty}^{\infty} \phi_D(u)\phi_C(\tilde{\nu}-u)du. \tag{2.43}$$

It is valid under the assumption that natural broadening is much weaker than the collisional (61), and this lineshape function is often highly accurate. However, it has been reported in recent years that it cannot reproduce atmospheric spectra accurately in some exceptional situations, particularly at sub-percent level and for light molecules (16). More accurate models are required but such discussion is beyond the scope of this thesis.

2.2.3 Spectral Databases

Practical applications of molecular spectroscopy are nowadays enabled by databases, which provide spectral lines parameters or actual spectra for a number of molecules. This data allow to identify molecular species in measured spectra in a range of applications or to model atmospheric transmission. There are several spectral databases but only two pertain to this work, namely the High Resolution Transmission compilation (HITRAN) (16) and the Northwest Infrared database (NWIR) (62) from the Pacific Northwest National Laboratory (PNNL) and usually referred to as the PNNL databases (this name is also assumed throughout this thesis). HITRAN stores parameters for transmission spectra modelling while PNNL provides experimental spectra.

HITRAN has been launched in 1960s with only 7 molecules and 4 parameters (63) including line positions $\tilde{\nu}_{ij}$, line intensities S^*_{ij}, lower-state energies, and collisional broadening half-widths γ as they appear in 2.41. The database has been continuously updated and currently compiles parameters for 55 different molecules and differentiates many of their isotopes. In addition to the original parameters, HITRAN now accounts for temperature-dependent collisional broadening, pressure-induced line shifts, and started to include temperature dependence of the pressure-induced line shifts. The authors also started to include parameters of other than Voigt profiles.

The data in HITRAN are provided at standard conditions. The effects of different ambient conditions are accounted for through a set of parameters

The PNNL database, on the other hand, is a set of experimental spectra recorded with $0.112\,\mathrm{cm}^{-1}$ resolution and $0.06\,\mathrm{cm}^{-1}$ sampling (64). The data have been prepared for several different concentrations at temperatures of 5 °C, 25 °C, and 50 °C, and standard pressure. As such, the data can scale with varying environmental conditions. Like HITRAN, the PNNL database had been continuously updated by adding more molecular species (65). Unfortunately, the data is no longer freely available at the time of writing this thesis.

2.2.4 Tuneable Diode Laser Absorption Spectroscopy (TDLAS)

In this section, the focus is on the methodology of TDLAS, which implementations have been reviewed by Hodgkinson (20) along with other spectroscopic techniques for gas detection. TDLAS is principally simple and the following paragraphs discuss how it operates and what challenges lie in the implementation.

The instruments rely on passing a laser beam through a gas cell filled with the analyte as depicted in Fig. 2.15 but setups for measuring over an open space path also exist (66). The

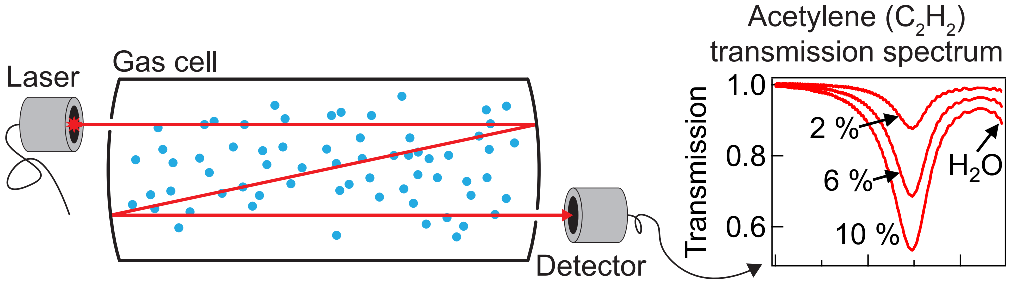

Figure 2.15: Schematics of a standard TDLAS setup with a multi-pass gas cell. The laser wavelength is tuned over the analyte absorption peak, which is then observed in the output spectrum such as the one of acetylene around 2566 nm shown here. The spectrum also indicates presence of water.

laser is tuned over a spectral range where absorption lines of the analyte are located. The light intensity received by the detector is attenuated accordingly with Lambert–Beer law (2.38) unless the absorption is saturated, which is discussed in a separately in section due to the relevance in integrated sensors. The recorded transmission is analysed to get qualitative and quantitative information about the sample and several analytes can be identified at once (67).

The laser wavelength can be tuned either by controlled temperature modulation or driving current modulation. Temperature control provides lower modulation of the output power but it is relatively slow. Current modulation is faster but it significantly affects the output power and the output signal is characteristic by residual amplitude modulation (RAM) if no normalisation was done. The selection will therefore depend on the power and speed requirements.

Equation (2.38) shows that it is possible to increase the magnitude of the detected signal by increasing the pathlength. Long paths are achieved by folding the beam between two mirrors several times to to obtain lengths of several tens of meters (20), which facilitates high sensitivity. The spectrum can be obscured by etalon fringes originating from the coupling windows, non-specular scattering from optics, and edge diffraction (68). The impact can be lowered by adding anti-reflection coatings on the windows and using wedged windows. Moreover, techniques of active suppression have been developed.

Gas cells introduce another limitation due to their relatively high volume, often in the order of litres. Large samples are therefore required and the volume needs to be entirely exchanged during consecutive sampling to ensure reliable measurement. The response time is thus limited by this factor and has already lead to development of low-volume gas cells such as a toroidal cavity with reflective surfaces (69; 70). The lowest volumes are achieved with hollow core fibres and they also feature the best pathlength to volume ratio (20). This is an important figure of merit of gas cell because the laser beam fills only a small fraction of the gas cell

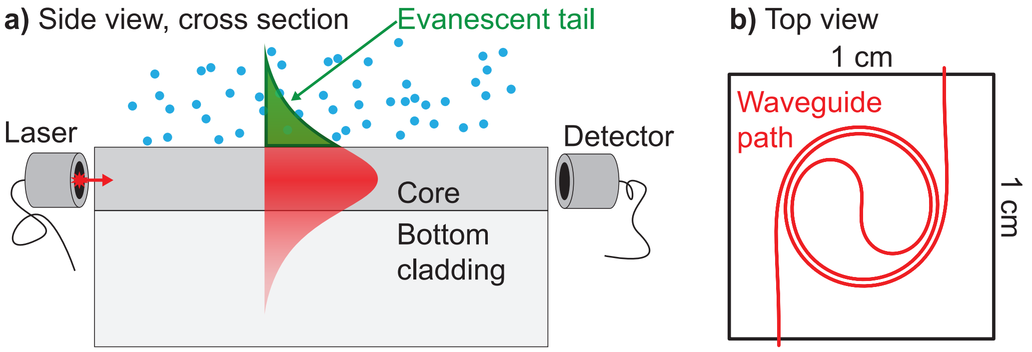

Figure 2.16: Schematics of a TDLAS setup with a waveguide instead of the multi-pass cell. **a)** Interaction between the guided mode and the analyte happens through the evanescent field. **b)** Waveguides can be coiled into a spiral to achieve small footprints.

volume and the sample is not used efficiently. Nevertheless but they are even more limited in the response times with some configuration requiring minutes to fill up the fibre [refs].

The large volumes and long filling times hinder the field utility in many applications. Some current solutions are portable and allow in situ measurements but the most sensitive instruments are often bound to laboratories and require discrete sampling. This hinders time resolution of continuous monitoring and sampling is also a major source of errors.

2.2.4.1 Miniaturisation

TDLAS has a potential to be miniaturised by making use of integrated optics. In this scenario, the open optical path and bulk optics can be replaced with an optical waveguide as shown in Fig. 2.16a and the waveguide can be wrapped as a spiral to utilise the limited chip space efficiently as seen in Fig. 2.16b. Hence a long path can be achieved on a small footprint.

Most waveguides will give lower effective pathlength ΓL compared to the physical pathlength: $\Gamma L < L$ where Γ is the confinement factor from section 2.1.3.[5] This adjustment enters the Lambert–Beer law (2.38). There are few exception such as the air-suspended rib waveguide presented in Papers I and III and PhC waveguides making use of the slow light (38), which feature Γ values of or over $100\,\%$. It is currently challenging to increase the integrated sensor sensitivity given the typical propagation losses of MIR waveguides in units of $\mathrm{dB\,cm^{-1}}$. Decreasing the loss requires input from materials science and, as discussed in section 2.1.4.1, and Papers I and III. Although a challenge, it opens a potential for further research.

It was discussed in the introduction that TDLAS miniaturisation holds a promise towards a fully integrated system, that is laser, waveguide, and detector on a single chip and such

---

[5] As a reminder, Γ is directly proportional to the electric field energy density $\epsilon|\mathbf{E}|^2$ and the group index n_g.

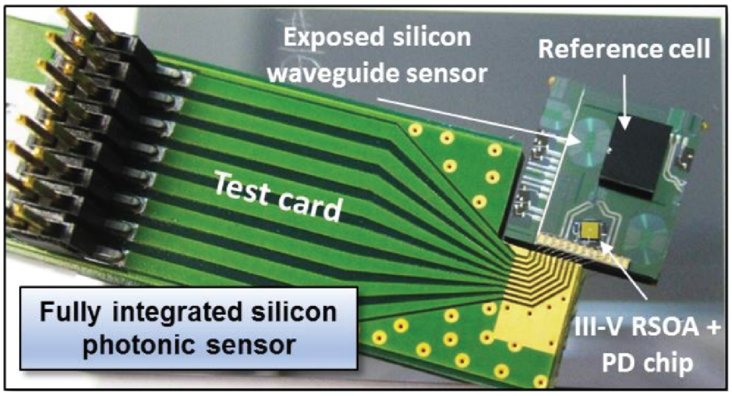

Figure 2.17: Fully integrated photonic chip sensor mounted on a PCB test card for testing. Taken from (21).

systems are under development. It is possible to add other functionalities too, for example from the various MEMS components developed to date.

An integrated TDLAS sensor will not be able to compete with its bulk counterparts in terms of sensitivity but it is sufficient to design the system to perform well enough in selected applications (20). Fabry–Pérot etalons are another disadvantage and they are much stronger then in multi-pass cells. E.g., SOI waveguides have effective indices above 1.43, giving 3 % Fresnel reflection and a 10 % transmission modulation. The fringes also drift with temperature variation, resulting in an increased measurement uncertainty. To tackle this, methods of waveguide etalon suppression are being investigated (71; 72). Compared to the bulk instruments, miniaturised TDLAS will have low size and weight, and relaxed power consumption. However, waveguides have advantage over the bulky instruments in several aspects. With full integration, such system will be robust and resistant against misalignment; The laser only needs to couple into the waveguide and not into a carefully aligned multi-pass cell. The low size of the sensor also means less than 1 ml sample volumes. This further means reduced sample handling with and online monitoring *in situ* measurement capability.

In the last few years IBM demonstrated an a significant progress towards an integrated TDLAS setup for methane detection, targeting lines around 1650 nm (41). Their efforts resulted in a monolithically integrated photonic sensor incorporating an on-chip III-V laser, detector, sealed reference cell, and sensing waveguide with $\Gamma = 15\,\%$ and sub-100 ppm/$\sqrt{\text{Hz}}$ sensitivities (21) shown in Fig. 2.17. Integration of MIR lasers with waveguides is also being investigated, as discussed in the introduction, and it will facilitate even higher sensitivities.

Before leaving this section, it is worthwhile to summarise the characteristics of miniaturised TDLAS sensors:

- **Accuracy.** Maximum deviation of the measured quantity from the true quantity.

- **Precision.** Ability to reproduce the response to the same input.
- **Sensitivity / Limit of Detection.** The least detectable change of the measured quantity.
- **Specificity.** Ability to identify the analyte.
- **Response time.** Response of the sensor to a step-wise change of the measured quantity. The required time to reach a certain level of the measured response such as 90 %.

Most of these pertain to TDLAS in general. High accuracy is inherent to TDLAS because it is an absolute method, but it can be limited e.g., by the absorption model (see the next section). Precision will be prone to etalon fringes interference and etalon suppression is therefore imperative. Sensitivity and specificity were already discussed; Long paths, strong light–matter interaction, and detection in the fingerprint region govern these merits. Last, the response time is specific to the miniature sensors. Fast response will be achieved with a small gas cell, such as the one in the IBM sensor described above.

2.2.5 Saturation of Absorption

Lambert–Beer law (2.38) was defined for a linear absorption but it is possible to enter a saturation regime. When the absorption rate starts approaching the lower state repopulation rate, the lineshape will be affected. This will occur when the incident intensity is relatively high, which can be achieved with lasers, and it is highly pertinent to waveguide modes. The modal area of a free-space beam is typically 1 mm^2 to 10 mm^2 while optical waveguides confine the same power to areas of 0.1 to 10 $\mu\mathrm{m}^2$, 3 orders of magnitude smaller. When designing a waveguide-based sensor, the absorption saturation should be therefore analysed because it affects the lineshapes and the measurement accuracy. Two cases can be distinguished based on the relative linewidths of the laser $\Delta\nu_L$ and the absorption peak $\Delta\nu_a$: Either $\Delta\nu_L$ is larger than $\Delta\nu_a$ or vice versa. In our setup, $\Delta\nu_L$ is typically much narrower than $\Delta\nu_a$, and only this case will be considered in the following discussion.

Homogeneously broadened lines will become wider and inhomogeneously broadened ones will show a dip in the lineshape.

The change in light intensity dI due to absorption is simply given as

$$dI = -I\alpha dz. \tag{2.44}$$

This expression describes linear absorption, assuming that α is constant, and integration gives directly the Lambert–Beer law. In nonlinear absorption, however, the absorption coefficient is a function of the incident intensity $\alpha = \alpha(I)$. First approximation, $\alpha(I) = \alpha_0(1 - bI)$,

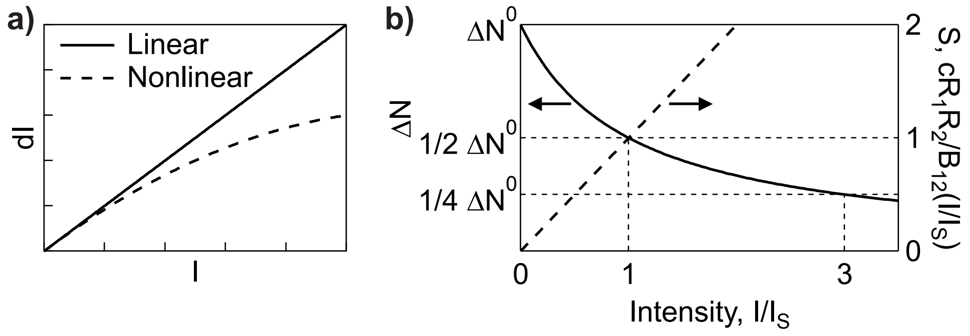

Figure 2.18: Nonlinear absorption illustration. **a)** Comparison of linear and nonlinear absorption given by equations (2.44) and (2.45). **b)** Population difference ΔN and saturation parameter S as a function of incident intensity I relative to the saturation intensity I_S.

yields

$$dI = -(I\alpha_0 - \alpha_0 b I^2)dz \tag{2.45}$$

where the second term represents the nonlinear contribution to the absorption and effectively lowers it. As noted above, and plotted in Fig. 2.18a, the nonlinearity will be observable only at high intensities relative to the lower state relaxation rate. Demtröder (73) further shows how this effect can be predicted.

In a two-level system, and assuming that the light frequency is tuned to the centre of the absorption line ν_0, (2.44) can be written as

$$dI \approx \Delta N dz I_\nu(\nu_0)\sigma_{12}(\nu_0) \tag{2.46}$$

where $\Delta N = N_2 - N_1$ is the difference between upper and lower energy state populations, I_ν is the spectral intensity [W s m^{-2}], and σ_{12} is the absorption cross section. ΔN follows from rate equations (73),

$$\Delta N = \frac{\Delta N^0}{1 + B_{12}I_\nu/c(1/R_1 + 1/R_2)} = \frac{\Delta N^0}{1+S}. \tag{2.47}$$

ΔN^0 is the number of available states for $I_\nu = 0$, B_{12} is the Einstein coefficient of absorption, R_1 and R_2 are the relaxation rates of levels 1 and 2 respectively. S is called the saturation parameter and it was chosen as

$$S = \frac{B_{12}I_\nu(R_1 + R_2)}{cR_1R_2}. \tag{2.48}$$

The spectral intensity $I_S(\nu)$ at which $\Delta N = 1/2$ is called the saturation intensity (see Fig. 2.18b) and it follows from (2.48). Moreover, the total saturation intensity for narrow line laser is $I_S = I_S(\nu_0)\delta\nu_L$.

Assuming that collisional broadening is dominant, the saturation intensity can be calculated as (74; 75)

$$I_S = \frac{\epsilon_0 c^3 h^2 \gamma^2}{8\pi^2\mu_{12}^2} = \frac{\gamma^2}{\mu_{12}^2} 1.33 \times 10^{-50} \mathrm{J\,C^2\,cm^2\,s^{-1}} \tag{2.49}$$

where h is the Planck's constant and γ is the line HWHM in units of cm^{-1}. μ_{12} represents the transition dipole moment, here in units of C m, and it is related to the Einstein coefficient of spontaneous emission A_{21} through (76)

$$\mu_{12}^2 = \frac{A_{21} 3 \epsilon_0 h}{16 \pi^3 \nu_{12}^3} = \frac{A_{21}}{\tilde{\nu}_{12}^3} 3.55 \times 10^{-53} \mathrm{C}^2\,\mathrm{s\,cm}^{-1}. \tag{2.50}$$

where the line position $\tilde{\nu}_{ij}$ is in cm^{-1} and the A_{21} coefficient in s^{-1}. This relation between μ_{12} and A_{21} has practical importance because HITRAN provides Einstein coefficients A_{ji} and hence the saturation intensity I_S can be calculated using (2.49) and (2.50).

Equations (2.49) and (2.50) were used in Paper I to assess whether the absorption would get saturated when performing spectroscopy with a the air-suspended waveguide (see the next section for details). We concluded that the intensity in the waveguide is more than an order of magnitude below I_S and the saturation should not be observable. Indeed, the spectroscopy experiment presented in Paper I supports the linearity of absorption by comparing waveguide-based and free space spectra. However, the calculation of the transition dipole moment via (2.50) remains somewhat unclear at the time of writing this thesis.

Castrillo *et al.* (74) have done a theoretical analysis of CO_2 P(28)[6] transition line at $2312.4176\,\mathrm{cm}^{-1}$. I_S can be readily calculated with the data provided in the paper,[7] and it was verified that it is approximately $80\,\mathrm{W\,m}^{-2}$ as the authors have claimed. They have further claimed μ to be $1.7 \times 10^{-31}\,\mathrm{C\,m}$, but this number could not be reproduced with (2.50), which gives $7.68 \times 10^{-31}\,\mathrm{C\,m}$ for $A = 205.5\,\mathrm{s}^{-1}$ (16). Possible reasons are an error in Castrillo's calculation, and the effect of degeneracy which should be included in (2.50). According to Demtröder (77), the transition dipole moment is

$$\mu_{12}^2 = g_2 \frac{A_{21} 3 \epsilon_0 h}{16 \pi^3 \nu_{12}^3} \tag{2.51}$$

where g_2 is the upper state degeneracy. However, even with this formula and $g_2 = 55$ (16), Castrillo's transition dipole moment could not be reproduced.

To conclude the theoretical part of the absorption saturation, it needs to be said that more attention is required to this problematic. If done right, it allows to assess the saturation before experimenting with waveguides. The saturation will cause line broadening but only partly because the intensity in the waveguide can decrease below I_S during the light propagation. This can result in inaccurate measurement. However, it is best to test this phenomenon experimentally if possible.

---

[6] P stands for the P branch while the number in parenthesis is the rotational quantum number J. The label is therefore P(J) in general.

[7] The experiment has been designed with pure CO_2 at 1.3×10^{-4} atm pressure. Air-induced collisional broadening thus does not contribute to the linewidth and with $\gamma_{self} = 0.093\,\mathrm{cm}^{-1}\,\mathrm{atm}^{-1}$ (16) and natural broadening contribution of $1.3 \times 10^{-6}\,\mathrm{cm}^{-1}$ (74), the line HWHM is $1.3 \times 10^{5}\,\mathrm{cm}^{-1}$.

The next section shows application examples of the absorption saturation.

2.2.5.1 Application to Selected Waveguides

The saturation should be predictable from the relations above. The last thing that needs to be determined in waveguide-based spectroscopy is the intensity in the interacting field. That is, only the part of the field in air will participate in the light-matter interaction, which was discussed in section 2.1.3. It is not certain how the confinement factor (2.27) enters the intensity calculation, and more work in this direction is required. Nevertheless, it is not crucial for qualitative analysis of the waveguides and the calculation here is based on the power fraction. The difference between the two can be notable, as will be shown, but still far below an order of magnitude. The intensity in the waveguides needs to be at least an order of magnitude less than I_S (see Fig. 2.18b), and the use of the power fraction is justified.

Two waveguide types, an air-suspended Ta_2O_5 rib waveguide (Fig. 2.19a) and an SOI slot waveguide (Fig. 2.19b), which were studied in chapter **??**, are analysed for absorption saturation. The waveguides are intended for detection of acetylene at 2566 nm and methane around 3250 nm respectively. They are designed for opposite polarisations, TM in the rib and TE in the slot waveguide. Waveguide modelling was done with finite differences solver (MODE, Lumerical) and the power was calculated from the Poynting vector and normalised. The modal area was then calculated as the area where the power is more than $1/e$ of its maximum, and areas in both waveguides are displayed in Fig. 2.19 for comparison. Power fraction Γ_P was calculated as the total power in air over the total power in the mode. In both calculations, any field inside of the core material was excluded.

The calculated parameters for both waveguides are listed in Table 2.3, including the design wavelength, external confinement factor (that is, in air), and maximum laser power $P_{L,max}$. Lasers are those available in our MIR experimental setup described in section [ref]. As already mentioned above, typical waveguide mode areas are less than 10 µm^2, and in the two examples have areas of 3.36 µm^2 and as little as 0.05 µm^2 respectively.

Intensities in the waveguides are presented in two ways. First, the standard calculation is done by dividing the total power in air by the field area as

$$I_W = \frac{\Gamma_P P_L}{A} \tag{2.52}$$

where Γ_P is the fraction of the power in air,[8] P_L is the laser power, and A is the mode area in air based on the power distribution. The power fraction is included because the power within the core or cladding (other than air) does not contribute. The laser power should be also

---

[8] Generally the medium of interest, which could also be certain cladding.

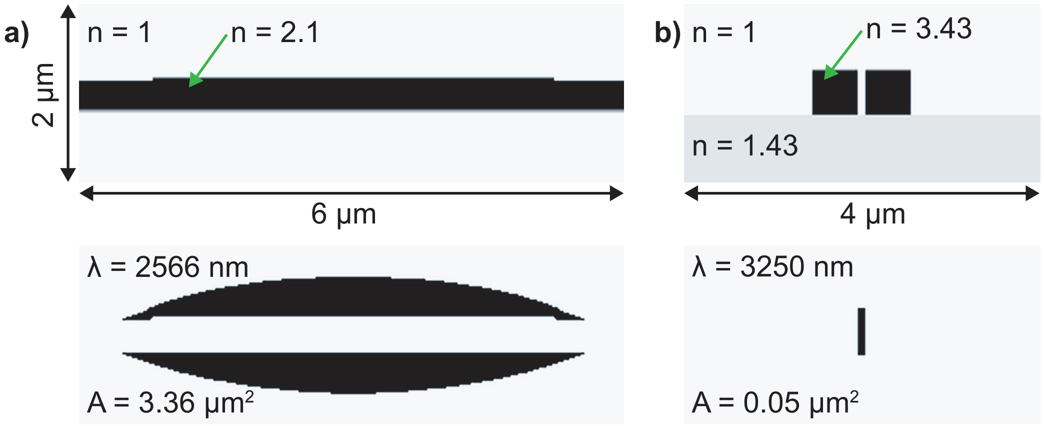

Figure 2.19: Areas of intensity larger than $1/e$ in two different waveguides studied in this work (see section). **a)** Air-suspended rib waveguide with 350 nm thickness at the centre, 30 nm etch depth and 4.5 µm width. The refractive index of 2.1 corresponds to Ta_2O_5. Wavelength of 2566 nm lies in acetylene and HF absorption bands. **b)** silicon slot waveguide with 100 nm wide slot, 550 nm wide and 500 nm high silicon slabs. Wavelength of 3250 nm is chosen for methane absorption.

adjusted for the waveguide coupling loss but it was omitted here and the resulting waveguide power is an upper limit.

Table 2.3: Waveguide parameters and molecular transition parameters for the selected analyte. W index refers to a waveguide and L to a laser. P_W represents the total power in the waveguide mode, I_W was calculated with (2.52), . Molecular transitions were selected according to the available DFB lasers and so as to avoid water absorption interference. p_{self} represents the selected gas partial pressure, γ_{self} and γ_{air} are collisional broadening parameters (HWHM) and γ is the line HWHM as defined in 2.41.

Parameter	Rib – C_2H_2	Slot – CH_4
λ [nm]	2566	3250
Γ [%]	108	79
Γ_P [%]	87	36
A [µm^2]	3.36	0.05
$I_{W,max}/P_W$ [m^{-2}]	1.8×10^{11}	5.5×10^{12}
$P_{L,max}$ [mW]	13.5	4
I_W [W m^{-2}]	4×10^9	8×10^{10}
$I_{W,max}$ [W m^{-2}]	2.4×10^9	2.2×10^{10}
Gas	Acetylene (C_2H_2)	Methane (CH_4)
A_{ji} [s^{-1}]	0.3518	27.65
$\tilde{\nu}_{ij}$ [cm^{-1}]	3897.148	3076.5496
μ_{ij} [C m]	1.45×10^{-32}	1.84×10^{-31}
γ_{air} [cm^{-1} atm^{-1}]	0.082	0.061
γ_{self} [cm^{-1} atm^{-1}]	0.158	0.0077
p_{self} [atm]	0.1	2×10^{-6}
γ [cm^{-1}]	0.0896	0.061
I_S [W m^{-1}]	5×10^{11}	1.5×10^9

3

Methods of Waveguide Design and Pattern

Each application of waveguides has its own specifics, which needs to be reflected in the waveguide design. For example, delay lines might require strong confinement to the core in order to reduce scattering from surface roughness (43; 42). SOI waveguides in MIR are limited by silica absorption loss, which has been circumvented by a strong confinement to either a large core waveguide (78) (Fig. 3.1) or a slot waveguide (49) operating at 3.8 µm respectively. Biosensing with surface functionalisation relies on strong light–matter interaction close to the waveguide surface (79; 80), and absorption spectroscopy is characteristic by sensing in a volume (81; 82; 80; 41) (Fig. 3.1b).

Modelling is done with numerical methods. In this work, two different softwares were used for the modelling making use of a finite difference method (FDM). In this section, the method is first introduced together with the softwares. Following the methodology part, results of waveguide modelling are presented.

3.1 Finite Difference Method (FDM)

FDM is a direct method, meaning that it solves given equations directly without making any assumption on the presented problem. In order to do that computationally, derivatives are

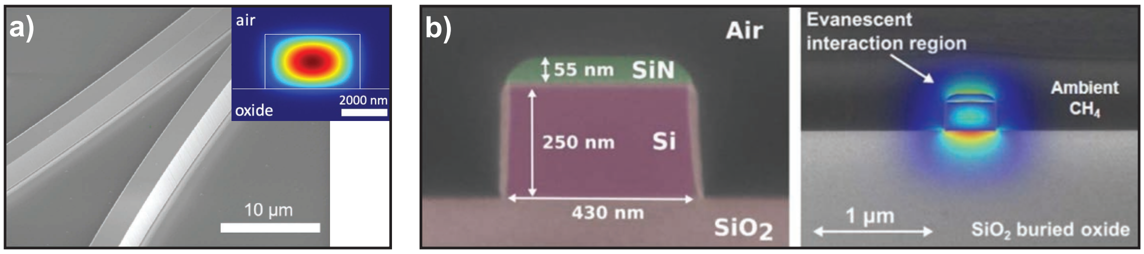

Figure 3.1: Illustration of the requirements on the field distribution in waveguides for specific applications. **a)** A large-core SOI waveguide for nonlinear applications past the silica absorption edge at 3.6 μm. The waveguide has been designed to have a small overlap with the silica cladding. Taken from (84) **b)** An SOI waveguide for methane sensing around 1650 nm. Taken from (41).

first replaced with finite differences (83)

$$f'(x) = \frac{f(x+h) - f(x-h)}{2h} + O(h^2). \tag{3.1}$$

where f is a function and f' its derivative. This can be applied for example to the wave equations (2.10) and (2.11), or directly to the Maxwell equations if the time dependence is factorised out. The computational domain is split into a mesh, and the equations are solved at each node.

Finite differences in time domain method is, as the name says, an application on time-dependent problems. As such, it can be used to directly solve Maxwell equations as they appear in (2.6)–(2.9)

Lastly, the methods need to be constrained by boundary conditions. In other, it needs to be imposed how the field behaves on the edge of a computational domain. Common boundary conditions include perfect electric conductor (PEC), perfect magnetic conductor (PMC) and perfectly matched layers (PML). PEC imposes that $E_{\parallel} = 0$ and $\partial E_{\perp}/\partial n = 0$ with n being the normal coordinate and vice versa for the magnetic field components. It simply nulls some field components and or their derivatives on a boundary. The situation is the opposite for PMC. PML are absorption type boundary conditions, and usually extend the computational domain by an additional layer(s) with gradually increasing absorption coefficient.

3.1.1 Solvers

Two modesolvers were used throughout the work on this thesis. These were FIMMWAVE from PhotonDesign, and MODE from Lumerical. Both implement FDM and, expectedly, have different additional features.

Scripting. FIMMWAVE can be interfaced with Python, which then allows extensive data post-processing. MODE comes with an internal scripting language, which is relatively easy to grasp. All user interface options can be accessed with the language, and post-processing is also possible although not into such extent as in Python.

Confinement factor. The confinement factor is directly implemented in FIMMWAVE, and it is sufficient to mark the areas where the calculation should be done. In MODE, the calculation needs to be implemented manually. A custom script was therefore written for this purpose, and it is available in Appendix B.

3.2 Waveguide Patterns – Mask Design

Designing a mask is an inherent part of waveguide design. Optimal waveguide dimension are defined in the mask and lithographic methods allow to transfer the pattern into a device layer. Masks in this work were created with commercial tool CleWin and an open-source tool Nazca. This section describes some particular features of the mask designs: Adiabatic connections based on clothoid curves, and automatic placement of etching openings along arbitrary waveguide paths.

3.2.1 Transition Loss and Adiabatic Curves

Section introduced propagation losses in optical waveguides, noting that there are several mechanisms. Waveguides enable long optical paths on small footprints, which is achieved by a compact waveguide pattern. As such, a single waveguide can consist of straight lines and bends of varying radii of curvature. Even if the waveguide cross section is the same along the whole path, bent and straight waveguides are not the same because the field distribution is different as seen in Fig. 3.2.

The limited overlap between modes in waveguides with different curvatures results in a loss proportional to the non-overlapping portions of the field distributions. Spirals are commonly used for tight patterning, but the direction of propagation needs to be reversed in the centre so that the waveguide exits the spiral pattern. This is done with an S-bend, which is particularly prone to the transition loss.[1] The effect can be mitigated by designing adiabatic transitions, that is paths where the curvature does not change abruptly but continuously over a certain distance.

---

[1] This kind of loss is perhaps not known in literature under any common name but it does occur, but the term "transition loss" has been used before (85)

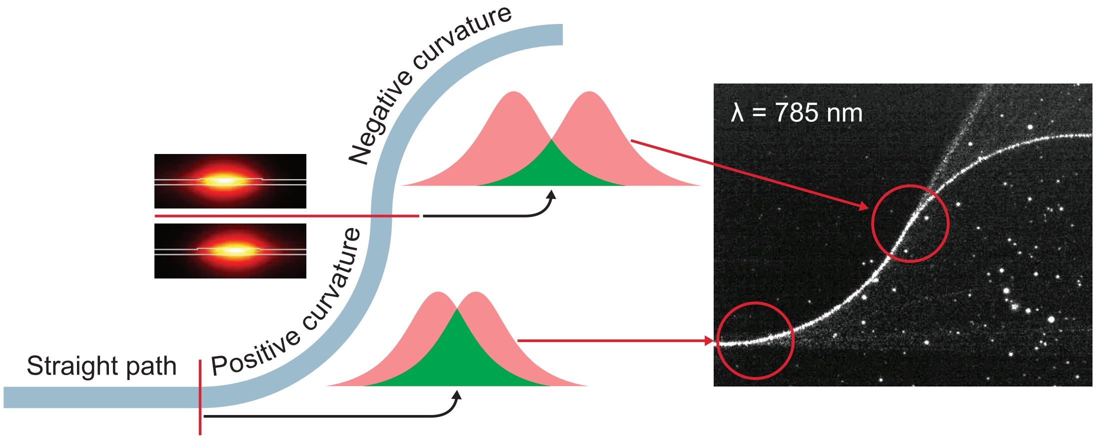

Figure 3.2: Transition loss illustration. Assuming an invariant cross section, field distributions are mutually offset in waveguides with different curvature, as seen in the simulated rib waveguide modes ($\mathbf{P}_z$) to the left of the path illustration. Only the overlapping portion of the field (in green) is coupled into the next mode. The microscope image on the right shows a real observation at 785 nm.

3.2.2 Minimum Variation Curves for Waveguide Connections

The minimum variation curve (MVC) problem has been elaborated in a Ph.D. thesis of Raphael Levien (86), who has applied it on font designs. Researchers from the Vahala group have introduced the MVC into their waveguide design for integrated optical delay lines (43; 85; 42). It is defined by an integral

$$E_{MVC} = \int_0^l \left(\frac{d\kappa}{ds}\right)^2 ds \tag{3.2}$$

where κ is the curve curvature, s is the path, and l is the total pathlength. The curvature has a meaning of the tangential angle θ change rate along the path, that is $\kappa = d\theta/ds$.

Equation (3.2) is solved by means of variational analysis. Requiring $\delta E = 0$ leads to an Euler-Lagrange equation, which solution is a general clothoid (also known as Euler or Cornu spiral), $\kappa = k_0 + k_1 s$. However, this equation does not include endpoint constraints as the only constraints are in terms of the curvature. This has been solved by including Lagrange multipliers λ_i into (3.2), and solving a more general functional

$$E'_{MVC} = \int_0^l \left[\left(\frac{\partial\kappa}{\partial s}\right)^2 + \lambda_1 \sin\theta(s) + \lambda_2 \cos\theta(s)\right] ds. \tag{3.3}$$

Details on solving (3.3) can be found in (86; 85). The final solution for κ is a higher order polynomial, and in order to fit the solution to an S-bend connecting two branches of a two-dimensional spiral, polynomial of a 4th order,

$$\kappa(s) = a_0 + a_1 s + a_2 s^2 + a_3 s^3 \tag{3.4}$$

with parameters a_i, is required. This leaves a set of 5 unknowns $(a_1, a_2, a_3, \theta_0, s)$, which match 5 continuity constraints: position (x_1, y_1), tangential angle θ_1, curvature κ, and curvature derivative κ'. The algorithm gives only one branch of the S-bend while the second is obtained by inversion. The continuity of κ' has been imposed by Chen *et al.* (85) for multimode waveguides due to a particular application on a whispering gallery S-bend. The authors have noted that it is necessary in order to avoid inter-modal coupling, and it is probably not required in single-mode waveguides. Nevertheless, the design algorithm was adopted in this work in full.

Five equations then relate the parameters to the constraints (85). With some manipulation, the following equations can be obtained

$$\begin{aligned}
\theta_0 &= \theta_1 - \frac{2}{3}\kappa_1 s_1 + \frac{1}{6}\kappa_1' s_1^2 - \frac{1}{12}a_3 s_1^4 \\
a_2 &= -\frac{\kappa_1}{s_1^2} + \frac{\kappa_1'}{s_1} - 2a_3 s_1, \\
a_1 &= \kappa_1' - 2a_2 s_1 - 3a_3 s_1^2, \\
x_0 &= \int_0^l \cos\theta(s) ds x_1, \\
y_0 &= \int_0^l \sin\theta(s) ds y_1,
\end{aligned} \tag{3.5}$$

where s_1 is the pathlength at (x_1, y_1) and the start point was set (x_0, y_0). These equations are directly suited for numerical implementation. It can be observed that only a_3 and s_1 need to be guessed, which is a great simplification as opposed to guessing all 5 unknowns. The equations are highly unstable, and the provided guesses needs to be very accurate despite of guessing only 2 parameters.

Moreover, the adiabatic connections were extended also to the outputs from the spiral, which constraints θ_0. This requires one order higher polynomial than (3.4) and introduces a sixth unknown a_4. The following equations

$$\begin{aligned}
a_3 &= 12\frac{(\theta_1 - \theta_0)}{s_1^4} - 8\frac{k_1}{s_1^3} + 2\frac{dk_1}{s_1^2} - \frac{12}{5}a_4 s_1 \\
a_2 &= -\frac{\kappa_1}{s_1^2} + \frac{\kappa_1'}{s_1} - 2a_3 s_1 - 3a_4 s_1^2 \\
a_1 &= \kappa_1' - 2a_2 s_1 - 3a_3 s_1^2 - 4a_4 s_1^3
\end{aligned} \tag{3.6}$$

then need to be solved together with the (x, y) conditions from Equations (3.5).

These adiabatic transitions were implemented in mask designs in this work in order to prevent the situation illustrated in Fig. 3.2. The essential part of the code that solves these equations is provided in Appendix D.

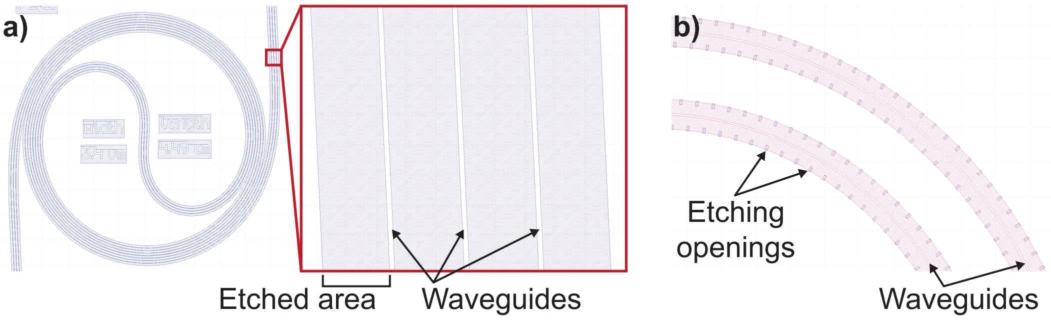

Figure 3.3: Elements of mask designs. **a)** A spiral with a master waveguide (middle) and two offset waveguides. **b)** A waveguide in the central S-bend of a spiral followed by etching openings on both sides.

3.2.3 Aligning Other Objects to the Waveguides

In order to fabricate the the free-standing waveguides, the mask had to consist of two layers. First for the waveguides and second for the etching openings, which need to exactly follow the waveguides. This was automatised with few functions.

Aligning the etching openings involves tracing the original path first. This itself allows to pattern multiple waveguides next to each other. Several waveguides can be placed into a single spiral, as shown in Fig. 3.3a, which is a sample from the mask design for Paper I. Another option is then placing oriented objects of arbitrary shapes along the waveguide as can be seen in Fig. 3.3b. This was used in Paper III in order to under-etch the waveguides. The script for generating the offset paths and etching openings positions is provided in Appendix E.

4

Methods of Waveguide Fabrication

Waveguides are typically patterned into thin films of optically transparent materials. In general, waveguide fabrication involves the following steps:

Thin layer deposition,

lithography, and

etching.

The choice of materials will follow the requirements imposed by the application, which also includes a particular wavelength. Based on discussions in chapter 2, the selected materials need to be transparent and provide a refractive index contrast for waveguiding. Lithography method will be selected based on aspects like minimum feature dimension in the design, and feasibility of iterative design adjustment. The latter pertains to research and development, where iterations between fabrication and testing are imperative to achieving optimal results. Last, the methods of etching have to meet criteria such as isotropicity, and selectivity towards different materials.

The fabrication of waveguides in this thesis was conducted in two nanofabricaiton facilities: the Optoelectronics Research Centre in Southampton, UK, and Nanolab at NTNU, Trondheim, Norway. Most deposition was done with physical vapour deposition (PVD) methods of sputtering and evaporation.

Optical waveguide at MIR wavelength feature relatively large dimensions. This provides a benefit in using UV photolithography, which is commonly available in foundries used also for MEMS. There are exceptions, such as the slot waveguide, for which DUV photolithography, or electron beam lithography is required, but such structures were not a part of the fabrication in this thesis. Dimensions of all the patterns within this work were 1 µm or larger.

Details, of nanofabrication methods can be found in textbooks such as (87), and there is no need for detailed description of all the processing steps. Nevertheless, etching is given more attention in the next section because etching optimisation was a great part of this thesis.

4.1 Etching

Etching is a process of removing a material, typically at a controlled rate, and transferring a certain pattern from a mask into the the underlying layers. The techniques are categorised based on the phase of the etchant into *wet* and *dry* etching, or based on the process isotropy into *isotropic* and *anisotropic*. The next sections of this chapter will describe selected etching techniques. Most attention is given to those used for fabricating the suspended waveguides, which are the main subject of this thesis.

4.1.1 Anisotropic Etching

Isotropy of etching depends on the material, the etchant, and the method. For example, crystalline silicon is etched anisotropically in potassium hydroxide (KOH) and tetramethyl ammonium hydroxide (TMAH), and isotropically in HNA (HF + HNO_3 + diluent). These methods are not so common for waveguide fabrication, which pattern transfer often requires vertical etching over the whole substrate independently of the pattern orientation.

Vertical etching can be achieved with dry etch methods, which are typically the choice in nanophotonics. In particular, plasma etching has become crucial to structuring optical waveguides and integrated lasers.

4.1.1.1 Ion beam milling (IBM)

IBM is a straightforward method for obtaining vertical profiles through a purely physical process. Argon plasma is struck above the target in an evacuated reactor, and high energy ions are ejected and bombard the substrate. The substrate material is then sputtered away, and patterns are transferred from a photoresist into a device layer.

IBM has been used for making optical waveguides (88; 89), and also applied for defining rib waveguides and etching openings in Paper I. However, this method causes material redeposition. The sputtered material is deposited onto the sidewalls of the resist and it does not get removed with the resist removal (90; 91). This issue is further discussed in Paper III.

it is etched represents an anisotropic etchant. On the other hand, both KOH and TMAH will be isotropic towards amorphous silicon or aluminium oxide (Al_2O_3) (92). In dry etching, isotropic behaviour is achieved with e.g. XeF_2 or SF_6 plasma while anisotropic etching is achieved in reactive ion etching with carbon-containing chemistries. In the latter case, carbon together with fluorine or chlorine polymerises on the substrate surface, and the process can be tuned to yield nearly perfect vertical profiles.

4.1.1.2 Reactive Ion Etching (RIE)

RIE also utilises plasma in a reactor under a vacuum, but in this case, reactive species are generated from suitable feed gases. Nowadays, the most common chemistries are based on fluorocarbon gases such as CF_4, CHF_3, etc. The reactive species, such as fluorine radicals, then react with the substrate material to form more stable products such as SiF_4 from silicon or TaF_5 from Ta_2O_5. In a contrast to physical etching described above, this etching is chemical because of the reactions between the plasma species and the substrate. It is important that the final products are volatile under the low pressure in order to be exhausted away.

RIE can also induce physical etching. The dominant etching component depends on the process parameters: pressure (typically in units or tens of m), applied power, gas flow, and the chemistry. In RIE processing, material can be also deposited, e.g., a polymer film formed from the fluorocarbon gases. Finding a proper balance between the deposition rate and the etch rate can ensure vertical etching with no redeposition (93; 94). This was done in Paper III, which compares RIE and IBM results. The next section shows application of RIE on mesoporous TiO_2, which is a subject of Paper II.

4.1.1.3 Application of RIE to Mesoporous TiO_2 Waveguides

Titanuim dioxide is one of the transparent dielectrics which is suitable for optical waveguides with transparency ranging from 400 nm to 400 µm (95). Its refractive index takes values from 2.2 to 2.4. Waveguides have been prepared on lithium niobate susbtrate for optical switching by the electro-optical modulation (95). SU8 resist has also been used as a substrate enabling flexible biocompatible waveguide chips (96) with $11(2)\,\mathrm{dB\,cm^{-1}}$. Spectral broadening of femtosecond laser pulses has been observed in TiO_2 on SiO_2 waveguides, showing the potential of titania for nonlinear optics (97). TiO_2 strip waveguides (98) ($2.4(2)\,\mathrm{dB\,cm^{-1}}$) and slot waveguide resonators (99) ($Q = 740\,\mathrm{nm}$) on SiO_2 have been demonstrated for $1.55\,\mu\mathrm{m}$ and visible wavelengths respectively.

In Paper II, we have used mesoporous titania for optical waveguide fabrication. The work is unique in that the mesoporous titania constitutes the waveguide cores instead of claddings, which are more common (100). The waveguide characterisation is detailed in the attached paper, and it is not repeated her. The top-down waveguide fabrication, however, was a part of this thesis, and this section provides partial results from the processing. It is not a comprehensive study, but a random search approach, which resulted in reasonable structures as observed an SEM.

TiO_2 waveguides have been prepared by lift-off (95), but reactive ion etching is the preferred method. Different chemistries have been used, including $SF_6/O_2/Ar$ (98; 99), CF_4/Ar (101), and $CF_4/O_2/Ar$. Norasetthekul *et al.* (102) have shown that etch rates in SF6/Ar and Cl2/Ar chemistries are much higher than in Ar ion beam milling, yield smooth morphologies and highly anisotropic features with photoresist patterning.

The TiO_2 waveguides of Paper II were fabricated in Nanolab (NTNU, Trondheim, Norway). Lithographic patterning was done with a positive photoresist and a maskless aligner (MLA150, Heidelberg instruments). Table summarises the patterning protocol.

After resist developing, the pattern was transferred into the device layer by ICP–RIE (ICP–RIE, Plasmalab System 100 ICP–RIE 180). 15 etching recipes were tested in total in order to meet several requirements at once: smooth surface finish, no redeposition of the etched material (discussed in Paper II), low etch rate for controllable shallow etching, and vertical sidewalls.

Samples from the recipe development are displayed in Fig. 4.1. Sample A exhibited excessive redeposition, which can be avoided by suppressing the physical etching component. Sample B was exposed to more reactive chemistry in order to avoid redeposition but it shows micrograss on top of the etched surfaces. This is again avoidable by tuning the recipe: either increasing ICP or RF power, or decreasing pressure. The micrograss was effectively suppressed in all other recipes. Recipe C resulted in too high etch rate, and it would be difficult to achieve only $70\,\mathrm{nm}$ to $100\,\mathrm{nm}$ deep etch. Recipe D yielded slanted sidewalls, and final adjustments were made towards recipe E, which was applied to the waveguide fabrication.

It cannot be said that the final recipe is optimal. It would be beneficial to further reduce the

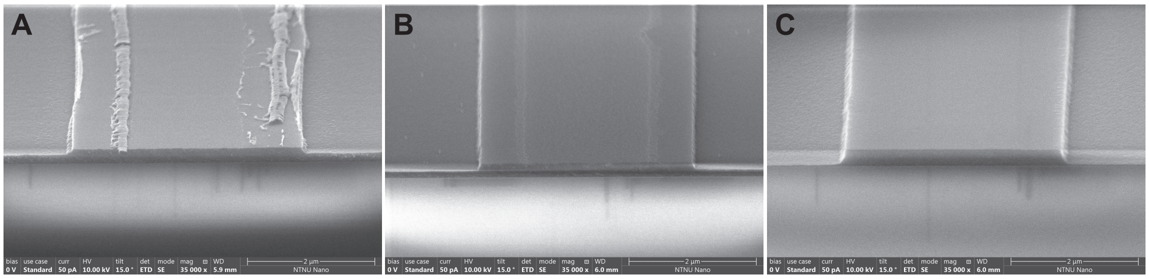

CHF_3/Ar	40/10 sccm	CHF_3/SF_6	25/25 sccm	$CHF_3/SF_6/Ar$	20/25/5 sccm
p	20 mTorr	p	20 mTorr	p	15 mTorr
RF power	50 W	RF power	50 W	RF power	100 W
ICP power	1000 W	ICP power	600 W	ICP power	1400 W
DC bias	166 V	DC bias	254 V	DC bias	235 V
Etch rate	101 nm/min	Etch rate	130 nm/min	Etch rate	506 nm/min

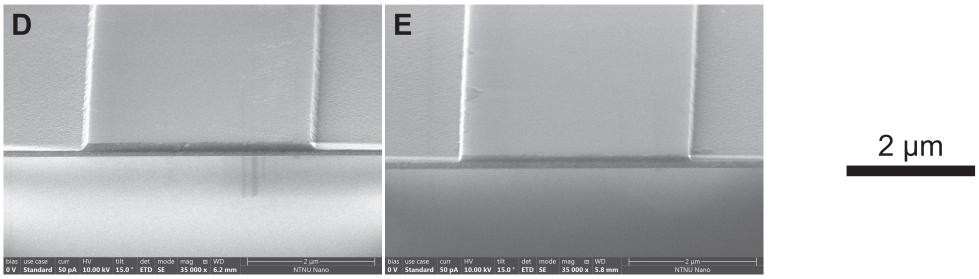

$CHF_3/SF_6/Ar$	20/25/5 sccm	CHF_3/O_2	48/2 sccm
p	30 mTorr	p	20 mTorr
RF power	200 W	RF power	100 W
ICP power	1000 W	ICP power	1000 W
DC bias	583 V	DC bias	250 V
Etch rate	263 nm/min	Etch rate	277 nm/min

Figure 4.1: Illustration of the TiO_2 etching recipe development. Images were taken with a 15°, and the scale bar applies to all images.

etch rate, possibly by switching off the ICP unit completely, to have a better control over shallow etching. More vertical sidewalls could be also achieved through adjusting the chemistry, to obtain better ratio between sidewall passivation and its removal (93). It is also expectable that the etching of a mesoporous material is faster. Hence the findings here are not directly applicable to a non-porous titania.

4.1.2 Isotropic etching

Dry etching can yield isotropic profiles irrespective of the amorphous or crystalline nature of the substrate. This section provides a background of XeF_2 molecular gas and SF_6 etching, which were used for under-etching Ta_2O_5 in Papers I and III.

4.1.2.1 XeF_2 gas

Fluorine is a highly reactive element. In connection with microfabrication, it has been widely studied since the late 1970s (103) as a simple and mechanically gentle alternative to plasma and wet etching of Si that does not leave residues on the etched surface. The fluoride is a white crystalline solid that sublimates until 3.8 at room temperature. It spontaneously attacks Si at room temperature in contrast to fluoride plasmas where free radicals first need to be generated. The etching follows these five steps:

1. Nondissociative adsorption,
2. dissociative adsorption,
3. formation of product molecule,
4. desorption of product molecule, and
5. residue removal,

where the residues are simply xenon molecules.

The early fundamental studies of XeF_2 plasma-less silicon etching were concerned with temperature dependences and relation to other fluorinating agents not requiring plasma. It has been found that XeF_2 etches Si about 10 times faster than F atoms at room temperature whereas F_2 is an even slower etchant than F (104). At low temperatures, the etching is dominated by a physisorbed XeF_2 layer whereas it is a direct impact at high temperatures. The comparison has been further extended to include ClF_3, BrF_3, BrF_5, IF_5, and ClF, and among all these compounds, XeF_2 has still the highest reaction probability (105).

While Si gets etched rapidly, some materials like SiO_2, Si_3N_4, Al_2O_3, or photoresists are resistant to XeF_2 or at least etched much slower than Si. There is numerous evidence in the literature to support the resistance of the above-mentioned materials, but the Si compounds hold a special place. Initially, they appeared to be absolutely resistant to XeF_2 (103; 104) unless electron or ion beam assisted the etching. This discrepancy has been settled later by a so-called *proximity effect* (106). The XeF_2–Si interaction produces highly energetic F atoms which consequently attack other materials, namely SiO_2 in the study. Despite the knowledge that has been acquired about XeF_2 over the past decades, little is known about XeF_2–Ta_2O_5 interaction.

Nowadays it is known that SiO_2 and Si_3N_4 are etched by XeF_2 with Si selectivity, although it varies greatly in literature, around $1000:1$. The authors revealed that XeF_2-Si interaction induces formation of unstable XeF molecules which quickly dissociate in a gas-phase, leaving a fast-moving F radical that eventually attacks SiO_2. Despite of the knowledge about the resistant materials, interaction of XeF_2 with tantalum pentoxide (Ta_2O_5) was not yet explored to the best of my knowledge.

4.1.2.2 SF_6 Plasma

Besides XeF_2, another method to etch crystalline silicon isotropically is pure SF_6 plasma. Many nanofabrication facilities are equipped with inductively coupled plasma reactive ion etching (ICP–RIE) instruments, and they prove to be crucial for making nanophotonic components. Typical applications for nanophotonics is vertical etching. This is necessary for making majority of optical waveguides which often require vertical sidewalls. The application here requires relies on the ICP in ICP–RIE. RIE uses 2 electrodes, 1 above and 1 below the sample. These 2 electrodes then deliver the energy to the gas in order to ionise it, and hence strike and maintain the plasma. At the same time, the voltage maintained between these 2 electrodes accelerates the ionised species towards the specimen and is responsible for the vertical etching discussed above. In order to achieve isotropic etching, it is necessary to circumvent this behaviour and that's where ICP. ICP maintains plasma within a cylindrical chamber situated above the sample and without the RIE operating, it does not cause any bias in the plasma and thus the ions are not accelerated to the specimen. This then results in isotropic etching or even a deposition from a fluorocarbon precursor.

Isotropic etching with SF_6 plasma has been studied e.g., (107; 108), and it is further discussed and applied to Ta_2O_5 under-etching in Paper III.

5

Waveguide Characterisation

This chapter mainly describes the spectroscopy setups used for measurements in Papers I and II. Propagation loss measurements were done with the same setups described here, and two methods were used throughout this work: i) By recording and analysing light scattered out of the waveguide plane, which was used in all of the attached Papers. ii) By the cutback method Paper III.

5.1 Experimental Setups for Chip-Based TDLAS

Our experimental setups were designed for characterisation of waveguide performance in gas detection. Two separate setups were constructed for MIR and NIR, and both were used with acetylene in the experiments related to this thesis. The air-suspended Ta_2O_5 rib waveguide reported in Paper I was characterised in the MIR setup experiments with acetylene and the NIR setup was used in spectroscopic experiments with a mesoporous TiO_2 waveguide in Paper II.

5.1.1 MIR Setup

Fig. 5.1 shows schematics of the MIR TDLAS experimental setup. A custom LabVIEW software, obtained from Herbert Looser (UAS Northwestern Switzerland) and adapted by Anurup Datta (postdoc, UiT), controls a field-programmable gate array (FPGA; National Instruments, PCIe-7857) and mass flow controllers (Bronkhorst, EL-FLOW Select). It further handles processing of data returned by the FPGA, which has a sampling rate of 1 MHz, not attainable by a standard

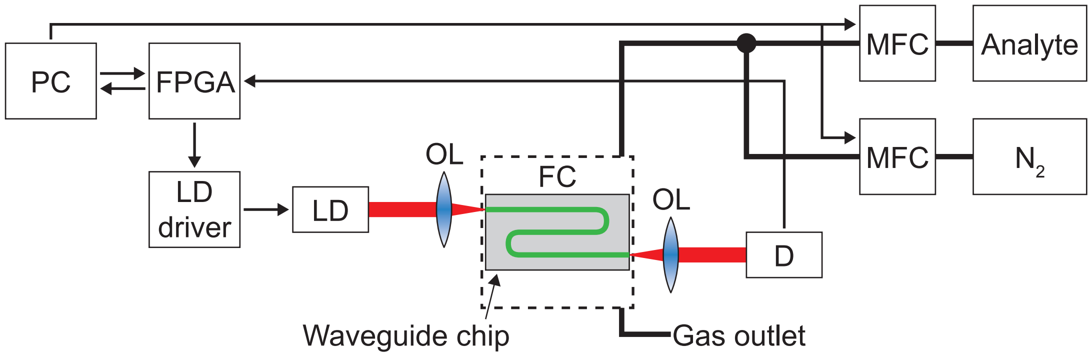

Figure 5.1: Schematics of the MIR TDLAS experimental setup. LD – laser diode, OL – objective lens, FC – flow cell, – D detector, – MFC – mass flow controller.

computer. Therefore, it allows fast laser control and detector signal read-out.

Besides the FPGA and MFCs, the setup includes a DFB laser diode (nanoplus) emitting at 2566 nm. This laser allows mode-hop-free tuning, has a maximum power of ≈13.5 mW, line FWHM below 3 MHz (66 fm or 10^{-4} cm^{-1}) and current tuning coefficient around 0.2 nm mA^{-1}. The transmitted light is detected with a mercury cadmium telluride (MCT) single-pixel detector (VIGO). Finally, an in-house aluminium flow cell shown in Fig. 5.2 is housing the chip to ensure controlled gas concentration during experiments. Flow cell windows are covered with microscope cover slips and the contact between the top and bottom part is sealed with PDMS. The top window allows to image the chip with a MIR camera (Telops), visible in Fig. 5.3, to facilitate coupling while the waveguide chip is inside. The camera is equipped with an InSb chip, Stirling cooling, and a long distance objective lens ($M = 4$, WD = 3 cm). According to the camera specifications, the InSb chip is sensitive in 3 µm–5 µm wavelength range but it detects 2566 nm light efficiently (109).

Prior to the gas detection experiment, the digital frequency was converted into wavenumbers using a 5 mm thick silicon etalon (Fig. 5.4a). An N_2 background spectrum was then acquired and fitted with a polynomial function, which was used for normalisation. The normalisation eliminates unwanted water peaks and corrects the amplitude modulation but a baseline drift can occur during the gas detection experiment. This drifting is corrected by the data fitting, and hence it causes no complication.

The FPGA was programmed to tune the current with a saw signal interlaced with cooling gaps ($I = 0$ A) as indicated in Fig. 5.4b. Although the tuning is done via current modulation, the wavelength is affected by immediate temperature changes in the laser, and the cooling step ensures larger wavelength tuning range as compared to a situation with no cooling. The FPGA was also programmed to acquire 16 baseline samples from the detector while the laser

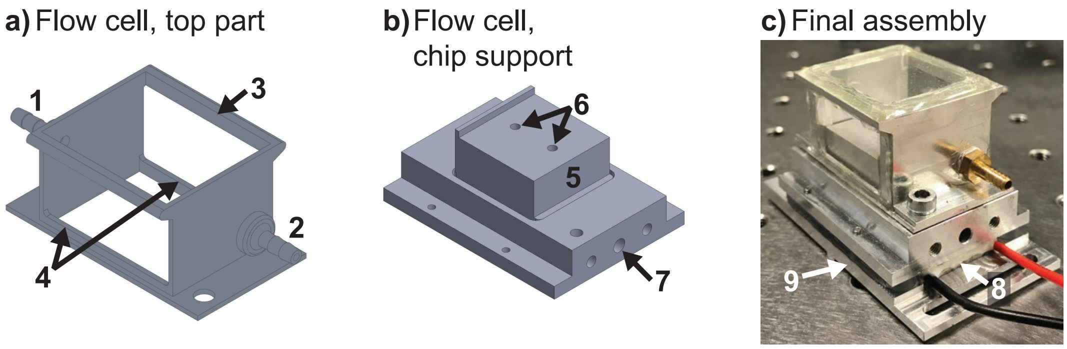

Figure 5.2: Flow cell for chip-based spectroscopy experiments, dimensioned for 2 cm long waveguides. **a)** Top part of the flow cell with 1 – gas inlet, 2 – gas outlet, 3 – side windows for end-fire light coupling, 4 – top window for chip imaging. **b)** Lower part of the flow cell for chip support. 5 – vacuum chuck, 6 – pump inlet, 7 – pump outlet. **c)** Final cell assembly made of duralumin. 8 – Peltier device, 9 – mounting plate. The mounting plate allows to fasten the whole cell in the TDLAS setups.

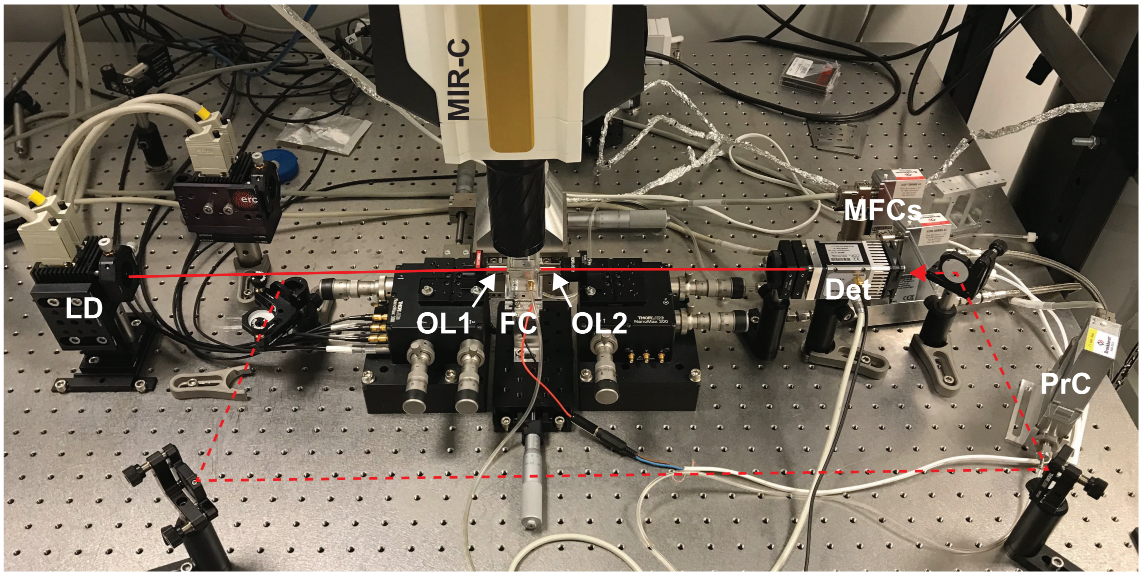

Figure 5.3: Photograph of the MIR TDLAS setup. LD – laser diode (DFB), OL1/OL2 – objective lenses (aspherical, OL1 = OL2), FC – the flow cell, Det – detector, MFCs – mass flow controllers, PrC – pressure controller, and MIR-C – MIR camera (MIR-C). The laser beam path is outlined in red, and the dashed line marks an alternative path for in-coupling from the back.

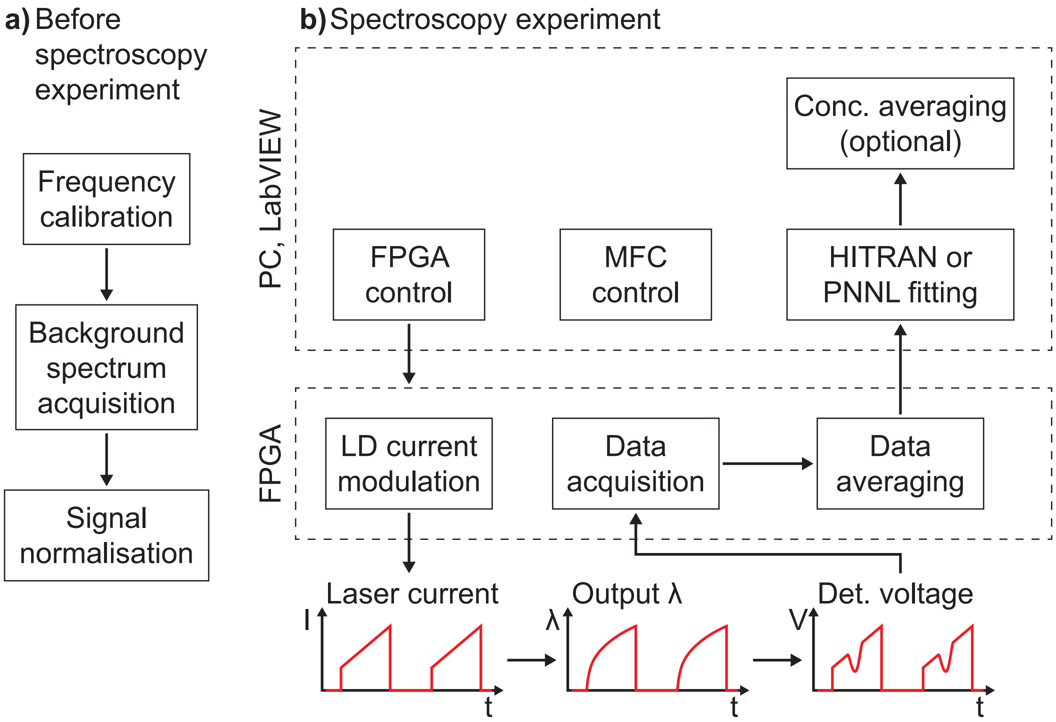

Figure 5.4: Data acquisition and processing in TDLAS experiments. **a)** Prior to the spectroscopy, the digital sampling is converted into wavenumber, and the acquired signal is normalised with pure N_2 background spectrum. **b)** Spectroscopy experiment procedure.

was off, and a total of 512 points were acquired per one current ramp.

Checking the baseline signal of the detector (zero LD driving current) ensured that the total magnitude of the signal was always found because the detector baseline is not zero and drifts over time. Note that this is different from the signal baseline described above. The signal baseline drift can originate e.g., from temporal waveguide coupling misalignment while detector drift is a property of the detector, primarily due to a dark current and a detector bias voltage. The two were corrected separately as explained here.

Collected data were averaged within the FPGA every 512 scans and only then passed to the computer. Data fitting was performed in the LabVIEW software, which has the capability of fitting both with HITRAN and PNNL data. However, the targeted acetylene Q branch of the first overtone at 2566 nm was not accurately predicted by HITRAN and the resulting peak (combination of several lines) had a different shape. For this reason, we fitted this peak with the experimental PNNL data (obtained at 10 % concentration and standard conditions) by simple scaling to obtain the best fit (least mean squares).

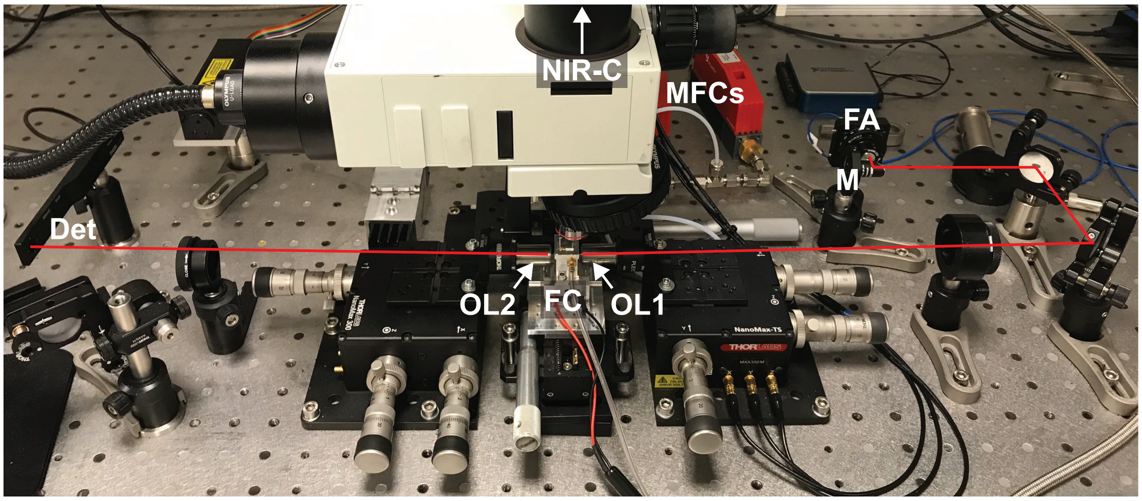

Figure 5.5: Photograph of the NIR TDLAS setup. PMF – polarisation-maintaining fibre, FA – fibre adapter, M – parabolic mirror, OL1 – objective lens, OL2 – objective lens, FC – flow cell, Det – detector, MFCs – mass flow controllers, and NIR-C – NIR camera. with a NIR camera (NIR-C). The laser beam path is outlined in red.

5.1.2 NIR setup

There were few differences in the NIR setup, captured in Fig. 5.5, compared to the MIR setup. Firstly, a tuneable external cavity laser diode (EXFO, T100S-HP-CLU-M) with a fibre-coupled output (polarisation maintaining, PM) was used. This laser covers a range of 1500 nm–1680 nm with a maximum tuning speed of 100 nm, limited by mechanical movement of a diffraction grating. The output of the PM fibre was then collimated with a parabolic mirror and navigated with a series of silver-coated mirrors to the chip. Chip coupling was done via aspheric lenses (Thorlabs, C240TMD-C, NA = 0.5), and the signal was detected with a Ge photodiode power sensor (Thorlabs, S132C). The chip was imaged with a NIR camera (Raptor photonics, Ninox 640), which uses an InGaAs detector. The laser wavelength was tuned directly with the laser controller and appropriate triggering signals were sent to a data acquisition device (DAQ; National Instruments, USB-6000, 5 kHz sampling rate) to synchronise the data collection.

Similarly to the MIR setup, precise wavelength/wavenumber was found with a 5 mm etalon. The laser tuning was significantly slower than with the DFB laser, and only allowed to collect approximately one scan per second. Data acquisition and fitting was performed with the same LabVIEW software, while HITRAN database parameters were used in this case.

6

Conclusion and Outlook

This work covers several aspects of optical waveguides for trace gas detection in the infrared domain. It first elaborates on the waveguide design where the light–analyte interaction is the key factor but other effects have to be considered in order to achieve optimal performance. These include loss mechanisms such as lateral leakage and substrate leakage, which are usually not encountered at shorter wavelengths and more established applications such as telecommunication.

In Paper I, we demonstrated an outstanding spectroscopic performance of the tantalum pentoxide free-standing waveguides. The confinement factor of 107 % was measured in a spectroscopic experiment with acetylene, where it was clearly observable that the response is stronger than in a free space. Because the guided mode has a very low effective index, below 1.1, etalon effects from the waveguide were suppressed, and no filtering was needed. Paper III compares two fabrication methods for free-standing waveguides, namely XeF_2 molecular gas etching, and SF_6 plasma. It was found that material selectivity limits the first of them, while SF_6 plasma can leave residues, which need further processing. Nevertheless, both challenges were solved, and functional waveguides were demonstrated. Lastly, Paper II shows a different approach to waveguide-based gas sensing. It demonstrates a porous material, where the porosity does not hinder the light guiding, and allows spectroscopic detection within its volume.

Future work will involve minimising propagation losses in the Ta_2O_5 free-standing waveguide, which are believed to originate mainly from residual water and OH bonds. It is also intriguing to apply the fabrication methods developed here to other materials such as Al_2O_3 and Si_3N_4, and create a photonic crystal free-standing waveguide, which could mitigate the lateral leakage.

References

[1] Qiancheng Ma. Greenhouse Gases: Refining the Role of Carbon Dioxide, March 1998.

[2] Worl Meteorological OrganizationOrganization. *WMO Greenhouse Gas Bulletin (GHG Bulletin) - No. 16 : The State of Greenhouse Gases in the Atmosphere Based on Global Observations through 2019*. WMO, Geneva, 2020.

[3] Achuthanunni Chokkathukalam, Dong-Hyun Kim, Michael P Barrett, et al. Stable isotope-labeling studies in metabolomics: new insights into structure and dynamics of metabolic networks. *Bioanalysis*, 6(4):511–524, February 2014.

[4] Peng Wang, Longyun Guo, Rohit Jaini, et al. A 13C isotope labeling method for the measurement of lignin metabolic flux in Arabidopsis stems. *Plant Methods*, 14(1):51, December 2018.

[5] Min Yuan, Daniel M. Kremer, He Huang, et al. Ex vivo and in vivo stable isotope labelling of central carbon metabolism and related pathways with analysis by LC–MS/MS. *Nature Protocols*, 14(2):313–330, February 2019.

[6] Alexander Tøsdal Tveit, Tilman Schmider, Anne Grethe Hestnes, et al. Simultaneous Oxidation of Atmospheric Methane, Carbon Monoxide and Hydrogen for Bacterial Growth. *Microorganisms*, 9(1):153, January 2021.

[7] Alexander Tøsdal Tveit, Tim Urich, Peter Frenzel, and Mette Marianne Svenning. Metabolic and trophic interactions modulate methane production by Arctic peat microbiota in response to warming. *Proceedings of the National Academy of Sciences*, 112(19):E2507–E2516, May 2015.

[8] A. Kannath and H. N. Rutt. Development of low cost instrumentation for non-invasive detection of Helicobacter pylori. page 64300L, San Jose, CA, February 2007.

[9] Jill D. Fenske and Suzanne E. Paulson. Human Breath Emissions of VOCs. *Journal of the Air & Waste Management Association*, 49(5):594–598, May 1999.

[10] Stuart Chen, Leslie Zieve, and V. Mahadevan. Mercaptans and dimethyl sulfide in the breath of patients with cirrhosis of the liver: Effect of feeding methionine. *The Journal of Laboratory and Clinical Medicine*, 75(4):628–635, April 1970. Publisher: Elsevier.

[11] Paul R. Mahaffy, Christopher R. Webster, Michel Cabane, et al. The Sample Analysis at Mars Investigation and Instrument Suite. *Space Science Reviews*, 170(1-4):401–478, September 2012.

[12] Joanna Kamieniak, Edward P. Randviir, and Craig E. Banks. The latest developments in the analytical sensing of methane. *TrAC Trends in Analytical Chemistry*, 73:146–157, November 2015.

[13] Emily J. Chua, William Savidge, R. Timothy Short, et al. A Review of the Emerging Field of Underwater Mass Spectrometry. *Frontiers in Marine Science*, 3, 2016.

[14] E. Baudet, A. Gutierrez-Arroyo, M. Baillieul, et al. Development of an evanescent optical integrated sensor in the mid-infrared for detection of pollution in groundwater or seawater. *Advanced Device Materials*, 3(2):23–29, October 2017.

[15] Mingzhou Jin, Feng Lu, and Mikhail A Belkin. High-sensitivity infrared vibrational nanospectroscopy in water. *Light: Science & Applications*, 6(7):e17096–e17096, July 2017.

[16] I.E. Gordon, L.S. Rothman, C. Hill, et al. The HITRAN2016 molecular spectroscopic database. *Journal of Quantitative Spectroscopy and Radiative Transfer*, 203:3–69, December 2017.

[17] J. Barry McManus, Mark S. Zahniser, David D. Jr. Nelson, et al. Application of quantum cascade lasers to high-precision atmospheric trace gas measurements. *Optical Engineering*, 49(11):111124, November 2010.

[18] Lars Nähle, Lars Hildebrandt, Martin Kamp, and Sven Höfling. INTERBAND CASCADE LASERS: ICLs open opportunities for mid-IR sensing, May 2013.

[19] Jerry Meyer, William Bewley, Chadwick Canedy, et al. The Interband Cascade Laser. *Photonics*, 7(3):75, September 2020.

[20] Jane Hodgkinson and Ralph P Tatam. Optical gas sensing: a review. *Measurement Science and Technology*, 24(1):012004, January 2013.

[21] Eric J. Zhang, Yves Martin, Jason S. Orcutt, et al. Trace-gas Spectroscopy of Methane using a Monolithically Integrated Silicon Photonic Chip Sensor. In *Conference on Lasers and Electro-Optics*, page STh1F.2, San Jose, California, 2019. OSA.

[22] Aditya Malik, Alexander Spott, Eric J. Stanton, et al. Integration of Mid-Infrared Light Sources on Silicon-Based Waveguide Platforms in 3.5–4.7 \si{\micro\metre} Wavelength Range. *IEEE Journal of Selected Topics in Quantum Electronics*, 25(6):1–9, November 2019.

[23] Eric Stanton, Alexander Spott, Jon Peters, et al. Multi-Spectral Quantum Cascade Lasers on Silicon With Integrated Multiplexers. *Photonics*, 6(1):6, January 2019.

[24] Parthasarathy Srinivasan, Madeshwari Ezhilan, Arockia Jayalatha Kulandaisamy, et al. Room temperature chemiresistive gas sensors: challenges and strategies—a mini review. *Journal of Materials Science: Materials in Electronics*, 30(17):15825–15847, September 2019.

[25] Weiwei Cai, Oliver Vanderpoorten, and Clemens Kaminski. Tomographic absorption spectroscopy based on wavelength modulation and multi-harmonic detections. In *Imaging and Applied Optics 2016*, page JT3A.19, Heidelberg, 2016. OSA.

[26] A. Inberg, M. Oksman, M. Ben-David, and N. Croitoru. Hollow Waveguide for Mid and Thermal Infrared Radiation. *Journal of Clinical Laser Medicine & Surgery*, 16(2):127–133, April 1998.

[27] Nathan Li, Lei Tao, Hongming Yi, et al. Methane detection using an interband-cascade LED coupled to a hollow-core fiber. *Optics Express*, 29(5):7221, March 2021.

[28] Bruce T. Thompson, A. Inberg, N. Croitoru, and Boris Mizaikoff. Characterization of a Mid-Infrared Hollow Waveguide Gas Cell for the Analysis of Carbon Monoxide and Nitric Oxide. *Applied Spectroscopy*, 60(3):266–271, March 2006.

[29] L. Tamina Hagemann, Sonja Ehrle, and Boris Mizaikoff. Optimizing the Analytical Performance of Substrate-Integrated Hollow Waveguides: Experiment and Simulation. *Applied Spectroscopy*, 73(12):1451–1460, December 2019.

[30] Julius Adams Stratton. *Electromagnetic theory*. McGraw-Hill, New York, 2012. OCLC: 838914255.

[31] Ginés Lifante. *Integrated photonics: fundamentals*. J. Wiley, Hoboken, NJ, 2003.

[32] John D. Joannopoulos, Steven G. Johnson, Joshua N. Winn, and Robert D. Meade. *Photonic crystals: molding the flow of light*. Princeton University Press, Princeton Oxford, 2nd edition edition, 2008. OCLC: 255634213.

[33] Robert Halir, Przemek J. Bock, Pavel Cheben, et al. Waveguide sub-wavelength structures: a review of principles and applications. *Laser & Photonics Reviews*, 9(1):25–49, January 2015.

[34] T.D. Visser, H. Blok, B. Demeulenaere, and D. Lenstra. Confinement factors and gain in optical amplifiers. *IEEE Journal of Quantum Electronics*, 33(10):1763–1766, October 1997.

[35] Christian Ranacher, Cristina Consani, Andreas Tortschanoff, et al. Mid-infrared absorption gas sensing using a silicon strip waveguide. *Sensors and Actuators A: Physical*, 277:117–123, July 2018.

[36] Christian Ranacher, Cristina Consani, Natalie Vollert, et al. Characterization of Evanescent Field Gas Sensor Structures Based on Silicon Photonics. *IEEE Photonics Journal*, 10(5):1–14, October 2018.

[37] Jacob T. Robinson, Kyle Preston, Oskar Painter, and Michal Lipson. First-principle derivation of gain in high-index-contrast waveguides. *Optics Express*, 16(21):16659–16669, October 2008.

[38] Isabelle Dicaire, Alfredo De Rossi, Sylvain Combrié, and Luc Thévenaz. Probing molecular absorption under slow-light propagation using a photonic crystal waveguide. *Optics Letters*, 37(23):4934, December 2012.

[39] Sara Ek, Per Lunnemann, Yaohui Chen, et al. Slow-light-enhanced gain in active photonic crystal waveguides. *Nature Communications*, 5(1), December 2014.

[40] Kuanping Shang, Shibnath Pathak, Binbin Guan, et al. Low-loss compact multilayer silicon nitride platform for 3D photonic integrated circuits. *Optics Express*, 23(16):21334, August 2015.

[41] L. Tombez, E. J. Zhang, J. S. Orcutt, et al. Methane absorption spectroscopy on a silicon photonic chip. *Optica*, 4(11):1322, November 2017.

[42] Tong Chen, Hansuek Lee, and Kerry J. Vahala. Design and characterization of whispering-gallery spiral waveguides. *Optics Express*, 22(5):5196–5208, March 2014.

[43] Hansuek Lee, Tong Chen, Jiang Li, et al. Ultra-low-loss optical delay line on a silicon chip. *Nature Communications*, 3:867, May 2012.

[44] Richard Soref. Mid-infrared photonics in silicon and germanium. *Nature Photonics*, 4(8):495–497, August 2010.

[45] Thomas Schädle and Boris Mizaikoff. Mid-Infrared Waveguides: A Perspective. *Applied Spectroscopy*, 70(10):1625–1638, October 2016.

[46] Hongtao Lin, Zhengqian Luo, Tian Gu, et al. Mid-infrared integrated photonics on silicon: a perspective. *Nanophotonics*, 7(2):393–420, December 2017.

[47] Delphine Marris-Morini, Vladyslav Vakarin, Joan Manel Ramirez, et al. Germanium-based integrated photonics from near- to mid-infrared applications. *Nanophotonics*, 7(11):1781–1793, September 2018.

[48] Harry D. Downing and Dudley Williams. Optical constants of water in the infrared. *Journal of Geophysical Research*, 80(12):1656–1661, April 1975.

[49] Jordi Soler Penades, Ali Khokhar, Milos Nedeljkovic, and Goran Mashanovich. Low Loss Mid-Infrared SOI Slot Waveguides. *IEEE Photonics Technology Letters*, pages 1–1, 2015.

[50] Jeff Chiles and Sasan Fathpour. Silicon photonics beyond silicon-on-insulator. *Journal of Optics*, 19(5):053001, April 2017.

[51] Neetesh Singh, Alvaro Casas-Bedoya, Darren D. Hudson, et al. Mid-IR absorption sensing of heavy water using a silicon-on-sapphire waveguide. *Optics Letters*, 41(24):5776, December 2016.

[52] Yi Zou, Swapnajit Chakravarty, Parker Wray, and Ray T. Chen. Experimental demonstration of propagation characteristics of mid-infrared photonic crystal waveguides in silicon-on-sapphire. *Optics Express*, 23(5):6965, March 2015.

[53] Carlos Alonso-Ramos, Milos Nedeljkovic, Daniel Benedikovic, et al. Germanium-on-silicon mid-infrared grating couplers with low-reflectivity inverse taper excitation. *Optics Letters*, 41(18):4324–4327, September 2016.

[54] Papichaya Chaisakul, Vladyslav Vakarin, Jacopo Frigerio, et al. Recent Progress on Ge/SiGe Quantum Well Optical Modulators, Detectors, and Emitters for Optical Interconnects. *Photonics*, 6(1):24, March 2019.

[55] G. Z. Mashanovich, M. Nedeljkovic, J. Soler-Penades, et al. Group IV mid-infrared photonics [Invited]. *Optical Materials Express*, 8(8):2276–2286, August 2018.

[56] Nima Nader, Abijith Kowligy, Jeff Chiles, et al. Infrared frequency comb generation and spectroscopy with suspended silicon nanophotonic waveguides. *Optica*, 6(10):1269, October 2019.

[57] Alejandro Sánchez-Postigo, Juan Gonzalo Wangüemert-Pérez, Jordi Soler Penadés, et al. Mid-infrared suspended waveguide platform and building blocks. *IET Optoelectronics*, 13(2):55–61, April 2019.

[58] Wen Zhou, Zhenzhou Cheng, Xinru Wu, et al. Fully suspended slot waveguide platform. *Journal of Applied Physics*, 123(6):063103, February 2018.

[59] Aly Abdou, Parashara Panduranga, Jens Richter, et al. Air-clad suspended nanocrystalline diamond ridge waveguides. *Optics Express*, 26(11):13883–13890, May 2018.

[60] M. A. Webster, R. M. Pafchek, A. Mitchell, and T. L. Koch. Width Dependence of Inherent TM-Mode Lateral Leakage Loss in Silicon-On-Insulator Ridge Waveguides. *IEEE Photonics Technology Letters*, 19(6):429–431, 2007.

[61] Ronald K. Hanson, R. Mitchell Spearrin, and Christopher S. Goldenstein. *Spectroscopy and optical diagnostics for gases*. Springer, Cham, 2015. OCLC: 944218045.

[62] Timothy J. Johnson, Robert L. Sams, and Steven W. Sharpe. The PNNL quantitative infrared database for gas-phase sensing: a spectral library for environmental, hazmat, and public safety standoff detection. page 159, Providence, RI, March 2004.

[63] Laurence S. Rothman. History of the HITRAN Database. *Nature Reviews Physics*, April 2021.

[64] Steven W. Sharpe, Timothy J. Johnson, Robert L. Sams, et al. Gas-Phase Databases for Quantitative Infrared Spectroscopy. *Applied Spectroscopy*, 58(12):1452–1461, December 2004.

[65] Carolyn S. Brauer, Timothy J. Johnson, Thomas A. Blake, et al. The Northwest Infrared (NWIR) gas-phase spectral database of industrial and environmental chemicals: recent updates. page 910604, Baltimore, Maryland, USA, May 2014.

[66] Oguzhan Kara, Frazer Sweeney, Marius Rutkauskas, et al. Open-path multi-species remote sensing with a broadband optical parametric oscillator. *Optics Express*, 27(15):21358–21366, July 2019. Publisher: Optical Society of America.

[67] B. Tuzson, K. Zeyer, M. Steinbacher, et al. Selective measurements of NO, NO2 and NOy in the free troposphere using quantum cascade laser spectroscopy. *Atmospheric Measurement Techniques*, 6(4):927–936, April 2013.

[68] David S. Bomse, Alan C. Stanton, and Joel A. Silver. Frequency modulation and wavelength modulation spectroscopies: comparison of experimental methods using a lead-salt diode laser. *Applied Optics*, 31(6):718, February 1992.

[69] Béla Tuzson, Markus Mangold, Herbert Looser, et al. Compact multipass optical cell for laser spectroscopy. *Optics Letters*, 38(3):257, February 2013.

[70] Markus Mangold, Béla Tuzson, Morten Hundt, et al. Circular paraboloid reflection cell for laser spectroscopic trace gas analysis. *Journal of the Optical Society of America A*, 33(5):913, May 2016.

[71] Chu C. Teng, Eric J. Zhang, Chi Xiong, et al. Dynamic Optical Fringe Suppression for Silicon Photonic Sensors. In *Conference on Lasers and Electro-Optics*, page SW3L.7, San Jose, California, 2018. OSA.

[72] E.J. Zhang, L. Tombez, C.C. Teng, et al. Adaptive etalon suppression technique for long-term stability improvement in high index contrast waveguide-based laser absorption spectrometers. *Electronics Letters*, 55(15):851–853, July 2019.

[73] Wolfgang Demtröder. Nonlinear Spectroscopy. In *Laser Spectroscopy 2*, pages 83–147. Springer Berlin Heidelberg, Berlin, Heidelberg, 2015.

[74] A. Castrillo, E. De Tommasi, L. Gianfrani, et al. Doppler-free saturated-absorption spectroscopy of CO_2 at \SI{4.3}{\micro\metre} by means of a distributed feedback quantum cascade laser. *Optics Letters*, 31(20):3040, October 2006.

[75] K. Shimoda. Line broadening and narrowing effects. In S. Amelinkcx, A. Benninghoven, V. P. Chebotayev, et al., editors, *High-Resolution Laser Spectroscopy*, volume 13, pages 11–49. Springer Berlin Heidelberg, Berlin, Heidelberg, 1976. Series Title: Topics in Applied Physics.

[76] Wolfgang Demtröder. Widths and Profiles of Spectral Lines. In Vitalii I. Goldanskii, Robert Gomer, Fritz Peter Schäfer, and J. Peter Toennies, editors, *Laser Spectroscopy*, volume 5, pages 78–114. Springer Berlin Heidelberg, Berlin, Heidelberg, 1st edition, 1981. Series Title: Springer Series in Chemical Physics.

[77] Wolfgang Demtröder. *Laser Spectroscopy*. Springer Berlin Heidelberg, Berlin, Heidelberg, 2008.

[78] D. Miller. Device Requirements for Optical Interconnects to Silicon Chips. *Proceedings of the IEEE*, 97(7):1166–1185, July 2009.

[79] Katrien De Vos, Irene Bartolozzi, Etienne Schacht, et al. Silicon-on-Insulator microring resonator for sensitive and label-free biosensing. *Optics Express*, 15(12):7610–7615, June 2007.

[80] Mark Scullion, Thomas Krauss, and Andrea Di Falco. Slotted Photonic Crystal Sensors. *Sensors*, 13(3):3675–3710, March 2013.

[81] Jana Jágerská, Hua Zhang, Zhaolu Diao, et al. Refractive index sensing with an air-slot photonic crystal nanocavity. *Optics Letters*, 35(15):2523, August 2010.

[82] Wei-Cheng Lai, Swapnajit Chakravarty, Xiaolong Wang, et al. On-chip methane sensing by near-IR absorption signatures in a photonic crystal slot waveguide. *Optics Letters*, 36(6):984, March 2011.

[83] Kenji Kawano and Tsutomu Kitoh. *Introduction to Optical Waveguide Analysis*. John Wiley & Sons, Inc., New York, USA, July 2001.

[84] Steven A. Miller, Mengjie Yu, Xingchen Ji, et al. Low-loss silicon platform for broadband mid-infrared photonics. *Optica*, 4(7):707, July 2017.

[85] Tong Chen, Hansuek Lee, Jiang Li, and Kerry J. Vahala. A general design algorithm for low optical loss adiabatic connections in waveguides. *Optics Express*, 20(20):22819, September 2012.

[86] Raphael Linus Levien. *From Spiral to Spline: Optimal Techniques in Interactive Curve Design*. PhD thesis, EECS Department, University of California, Berkeley, December 2009.

[87] Marc J. Madou. *Fundamentals of microfabrication and nanotechnology: Manufacturing Techniques for Microfabrication and Nanotechnology*, volume 2. CRC Press, Boca Raton, FL, 3rd ed edition, 2012. OCLC: ocn727047810.

[88] Ananth Z. Subramanian, G. Senthil Murugan, Michalis N. Zervas, and James S. Wilkinson. High index contrast Er:Ta2O5 waveguide amplifier on oxidised silicon. *Optics Communications*, 285(2):124–127, January 2012.

[89] Ananth Z. Subramanian, G. Senthil Murugan, Michalis N. Zervas, and James S. Wilkinson. Spectroscopy, Modeling, and Performance of Erbium-Doped Ta2O5 Waveguide Amplifiers. *Journal of Lightwave Technology*, 30(10):1455–1462, May 2012.

[90] R Smith, MA Tagg, and JM Walls. Deterministic models of ion erosion, reflection and redeposition. *Vacuum*, 34(1):175–180, January 1984.

[91] K. P. Müller and J. Pelka. Redeposition in ion milling. *Microelectronic Engineering*, 7(1):91–101, January 1987.

[92] K. R. Williams, K. Gupta, and M. Wasilik. Etch rates for micromachining processing-Part II. *Journal of Microelectromechanical Systems*, 12(6):761–778, December 2003.

[93] S. M. Sze, editor. *VLSI technology*. McGraw-Hill series in electrical engineering. McGraw-Hill, New York, 2nd ed edition, 1988.

[94] Marc J. Madou. *Fundamentals of microfabrication and nanotechnology: Solid-State Physics, Fluidics, and Analytical Techniques in Micro- and Nanotechnology*, volume 1. CRC Press, Boca Raton, FL, 3rd ed edition, 2012. OCLC: ocn727047810.

[95] Tiening Jin, Junchao Zhou, and Pao Tai Lin. Mid-Infrared Electro-Optical Modulation Using Monolithically Integrated Titanium Dioxide on Lithium Niobate Optical Waveguides. *Scientific Reports*, 9(1), December 2019.

[96] Lan Li, Ping Zhang, Wei-Ming Wang, et al. Foldable and Cytocompatible Sol-gel TiO2 Photonics. *Scientific Reports*, 5(1), November 2015.

[97] C. C. Evans, K. Shtyrkova, J. D. B. Bradley, et al. Spectral broadening of femtosecond pulses in polycrystalline anatase titanium dioxide waveguides. In *Advanced Photonics Congress*, page JW4D.4, Colorado Springs, Colorado, 2012. OSA.

[98] Markus Hayrinen, Matthieu Roussey, Vishal Gandhi, et al. Low-Loss Titanium Dioxide Strip Waveguides Fabricated by Atomic Layer Deposition. *Journal of Lightwave Technology*, 32(2):208–212, January 2014.

[99] Markus Häyrinen, Matthieu Roussey, Antti Säynätjoki, et al. Titanium dioxide slot waveguides for visible wavelengths. *Applied Optics*, 54(10):2653, April 2015.

[100] Sebastián Alberti and Jana Jágerská. Sol-Gel Thin Film Processing for Integrated Waveguide Sensors. *Frontiers in Materials*, 8:629822, March 2021.

[101] I. Hotovy, S. Hascik, M. Gregor, et al. Dry etching characteristics of TiO2 thin films using inductively coupled plasma for gas sensing. *Vacuum*, 107:20–22, September 2014.

[102] S. Norasetthekul, P.Y. Park, K.H. Baik, et al. Dry etch chemistries for TiO2 thin films. *Applied Surface Science*, 185(1-2):27–33, December 2001.

[103] H. F. Winters and J. W. Coburn. The etching of silicon with XeF2 vapor. *Applied Physics Letters*, 34(1):70–73, January 1979.

[104] Dale E. Ibbotson, Daniel L. Flamm, John A. Mucha, and Vincent M. Donnelly. Comparison of XeF2 and F-atom reactions with Si and SiO2. *Applied Physics Letters*, 44(12):1129–1131, June 1984.

[105] D. E. Ibbotson, J. A. Mucha, D. L. Flamm, and J. M. Cook. Plasmaless dry etching of silicon with fluorine-containing compounds. *Journal of Applied Physics*, 56(10):2939–2942, November 1984.

[106] J.-F. Veyan, M. D. Halls, S. Rangan, et al. XeF2-induced removal of SiO2 near Si surfaces at 300 K: An unexpected proximity effect. *Journal of Applied Physics*, 108(11):114914, December 2010.

[107] Kristian P. Larsen, Dirch Hjorth Petersen, and Ole Hansen. Study of the Roughness in a Photoresist Masked, Isotropic, SF[sub 6]-Based ICP Silicon Etch. *Journal of The Electrochemical Society*, 153(12):G1051, 2006.

[108] Parashara Panduranga, Aly Abdou, Zhong Ren, et al. Isotropic silicon etch characteristics in a purely inductively coupled SF6 plasma. *Journal of Vacuum Science & Technology B*, 37(6):061206, November 2019.

[109] John W Zeller, Harry Efstathiadis, Gourav Bhowmik, et al. Development of Ge PIN Photodetectors on 300 mm Si wafers for Near-infrared Sensing. page 13.

[110] T. D. Visser, B. Demeulenaere, J. Haes, et al. Confinement and modal gain in dielectric waveguides. *Journal of Lightwave Technology*, 14(5):885–887, May 1996.

[111] H. Kogelnik. Theory of Optical Waveguides. In David H. Auston, Walter Engl, Takuo Sugano, et al., editors, *Guided-Wave Optoelectronics*, volume 26, pages 7–88. Springer Berlin Heidelberg, Berlin, Heidelberg, 1988.

[112] Shinyoung Lee, Seok Chan Eom, Jee Soo Chang, et al. Label-free optical biosensing using a horizontal air-slot SiN_x microdisk resonator. *Optics Express*, 18(20):20638, September 2010.

[113] T. Claes, J.G. Molera, K. De Vos, et al. Label-Free Biosensing With a Slot-Waveguide-Based Ring Resonator in Silicon on Insulator. *IEEE Photonics Journal*, 1(3):197–204, September 2009.

[114] Yi Zou, Harish Subbaraman, Swapnajit Chakravarty, et al. Grating-coupled silicon-on-sapphire integrated slot waveguides operating at mid-infrared wavelengths. *Optics Letters*, 39(10):3070, May 2014.

[115] Mingquan Pi, Chuantao Zheng, Ran Bi, et al. Design of a mid-infrared suspended chalcogenide/silica-on-silicon slot-waveguide spectroscopic gas sensor with enhanced light-gas interaction effect. *Sensors and Actuators B: Chemical*, 297:126732, October 2019.

[116] Jong-Moo Lee, Duk-Jun Kim, Gwan-Ha Kim, et al. Controlling temperature dependence of silicon waveguide using slot structure. *Optics Express*, 16(3):1645, 2008.

[117] Wen Zhou, Zhenzhou Cheng, Xinru Wu, et al. Fully suspended slot waveguides for high refractive index sensitivity. *Optics Letters*, 42(7):1245–1248, April 2017.

[118] Firehun Tsige Dullo, Susan Lindecrantz, Jana Jágerská, et al. Sensitive on-chip methane detection with a cryptophane-A cladded Mach-Zehnder interferometer. *Optics Express*, 23(24):31564, November 2015.

[119] Rei Kitamura, Laurent Pilon, and Miroslaw Jonasz. Optical constants of silica glass from extreme ultraviolet to far infrared at near room temperature. *Applied Optics*, 46(33):8118, November 2007.

7

Publications

Paper I

Extraordinary Evanescent Field Confinement Waveguide Sensor for Mid-Infrared Trace Gas Spectroscopy

M. Vlk, A. Datta, S. Alberti, H. D. Yallew, V. Mittal, G. S. Murugan, and J. Jágerská

Light: Science & Applications, Vol. 10(1), p. 26, 2021

Vlk et al. *Light: Science & Applications* (2021)10:26
https://doi.org/10.1038/s41377-021-00470-4

Official journal of the CIOMP 2047-7538
www.nature.com/lsa

LETTER Open Access

Extraordinary evanescent field confinement waveguide sensor for mid-infrared trace gas spectroscopy

Marek Vlk[1], Anurup Datta[1], Sebastián Alberti[1], Henock Demessie Yallew[1], Vinita Mittal[2], Ganapathy Senthil Murugan[2] and Jana Jágerská[1]

Abstract
Nanophotonic waveguides are at the core of a great variety of optical sensors. These structures confine light along defined paths on photonic chips and provide light–matter interaction via an evanescent field. However, waveguides still lag behind free-space optics for sensitivity-critical applications such as trace gas detection. Short optical pathlengths, low interaction strengths, and spurious etalon fringes in spectral transmission are among the main reasons why on-chip gas sensing is still in its infancy. In this work, we report on a mid-infrared integrated waveguide sensor that successfully addresses these drawbacks. This sensor operates with a 107% evanescent field confinement factor in air, which not only matches but also outperforms free-space beams in terms of the per-length optical interaction. Furthermore, negligible facet reflections result in a flat spectral background and record-low absorbance noise that can finally compete with free-space spectroscopy. The sensor performance was validated at 2.566 μm, which showed a 7 ppm detection limit for acetylene with only a 2 cm long waveguide.

Optical sensors based on infrared tuneable diode laser absorption spectroscopy (TDLAS)[1–4] are traditionally used for the most demanding applications in trace gas detection, from atmospheric monitoring of climate gases to detecting traces of methane on Mars by NASA's Curiosity Mars Rover[5]. These sensors rely on strong light absorption at the rotational–vibrational resonance frequencies of gas molecules and long optical interaction pathlengths, leading to detection limits below part-per-trillion (ppt) concentration levels[2]. Although a large variety of system configurations have been demonstrated, the most sensitive systems employ optical multi-pass cells or cavities[2,3] where the free-space beam is folded into tens of metres to kilometres to increase the probability of absorption by sparse target molecules. However, the large dimensions and sample volumes of multi-pass cells and their incompatibility with large-scale and cost-effective sensor deployment motivate efforts to seek alternatives using integrated photonics[6–11]. Such TDLAS sensors will allow the implementation of long optical pathlengths on chips, thus radically decreasing the instrument size and price, minimizing the sample volume, and relaxing gas flow and temperature control constraints. However, current photonic waveguides still suffer from propagation losses that limit the pathlength to several tens of centimetres. The losses mainly originate from roughness-induced scattering in the near-infrared (NIR) region and from material absorption due to residual impurities, water, OH, or NH[12,13] in the mid-infrared (MIR) region. Furthermore, reflections at waveguide facets and defects result in distinct etalon patterns in the transmission spectra. This spectral noise interferes with the signal and drastically reduces the gas detection capability and sensor stability[3,8,14]. Finally, yet importantly, the evanescent field

---

Correspondence: Ganapathy Senthil Murugan (smg@orc.soton.ac.uk) or Jana Jágerská (jana.jagerska@uit.no)
[1]Department of Physics and Technology, UiT The Arctic University of Norway, NO-9037 Tromsø, Norway
[2]Optoelectronics Research Centre, University of Southampton, Southampton SO17 1BJ, UK

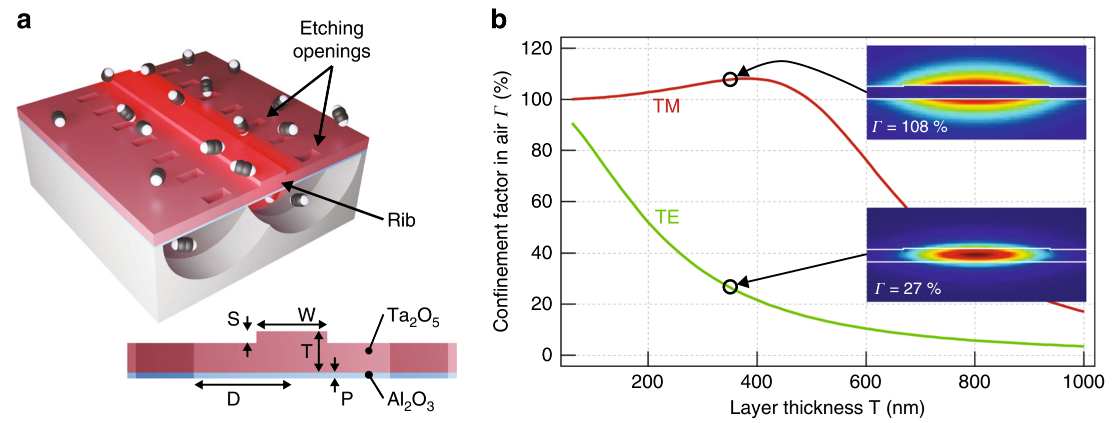

Fig. 1 Waveguide design with simulated evanescent field confinement factor in air. a Schematics of the free-standing shallow rib waveguide interacting with C_2H_2 molecules. The waveguide is patterned in a Ta_2O_5 core layer, bottom-passivated by Al_2O_3. The membrane is underetched through the etching openings. Dimensions T = 350 nm, S = 30 nm, W = 4.5 µm, D = 25 µm, and P = 30 nm guarantee single-mode propagation at λ = 2.566 µm and negligible mode disturbance by the openings. **b** Simulated confinement factor in air versus Ta_2O_5 film thickness T. Insets show $|\mathbf{E}|^2$ of the fundamental transversally magnetic (TM) and transversally electric (TE) mode field distributions together with air confinement factors for the processed membrane thickness T = 350 nm

in conventional air-cladded waveguides limits the light–matter interaction to a fraction of that for free space. Integrated waveguides must therefore be proportionally longer than the distance travelled by a free-space beam to achieve the same sensitivity.

Light absorption in waveguides exposed to an absorbing environment can be expressed by a generalized Lambert–Beer law $I = I_0 \exp[-\alpha \Gamma L]$, where Γ represents the external evanescent field confinement factor, α is the absorption coefficient of the surrounding environment, and L is the physical waveguide length. The confinement factor Γ gives a measure of light–matter interaction via the evanescent field[11,15–18], and it can be expressed as[18]

$$\Gamma = \frac{n_g}{\mathrm{Re}\{n_{cl}\}} \frac{\int\int_{cl} \varepsilon |\mathbf{E}|^2 dxdy}{\int\int_{-\infty}^{\infty} \varepsilon |\mathbf{E}|^2 dxdy} \quad (1)$$

where n_g is the group index, n_{cl} is the cladding refractive index, $\varepsilon(x, y)$ is the permittivity, and $\mathbf{E}(x, y)$ is the electric field (Supplementary Information S1). Importantly, the absorption in integrated waveguides is not simply scaled by the modal power fraction residing in the cladding but depends on both the electric field distribution and the waveguide dispersion captured through n_g. The combined effect of field delocalization and dispersion can cause Γ to exceed unity[16,17], facilitating stronger absorption than with a free-space beam.

To date, arguably the most successful realization of an on-chip TDLAS gas sensor has been based on a 10 cm long silicon strip waveguide for methane detection, operating at 1651 nm with $\Gamma = 25.5\%$[8,14]. In this work, a sub-100 ppm limit of detection (LOD) was achieved, mainly limited by etalon fringes and the weak absorption of methane in the NIR. In the MIR, three different waveguide sensors were reported to measure CO_2 concentrations down to 500 ppm, namely, silicon-on-insulator waveguides with $\Gamma = 14\%$[9], silicon strip waveguides on Si_3N_4 membranes with $\Gamma = 19.5\%$[10], and free-standing silicon strip waveguides supported by isolated pillars with $\Gamma = 44\%$[11]. Even higher confinement factors have been claimed using slow light photonic-crystal waveguides[6,7,19]; however, these came at the expense of high propagation loss limiting the device length to at best 1.5 mm[7].

In this work, we propose a waveguide sensor that pushes the confinement factor above 100% by making use of strong guided mode delocalization rather than waveguide dispersion. Our design is based on a free-standing high-aspect-ratio tantalum pentoxide (Ta_2O_5) membrane, where lateral confinement is achieved by a shallow rib, as illustrated in Fig. 1a. In the direction perpendicular to the membrane surface, the field distribution is mainly governed by the membrane thickness. Specifically, for transversally magnetic (TM) polarization, the evanescent field fraction increases rapidly with decreasing membrane thickness, and already at T = 500 nm, the weak waveguide dispersion is sufficient to bring the external confinement factor Γ above 100% (Fig. 1b and Supplementary S2.1). For Ta_2O_5 with a moderate refractive index, Γ reaches a maximum of 108% at approximately T = 400 nm, implying that a strong per-length interaction can be reached with a relatively thick and mechanically stable membrane.

To avoid interaction between the evanescent field and substrate in real structures, it is critical to remove the bottom cladding and create a sufficiently large separation between the membrane and the substrate. Oxide films on

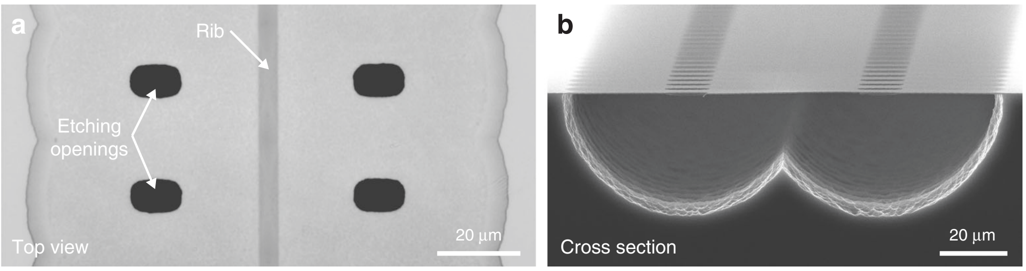

Fig. 2 Suspended rib waveguide. a Top-view optical microscope image of the fabricated waveguide. **b** SEM image of the waveguide cross section. The fabrication process resulted in a 130 μm wide and 350 nm thick membrane

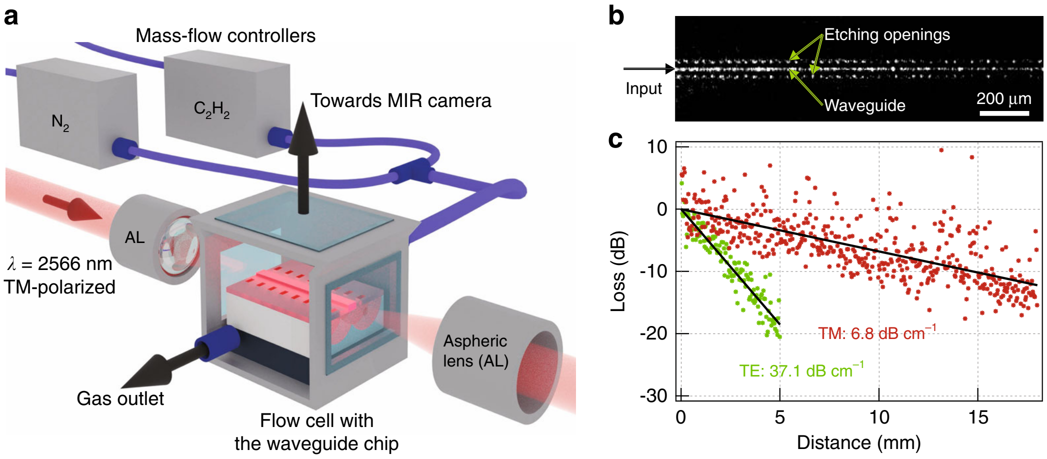

Fig. 3 Characterization setup and propagation loss measurement. a Outline of the experimental setup. **b** Top-view MIR image of the waveguide at 2.566 μm. The guided mode is visible through out-of-plane scattering at waveguide roughness and imperfections. **c** Propagation loss determined from the decay of out-of-plane scattered light for both TM and TE polarizations. The TE mode that is well confined in the Ta_2O_5 membrane experiences higher loss due to material absorption than the strongly delocalized TM mode

Si are widely used in microelectromechanical systems (MEMS)[20–23], and this concept was adopted here, as it allows for deeply underetched, high-aspect-ratio membranes. Ta_2O_5 was selected as the core material for its availability in microfabrication process lines, chemical and mechanical stability[24,25], low thermal expansion[26], low thermooptic coefficient[27], and optical transparency spanning from 500 nm to 10 μm[28,29]. A 350 nm Ta_2O_5 film was first deposited onto a silicon wafer passivated with a thin layer of aluminium oxide (Al_2O_3) to protect Ta_2O_5 against undesirable etching. Following a 2-step lithography process to pattern the ribs and etching openings, the membrane was underetched using xenon fluoride (XeF_2) dry etching. This process resulted in a 130 μm wide membrane with more than 20 μm separation from the Si wafer below, as captured in Fig. 2.

The waveguides were characterized in an end-fire coupling configuration using the combined imaging and spectroscopy setup depicted in Fig. 3a. A waveguide propagation loss of 6.8 dB cm^{-1} was measured for the TM polarization (Fig. 3b, c), comparable to values reported with other MIR waveguide gas sensors[9,11]. The loss is mainly attributed to light absorption in the Ta_2O_5 film due to residual OH and water (Supplementary S5) and is expected to drop significantly with an optimized film deposition process.

For an external confinement factor measurement and a spectroscopy evaluation, acetylene (C_2H_2), with its strong Q-band absorption peak near 2.566 μm (3897.1 cm^{-1}), was selected as an analyte. Figure 4a compares the experimental transmission spectra measured for a number of C_2H_2 concentrations using a 2 cm long waveguide in the TM polarization and a free-space beam of the same pathlength. The experimental spectra were fitted with reference spectra from the Pacific Northwest National Laboratory (PNNL) database[30] to precisely quantify the amplitude of the absorption peak. As illustrated in Fig. 4b, c, the absorption data acquired over 500 s for different reference gas concentrations between 1% and 10% exhibit good long-term stability and linearity without the need for intermittent recalibration. The fitted concentrations in free space closely match the reference value, but those

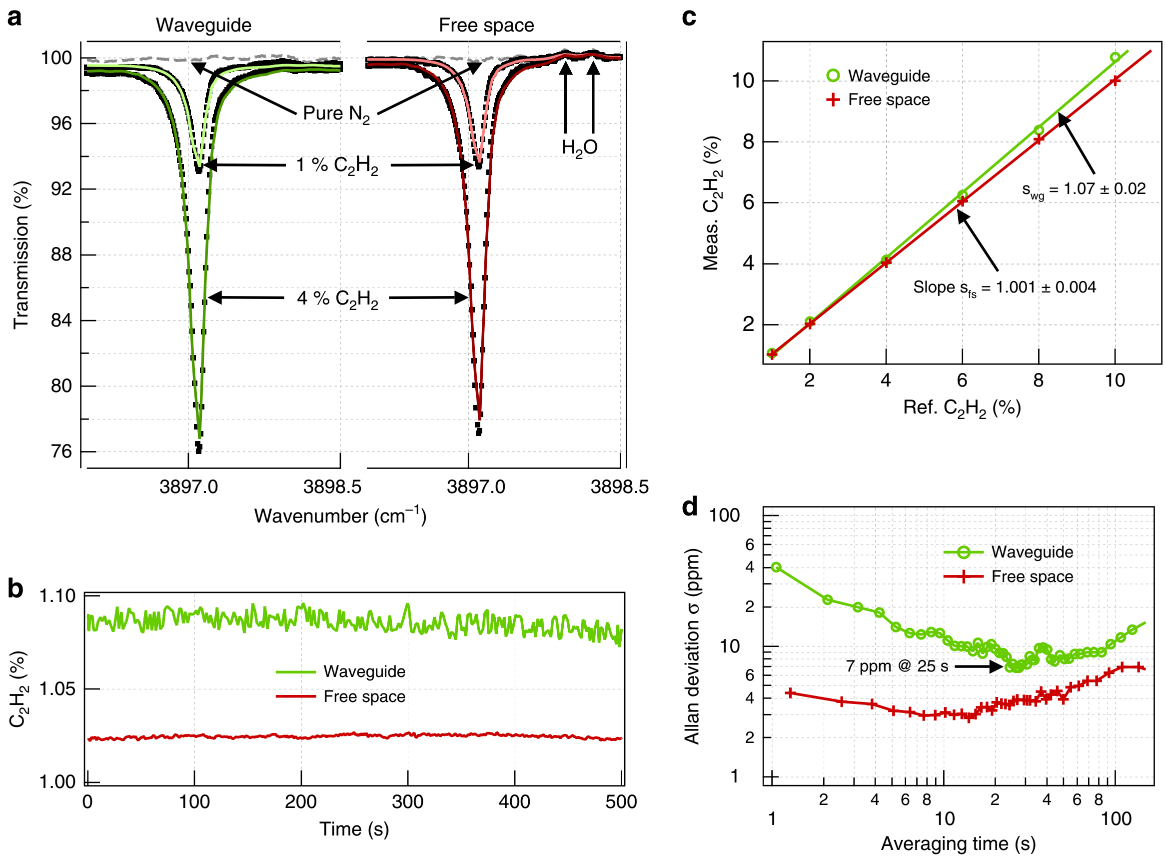

Fig. 4 Spectroscopic measurements with acetylene. a Transmission spectra (square symbols) and PNNL fits (solid lines) at different concentrations of C_2H_2 in N_2 measured with a 2 cm long waveguide (left) and in free space of equal pathlength (right). The spectra are normalized to the transmittance with dry N_2 (gray dashed lines). **b** Concentration time series for 1% C_2H_2 obtained from real-time spectral fitting with PNNL free-space reference spectra. **c** Measured C_2H_2 concentrations versus reference. The ratio s_{wg}/s_{fs} yields the evanescent field confinement factor in air as Γ = 107 ± 2% free from systematic error that may occur due to uncertainty in the calibration gas concentration or dilution. **d** Allan deviation plot corresponding to the concentration data time series shown in **b**. LOD of 7 ppm after 25 s averaging achieved with the waveguide translates into the absorption noise of 4.5×10^{-5}

measured with the waveguide are visibly higher, as they are scaled up by the extraordinary confinement factor. The exact value of Γ was retrieved from the ratio of the respective slopes in Fig. 4c, yielding 107 ± 2% in excellent agreement with the simulation.

The LOD was evaluated using Allan deviation analysis[4] with a 1% nominal C_2H_2 concentration measured for over 20 min (Fig. 4d). The 1σ-LOD was 7 ppm and 3 ppm using the waveguide and in free space, respectively, with the waveguide data visibly influenced by short-term coupling noise. Hence, despite comparably stronger light–matter interaction in the waveguide, the sensitivity of the free space has not yet been surpassed. However, we stress that this result was achieved with bulk coupling optics, with no thermal stabilization, and without any fringe removal or spectral filtering algorithms, and it is likely to be improved by more elaborate signal processing methods[14]. Nevertheless, the mere 2.5-fold difference in the LOD and comparable system stability almost close the performance gap between the on-chip and free-space-based MIR TDLAS analyzers.

This achievement is largely due to strong field delocalization, which enhances the sensitivity and minimizes the reflections at waveguide facets and defects. Due to a remarkably low effective index of the guided mode ($n_{eff} \cong 1.08$), reflections at the waveguide facets are ~0.1% (Supplementary S4 and Fig. S6), which is two orders of magnitude less than those for standard SOI waveguides. Similar low reflections are expected at other fabrication imperfections and material defects. As a result, Fabry–Pérot etalons, which substantially limit the performance of other reported waveguide sensors[3,7,14], are almost entirely suppressed. Strong evanescent field confinement also implies a low interaction of the mode with the waveguide material (Supplementary S5), which relaxes the requirements on material transparency and allows realization of long waveguides in fairly lossy materials. This property is particularly relevant in the MIR, where the optimization of photonic material is still an active research topic[31,32]. Last but not least, strong field delocalization resulting in a fairly large mode area mitigates absorption saturation effects[33] that can take place under intense irradiation typical for integrated nanophotonic waveguides. As calculated in Supplementary S6, our waveguide can be safely operated with input powers up to 100 mW at 1 bar before the 2.566 μm acetylene absorption line begins to saturate.

In conclusion, we have demonstrated a novel air-suspended Ta_2O_5 rib waveguide with a strongly delocalized field, leveraging the unique features of free-space beams for on-chip spectroscopy. Consequently, an absorption noise of 4.5×10^{-5} retrieved from the measured LOD was demonstrated[1]. This is, to our knowledge, the lowest value reported for a TDLAS platform based on integrated optical waveguides, either in the NIR or MIR. The current waveguide design curled in a spiral can easily reach 20 cm on a 1 cm^2 footprint, pushing the LODs for most gases to below part-per-million concentration levels while maintaining a minimal size of the sensor and microlitre sample volumes. Although on-chip sensors may not beat the kilometre pathlengths and ppt detection limits of high-end free-space TDLAS systems, radical sensor miniaturization will facilitate sensor deployment in process control, climate and space research and may open a whole class of new applications that are still out of reach for laser absorption spectroscopy. Examples include sensor organization in networks or in situ monitoring of metabolic processes in microbiology or organoid research. In the latter case, unprecedently small sample volumes combined with high sensitivity and specificity, inherent to TDLAS detection methods, will, for the first time, allow the quantification of metabolic gas release in situ and, so to speak, at a cellular level. Moreover, parallel waveguides patterned on the same chip, each optimized for a different analyte species, can readily realize a multi-gas sensor, with only a negligible increase in its footprint and complexity.

Methods

Waveguide simulations

All simulations were performed with the finite differences eigenmode solver Lumerical, MODE. Perfectly matched layers (PMLs) were used on the bottom and both sides of the computational domain to assess the mode leakage into the substrate and the lateral leakage of the TM mode. The effect of the etching openings on the guided mode was studied by varying the width of the computational domain. Single-mode conditions, complex effective indices, mode distributions, and coupling losses were simulated using built-in functions of the software. The confinement factor was calculated using a custom script integrated in the software. More details on the waveguide loss simulation and confinement factor calculation are provided in Supplementary Information S1 and S2.

Waveguide fabrication

Thin films of SiO_2 (30 nm), Al_2O_3 (30 nm), and Ta_2O_5 (350 nm) were deposited in this order onto 4-inch Si wafers by magnetron RF sputtering (Oxford Instruments PlasmaLab 400 +). SiO_2 promotes the adhesion of Al_2O_3 on Si, and Al_2O_3 acts as a passivation layer to protect Ta_2O_5 during membrane underetching. The deposited films were annealed in a tube furnace at 600 °C in O_2 for 3 h (1 °C/min ramping) to improve stoichiometry, and reduce the content of residual water and OH in the film.

Waveguides and etching openings were patterned via UV photolithography in two separate steps. For the waveguides, we applied a positive photoresist and exposed the waveguide patterns from a chromium hard mask in a mask aligner (Süss MA-6, $\lambda = 385$ nm). Pattern transfer from the resist to the Ta_2O_5 layer was performed via Ar ion beam milling (Oxford Instruments Ionfab 300 +). The same procedure was followed for making the etching openings (nominal dimensions 5×10 μm^2, Fig. 2a) with another Cr hard mask aligned to the waveguide pattern. It is critical to expose Si in the etching openings by Ar milling before the next step. Underetching, i.e., the selective removal of Si was performed by dry etching using XeF_2 (Xactix) in pulsed mode with 270 cycles of alternating XeF_2/N_2 etching (3/2 Torr, 5 s) and N_2 purging (10 s) steps. Ta_2O_5 was protected during the release process by photoresist on the top surface and Al_2O_3 layer on the bottom surface, which are both substantially more resistant to XeF_2 than Ta_2O_5.

Waveguide propagation losses

The propagation loss measurement was performed in the combined imaging and spectroscopy setup shown in Fig. 3a. An electrically tuneable DFB diode laser (Nanoplus) emitting a maximum of 15 mW at 2.566 μm was used as the light source. The laser polarization was set to either TE or TM using a half-wave plate and a polarizer. The laser beam was end-fire-coupled into the waveguides using an MIR aspheric lens (Thorlabs, black diamond, NA = 0.56). An MIR camera (Telops) was used to image the sample surface and aid the in-coupling. The propagation loss was measured from the decay of light scattered out of plane from the waveguide and recorded with the MIR camera (Fig. 3a). The raw image data taken along the waveguide length were first corrected for background due to thermal noise and spurious laser light, stitched together, and finally averaged over 10 adjacent pixels to give data presented in Fig. 3a (see also Supplementary S5.1 for further details about the data post-processing). Robustness of the loss value obtained by this method was also cross-checked by the cutback method on three different waveguides from the same wafer that yielded the loss of $6.8 \pm 0.7\,\mathrm{dB\,cm^{-1}}$.

Spectroscopic measurements

The 2 cm long waveguide chip was enclosed in a 2.4 cm long custom gas flow cell with glass windows (Fig. 3a) to provide a controlled environment in terms of the gas concentration and pressure. The latter was kept at 1 bar throughout the experiment. The light transmitted through the waveguide was collected and focused on a single-pixel MCT photodetector (Vigo PVI-3TE-3.4). A custom LabVIEW program was used to electrically tune the laser emission wavelength by 2–3 nm around the target absorption line and to control synchronous data acquisition with a high-speed field-programmable gate array (FPGA) digitizer. Spectral data were acquired at a rate of 1 kHz and averaged in real time to provide 1 s spectra for further data processing. Each spectrum was first divided by a reference measurement with 100% N_2 to obtain a flat baseline. Water was included in the fit (Fig. 4a) by modelling the spectrum as a sum of H_2O and C_2H_2 spectral templates because weak interference with atmospheric water from outside the gas cell was observed. The normalized spectra were then fitted with calibrated C_2H_2 spectra from the PNNL database to obtain the so-called equivalent concentration C_{eq}, accounting for the total 2.4 cm length of the cell. C_{eq} was subsequently corrected for the 0.4 cm free-space contribution between the waveguide facets and the flow cell windows by solving the equation $C_{\mathrm{eq}} \times 2.4 = C \times 2 + C_{\mathrm{ref}} \times 0.4$, where C and C_{ref} are the waveguide-measured and the reference concentrations, respectively. A linear regression fit of C versus C_{ref}, as shown in Fig. 4c, was used to calculate the slope of the line, which represents the average relation between the measured and reference concentration values. For the free-space measurement, the same procedure was repeated with the gas cell without the waveguide chip and collimation optics.

Acknowledgements
This work was supported by the European Research Council (grant no. 758973), the Research Council of Norway (grant no. 262608), Tromsø Research Foundation (project ID 17_SG_JJ), the Norwegian PhD Network on Nanotechnology for Microsystems (contract no. 221860/F60), EPSRC SPFS Programme grant (EP/L00044X/1), and "The Future Photonics Hub" (EPSRC grant EP/N00762X/1). The authors also want to thank Jan Torgersen for valuable discussions on waveguide fabrication, Herbert Looser for sharing his code for spectral data processing, and Olav G. Hellesø, Balpreet S. Ahluwalia, Peter Geiser, and James S. Wilkinson for a careful review of the manuscript.

Author contributions

J.J. conceived the idea and together with G.S.M. designed the research. M.V. simulated and fabricated the waveguide sensor and performed loss characterization. V.M. conducted the membrane underetching. A.D., H.D.Y., and S.A. constructed the setup, and A.D. performed all spectroscopic measurements. J.J. supervised the work, while G.S.M. led the fabrication. M.V. and J.J. mainly wrote the paper. All authors reviewed the manuscript and provided editorial input.

Conflict of interest

The authors declare that they have no conflict of interest.

Supplementary information The online version contains supplementary material available at https://doi.org/10.1038/s41377-021-00470-4.

Received: 19 May 2020 Revised: 6 January 2021 Accepted: 12 January 2021

References

1. McManus, J. B. et al. Application of quantum cascade lasers to high-precision atmospheric trace gas measurements. *Optical Eng.* **49**, 111124 (2010).
2. Tuzson, B. et al. Selective measurements of NO, NO_2 and NO_y in the free troposphere using quantum cascade laser spectroscopy. *Atmos. Meas. Tech.* **6**, 927–936 (2013).
3. Hodgkinson, J. & Tatam, R. P. Optical gas sensing: a review. *Meas. Sci. Technol.* **24**, 012004 (2013).
4. Werle, P., Mücke, R. & Slemr, F. The limits of signal averaging in atmospheric trace-gas monitoring by tunable diode-laser absorption spectroscopy (TDLAS). *Appl. Phys. B.* **57**, 131–139 (1993).
5. Mahaffy, P. R. et al. The sample analysis at mars investigation and instrument suite. *Space Sci. Rev.* **170**, 401–478 (2012).
6. Lai, W. C. et al. On-chip methane sensing by near-IR absorption signatures in a photonic crystal slot waveguide. *Opt. Lett.* **36**, 984–986 (2011).
7. Dicaire, I. et al. Probing molecular absorption under slow-light propagation using a photonic crystal waveguide. *Opt. Lett.* **37**, 4934–4936 (2012).
8. Tombez, L. et al. Methane absorption spectroscopy on a silicon photonic chip. *Optica* **4**, 1322–1325 (2017).
9. Ranacher, C. et al. Characterization of evanescent field gas sensor structures based on silicon photonics. *IEEE Photonics J.* **10**, 2700614 (2018).
10. Ranacher, C. et al. Mid-infrared absorption gas sensing using a silicon strip waveguide. *Sens. Actuators A: Phys.* **277**, 117–123 (2018).
11. Ottonello-Briano, F. et al. Carbon dioxide absorption spectroscopy with a mid-infrared silicon photonic waveguide. *Opt. Lett.* **45**, 109–112 (2020).
12. Beshkov, G. et al. IR and Raman absorption spectroscopic studies of APCVD, LPCVD and PECVD thin SiN films. *Vacuum* **69**, 301–305 (2002).
13. Bright, T. J. et al. Infrared optical properties of amorphous and nanocrystalline Ta_2O_5 thin films. *J. Appl. Phys.* **114**, 083515 (2013).
14. Zhang, E. J. et al. Adaptive etalon suppression technique for long-term stability improvement in high index contrast waveguide-based laser absorption spectrometers. *Electron. Lett.* **55**, 851–853 (2019).
15. Visser, T. D. et al. Confinement factors and gain in optical amplifiers. *IEEE J. Quantum Electron.* **33**, 1763–1766 (1997).
16. Parriaux, O. et al. Evanescent wave sensor of sensitivity larger than a free space wave. *Opt. Quantum Electron.* **32**, 909–921 (2000).
17. Veldhuis, G. J. et al. Sensitivity enhancement in evanescent optical waveguide sensors. *J. Lightwave Technol.* **18**, 677–682 (2000).
18. Robinson, J. T. et al. First-principle derivation of gain in high-index-contrast waveguides. *Opt. Express* **16**, 16659–16669 (2008).
19. Zou, Y. et al. Experimental demonstration of propagation characteristics of mid-infrared photonic crystal waveguides in silicon-on-sapphire. *Opt. Express* **23**, 6965–6975 (2015).
20. Frederico, S. et al. Silicon sacrificial layer dry etching (SSLDE) for free-standing RF MEMS architectures. In *Proc. Sixteenth Annual International Conference on Micro Electro Mechanical Systems*. pp. 570–573 (IEEE, Kyoto, Japan, 2003).
21. Williams, K. R., Gupta, K. & Wasilik, M. Etch rates for micromachining processing-Part II. *J. Microelectromech. Syst.* **12**, 761–778 (2003).
22. Arana, L. R. et al. Isotropic etching of silicon in fluorine gas for MEMS micromachining. *J. Micromech. Microeng.* **17**, 384–392 (2007).
23. Ghaderi, M. & Wolffenbuttel, R. F. Design and fabrication of ultrathin silicon-nitride membranes for use in UV-visible airgap-based MEMS optical filters. *J. Phys.: Conf. Ser.* **757**, 012032 (2016).
24. Chaneliere, C. et al. Tantalum pentoxide (Ta_2O_5) thin films for advanced dielectric applications. *Mater. Sci. Eng.: R: Rep.* **22**, 269–322 (1998).
25. Singh, S. et al. Universal method for the fabrication of detachable ultrathin films of several transition metal oxides. *ACS Nano* **2**, 2363–2373 (2008).

26. Lee, C. C. et al. An apparatus for the measurement of internal stress and thermal expansion coefficient of metal oxide films. *Rev. Sci. Instrum.* **72**, 2128–2133 (2001).
27. Wu, C.-L. et al. Tantalum pentoxide (Ta_2O_5) based athermal micro-ring resonator. *OSA Contin.* **2**, 1198–1206 (2019).
28. Kulisch, W. et al. In *Nanostructured Materials for Advanced Technological Applications* (eds Reithmaier, J. P. et al.) (Springer, 2009).
29. Saygin-Hinczewski, D. et al. Optical and structural properties of Ta_2O_5-CeO_2 thin films. *Sol. Energy Mater. Sol. Cells* **91**, 1726–1732 (2007).
30. Sharpe, S. W. et al. Gas-phase databases for quantitative infrared spectroscopy. *Appl. Spectrosc.* **58**, 1452–1461 (2004).
31. Mittal, V. et al. Optical quality ZnSe films and low loss waveguides on Si substrates for mid-infrared applications. *Optical Mater. Express* **7**, 712–725 (2017).
32. Lin, H. T. et al. Mid-infrared integrated photonics on silicon: a perspective. *Nanophotonics* **7**, 393–420 (2017).
33. Demtröder, W. In *Laser Spectroscopy* Vol. 5, 1st edition (ed. Demtröder, W.) (Springer, 1981).

Supplementary Information: Extraordinary evanescent field confinement waveguide sensor for mid-infrared trace gas spectroscopy

Marek Vlk[1], Anurup Datta[1], Sebastián Alberti[1], Henock Demessie Yallew[1], Vinita Mittal[2], Ganapathy Senthil Murugan[2]*, Jana Jágerská[1]*

1. Department of Physics and Technology, UiT The Arctic University of Norway, NO-9037 Tromsø, Norway

2. Optoelectronics Research Centre, University of Southampton, Southampton, SO17 1BJ, UK

[1]*jana.jagerska@uit.no, [2]*smg@orc.soton.ac.uk

Contents

S1) Confinement Factor

In optical waveguides, the confinement factor Γ represents a measure of interaction of the guided mode with the waveguide core or cladding, or, more generally, any material constituting the waveguide. Gain or loss α_{m} of a waveguide mode can be obtained from confinement factors Γ_i and bulk gain/loss coefficients α_i of individual materials which constitute the waveguide as

$$\alpha_{\mathrm{m}} = \sum_i \Gamma_i \alpha_i \,. \tag{S1}$$

Light absorption or gain along the waveguide can be then expressed by the generalized Lambert–Beer law

$$I = I_0 \exp\left[-\sum_i \Gamma_i \alpha_i \, L\right] \tag{S2}$$

Particular expressions for the confinement factor have been derived from the Poynting theorem[1] or from the variation theorem for dielectric waveguides[2] and hold for both gain and lossy media such as molecular gases.[3]

Using the Poynting theorem, Visser et al.[1] have found that the confinement factor is given as

$$\Gamma_i = \frac{c\varepsilon_0 \mathrm{Re}\{n_i\} \iint_i \left|\tilde{\mathbf{E}}\right|^2 dxdy}{\mathrm{Re}\{\iint_{-\infty}^{\infty} \left(\tilde{\mathbf{E}} \times \tilde{\mathbf{H}}^*\right) \cdot \mathbf{e}_z dxdy\}}. \tag{S3}$$

with c being the vacuum velocity of light, ε_0 the permittivity of vacuum, n_i the refractive index of i^{th} material, $\mathbf{E}$ and $\mathbf{H}$ the electric and magnetic field intensity respectively, and $\mathbf{e}_z$ the normal vector in the direction of propagation, z. Robinson et al.[2] have derived (S3) from the variational theorem for dielectric waveguides.[4] In addition, they have shown that it can also be expressed as

$$\Gamma_i = \frac{n_{\mathrm{g}}}{\mathrm{Re}\{n_i\}} \frac{\iint_i \varepsilon \left|\tilde{\mathbf{E}}\right|^2 dxdy}{\iint_{-\infty}^{\infty} \varepsilon \left|\tilde{\mathbf{E}}\right|^2 dxdy}. \tag{S4}$$

with n_{g} being the group index. The first fraction is linked to the particular material and, more importantly, to the waveguide dispersion. The second fraction represents the normalized electric field energy density in the i^{th} material.

The confinement factor can be readily calculated from (S3) or (S4) for an arbitrary part of the waveguide. In this work, the material of interest was air (particularly a mixture of N_2 and C_2H_2), which constitutes both the top and the bottom cladding of the waveguide (Fig. S1a). In the main text, we therefore reserve the symbol Γ for the evanescent field confinement factor in air.

S2) Design optimization

Fig. S1 schematically portrays the free-standing rib waveguide with its dimensional parameters. When designing the waveguide, we focused on the layer thickness T, the rib width W, and

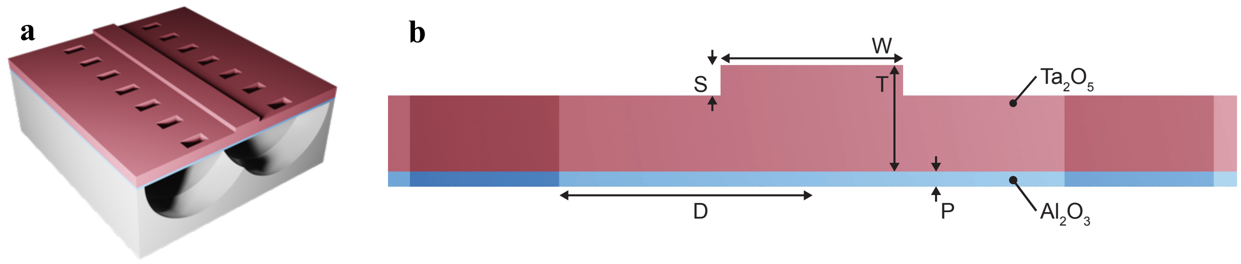

Fig. S1 | Free-standing rib waveguide schematics. a, Illustration of the waveguide which includes a shallow rib, and etching openings. **b**, The waveguide cross section. Our waveguide consists of a core Ta_2O_5 layer and a thin passivating Al_2O_3 layer, which is a necessary feature for the under-etching step in fabrication.

the rib step S for TM polarization at 2.566 μm and refractive indices 2.1 and 1.65 for Ta_2O_5 and Al_2O_3 respectively. All simulations in the design optimization were done with a finite-difference modelling software (MODE, Lumerical) prior to the fabrication. We considered three principal factors that together determined the waveguide dimensions: the evanescent field confinement factor in air Γ, the lateral leakage of the TM mode which occurs in rib waveguides,[5,6] and the single-mode condition.

S2.1) Evanescent field confinement factor in air

As shown in Fig. 1b of the main text, and also reproduced here in Fig. S2a, the evanescent field confinement factor in air depends strongly on the thickness T of the deposited layer but very weakly on the shallow rib dimensions. The change of the rib width W from 3 to 6 μm induced oscillating variations in Γ within only ± 1 % with T = 350 nm. Moreover, the additional layer of Al_2O_3, which is necessary for the fabrication, has only a small effect on the design.

According to Eq. (S4), the value of Γ results from a combination of field distribution and dispersion. Fig. S2b displays separately these two contributions, that is the electric field energy density $\varepsilon|\mathbf{E}|^2$ and the group index n_g. Multiplying these two quantities yields again the Γ plotted in Fig. S2a. In

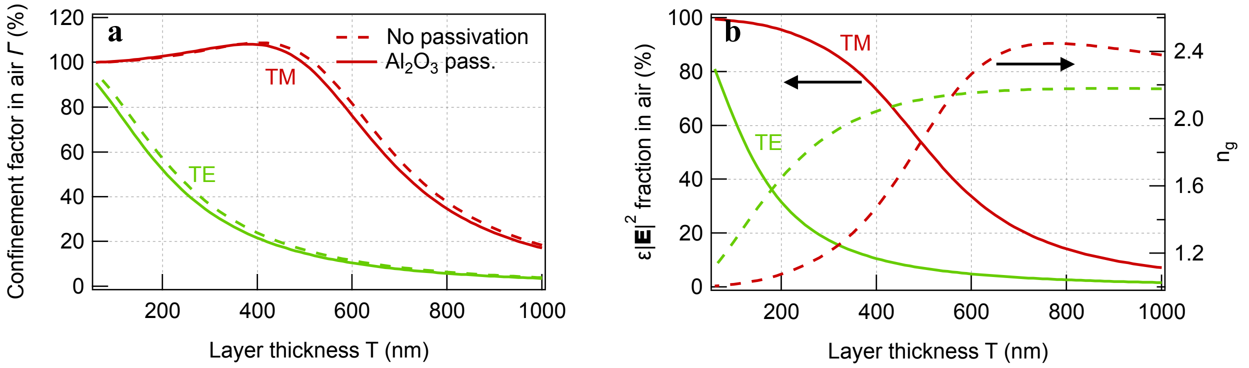

Fig. S2 | Evanescent field air-confinement factor of the free-standing rib waveguide. a, The dependence of the confinement factor on the layer thickness T for both non-passivated Ta_2O_5 membrane and membrane passivated with 30 nm of Al_2O_3. The step S and rib width W were set to 30 nm and 4.5 μm respectively. **b**, Plot of the electric field energy density fraction and the group index. Multiplying these two characteristics yields the confinement factor in air according to eq. (S4).

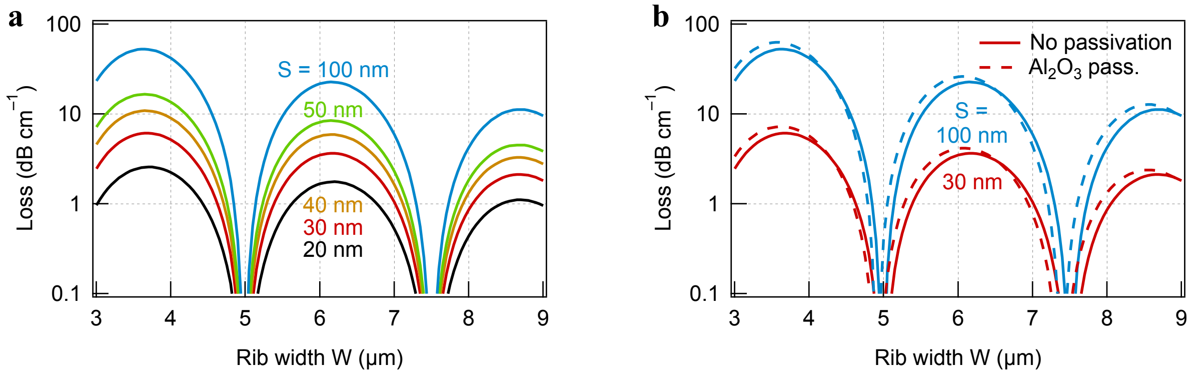

Fig. S3 | Lateral leakage of the TM mode. a, Loss dependence on the rib width for different rib steps from 20 to 100 nm. No Al_2O_3 passivation layer was assumed, and the layer thickness T was fixed to 350 nm. **b**, Deviation in the dependence caused by adding the Al_2O_3 passivation layer.

our waveguide design with T = 350 nm, the major contribution evidently comes from the strongly delocalized field rather than the dispersion, although the combination of the two is required to yield the extraordinary values of Γ. In addition, the extraordinary Γ can be obtained only in TM polarization in the rib waveguide, while for TE polarization, it monotonously increases to unity as the layer is approaching zero thickness.[7]

S2.2) Lateral leakage of TM mode in rib waveguides

The lateral leakage was explained and experimentally demonstrated by Webster et al.[5] It is characteristic only for TM-polarized rib waveguide modes and does not occur for TE-polarized modes. A rib waveguide is naturally formed in a slab which itself is a planar waveguide (see Fig. S1). In essence, the guided TM mode of a rib waveguide couples to a TE planar waveguide mode. This happens for two reasons. First, the guided TM mode has a lower effective index than the TE fundamental planar waveguide mode, which means that there will always be a phase-matched TE mode supported in the slab. Second, like all 2D waveguide modes, the TM rib waveguide mode is hybridized, and so can couple to the TE planar waveguide mode via its minor TE component. As a consequence, the energy of the TM mode is radiated out into the planar waveguide. Nevertheless, this is a resonant effect and the leakage can be avoided if the waveguide dimensions are carefully optimized.

Fig. S3a demonstrates the dependence of the lateral leakage on the rib width W for several step values S, with the layer thickness T fixed to 350 nm. There are pronounced minima in the loss around 5 and 7.5 µm within the studied range of W. We targeted the minimum around 5 µm in our design because such dimension still guarantees single-mode propagation (see the next section S2.3). Although another minimum would occur below W = 3 µm, the corresponding mode would be strongly laterally delocalized, requiring much wider membrane. This would be impractical from the point of membrane fabrication and its resulting mechanical stability.

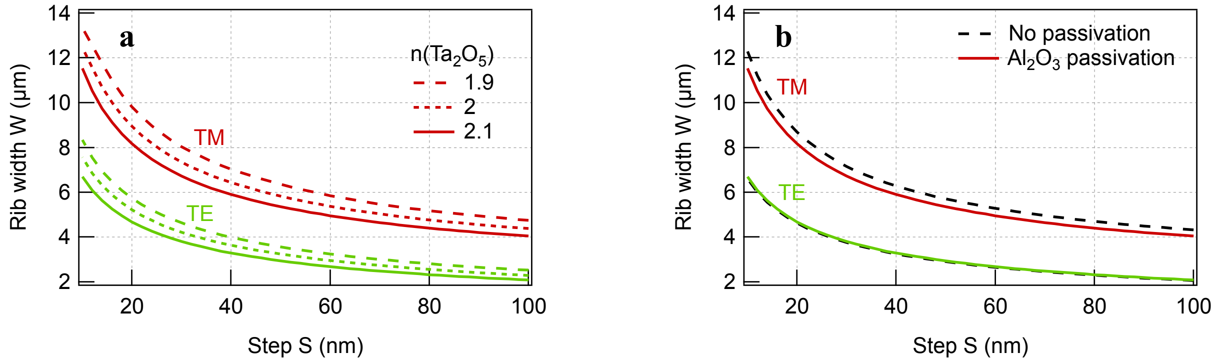

Fig. S4 | Single-mode condition. **a**, The single-mode condition was studied for several values of the refractive index of Ta_2O_5, which varies depending on the deposition method. The waveguide is single-mode below each curve for the respective polarization and refractive index of Ta_2O_5. Above the curves, the waveguide supports at least one higher order mode. **b**, Influence of the Al_2O_3 passivation layer on the single-mode condition.

Increasing the step S increases the maxima of the loss and narrows the fabrication tolerance for the rib width W. In this work, we selected S = 30 nm as a compromise between the fabrication tolerance and lateral mode confinement which needs to be sufficient in order to avoid scattering on the etching openings. Furthermore, for lithographic tuning, we set the rib width W to 4, 4.5, and 5 µm to follow the lateral leakage loss curve between one maximum and minimum (Fig. S3), and to account for inaccuracies in the fabrication.

Although we present only straight waveguides, the waveguide could be patterned into a spiral to achieve a longer pathlength on a small footprint. E.g. for a limit of a 1 cm^2 chip size, further optimization of parameters S and W would be required after selecting the thickness T.

S2.3) Single-mode condition

We studied the single-mode condition by observing the cut-off for the first-order mode in terms of parameters S and W. Simulations were performed for T = 350 nm and the results are presented in Fig. S4. Any choice of S and W from the parameter space below the plotted cut-off curve will result in single-mode propagation. Hence, step S = 30 nm and rib width W from 4 to 5 µm will yield a single-mode rib waveguide for the TM polarization with a large margin. In the TE polarization, the waveguide already just supports a higher order mode for W = 4 µm.

S3) Spectral response of the waveguide

In Fig. S5, we show how the lateral leakage loss and the confinement factor change in TM polarization with wavelength ranging from 2 to 3 µm. The waveguide maintains leakage loss below 1 dB cm^{-1} from approx. 2300 to 2500 nm, indicating a bandwidth of about 200 nm. It is evident that our current design is not fully optimized for the task of acetylene detection as the theoretical loss is around 1.5 dB cm^{-1} at 2.566 µm. As far as the confinement factor is concerned, the spectral variation within

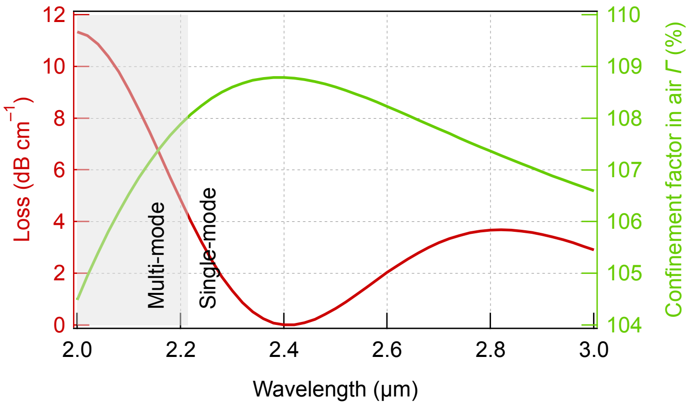

Fig. S5 | Waveguide spectral response. Wavelength dependence of the lateral leakage loss and the confinement factor in air Γ for dimensions T = 350 nm, W = 4.5 µm, S = 30 nm, P = 30 nm, and refractive indices 2.1 and 1.65 for Ta_2O_5 and Al_2O_3 respectively. The shaded area represents multi-mode behaviour.

the 200 nm bandwidth is less than 1 %. The graph also captures the single-mode condition, which occurs at 2.214 µm.

S4) Etalon effects

The TM guided mode exhibits exceptionally low effective index, $n_{\mathrm{eff}} = 1.08$. This translates into low Fresnel reflections between air and the mode at the waveguide facet. In order to quantify the reflection, we used the formula for normal incidence

$$R = \frac{|n_{\mathrm{eff}} - n|^2}{|n_{\mathrm{eff}} + n|^2} \tag{S5}$$

with $n = 1$ for air, and the n_{eff} data obtained with finite-difference mode solver (MODE, Lumerical). With the dimensions set to S = 30 nm, T = 350 nm, and W = 4.5 µm, we obtained 0.1 % reflection in TM polarization, while TE polarization gave 3.7 % (Fig. S6). Low Fresnel reflection is not only beneficial for the in-/out-coupling, but also helps to minimize etalon effects in the waveguide which otherwise limit the device performance in spectroscopic applications.

S5) Waveguide loss

This section describes the propagation loss analysis. Following the determination of the losses in both TM and TE polarization, and with the knowledge of the core confinement factor we estimated the bulk loss of the tantalum pentoxide.

S5.1) Propagation loss measurement and data post-processing

The loss evaluation was done by analysing MIR camera images of the guided light scattered out of plane. In total, 11 images were acquired for TM polarization and 5 images for TE polarization

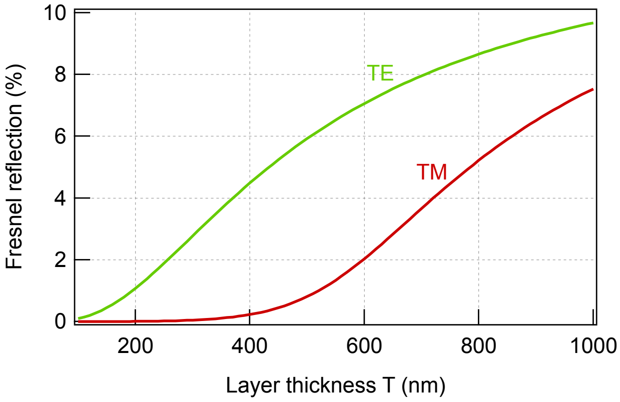

Fig. S6 | Fresnel reflections. Fresnel reflections dependence on a film thickness T for both polarizations. For the calculation, we assumed transmission between the mode of a given effective index and air, and normal incidence.

with a 2 cm long waveguide. The propagation loss in TE polarization is much higher, and there was no appreciable signal after the fifth image corresponding to approx. 1 cm of the waveguide length.

First, these images were corrected for thermal background because the MIR camera captures thermal radiation. This was done by blanking the laser, recording the thermal background, and subtracting it from the signal image. Moreover, the exposure time was individually adjusted for each image as to not saturate the camera.

Subsequently, the images were integrated across the waveguide width, corrected for different exposure times and spurious laser light background, and stitched together to give the complete intensity decay profile as presented in Fig. 3c of the main text (in this Figure, 10-point data averages are shown instead of the full dataset in order to improve the data presentation).

Finally, the intensity profile was converted into decibel (dB) power units as $S_{\mathrm{dB}} = 10\log(S/S_0)$, where S is the intensity value after integrating the camera signal and S_0 the maximum value. The decay profile S_{dB} was fitted with a linear curve, where the slope gave directly the propagation loss.

S5.2) Ta_2O_5 bulk loss

The measured propagation losses in our waveguide are 6.8 dB cm^{-1} in TM and 37.1 dB cm^{-1} in the TE polarization (see Fig. 3c of the main text). These two values together with waveguide loss simulation with complex refractive index allow us to estimate both the bulk absorption loss in the Ta_2O_5 film and the lateral leakage in the TM polarization.

The TE mode loss is assumed to come only from the material absorption. We neglect the scattering loss, which we assume sufficiently low at 2.566 µm as the scattering scales with λ^{-4}. Further, we assume a single-mode TE propagation in this scenario because 1) it is unlikely that the antisymmetric first-order mode will be efficiently excited, 2) due to large lateral extent it will experience strong loss due to the etching openings, and 3) the measured decay is well-described by a single exponential function. By varying the imaginary part of the Ta_2O_5 refractive index,

$n = n' + i\,n''$, we found the best fit with the measured loss value for $n'' = 0.000225$, which corresponds to bulk absorption of 47.9 dB cm^{-1}.

The same n'' yields a loss of 6.1 dB cm^{-1} in the TM polarization, which is in a good agreement with our measurement. The simulation also allows us to discriminate that 4.6 dB cm^{-1} of the total loss comes from the material absorption and 1.5 dB cm^{-1} from the lateral leakage (calculated with $n'' = 0$). The substantially lower absorption loss for the TM mode is a result of weaker confinement in the waveguide core material. Our simulations showed, that the confinement factor in Ta_2O_5 is about 77 % for the TE mode, while it is as low as 9 % for the TM mode.

S6) Saturation of Lambert–Beer absorption

Saturation of linear Lambert–Beer absorption can occur under intense incident irradiation. At sufficiently large intensities, the optical pumping rate on an absorbing transition becomes larger than the relaxation rate, resulting in intensity-dependent decrease of the population in the absorbing level. This manifests as a decrease in absorption coefficient and an additional line broadening.[8] While optical field in free-space beams has a typical mode area of 1–10 mm^2, in photonic waveguides the same optical power is confined to a much smaller area of approx. 0.1–10 μm^2. This results in orders of magnitude higher optical intensities and makes it possible to enter saturation regime at laser powers typical for state-of-the-art laser diodes.

In our experimental case, simulation of the optical field distribution in the waveguide gives a mode area of 3.4 μm^2 with maximum normalized intensity of 1.75×10^{11} m^{-2}. The laser is operated at the power of 15 mW, of which about 8.5 mW is coupled into the waveguide when a measured coupling loss of 2.5 dB is considered. The resulting maximum intensity in the waveguide is 2.5×10^{9} W m^{-2}.

If we assume a two-level system dominated by collisional (pressure) broadening, the saturation intensity can be expressed as

$$I_s = \frac{\varepsilon_0 c \hbar^2 \gamma^2}{2\mu^2},$$

Where γ is the pressure-broadened linewidth and μ the dipole moment of the transition.[9,10] μ can be further expressed by the Einstein coefficient A_{ij} and the transition frequency ν_{ij} as[11]

$$\mu^2 = \frac{A_{ij}\, 3\varepsilon_0 h c^3}{16\pi^3 \nu_{ij}^3}.$$

Saturation of Lambert–Beer absorption will occur if the maximum intensity of the guided mode becomes comparable or exceeds I_s. From the HITRAN2016 database,[12] the typical transition dipole moment for lines of the C_2H_2 Q-branch centered at 2.566 μm (3897 cm^{-1}) is $\mu = 4.4 \times 10^{-3}$ D or 1.48×10^{-32} C m and the pressure broadened linewidth at atmospheric pressure 2.7 GHz, giving a saturation intensity $I_S \cong 5 \times 10^{11}$ W m^{-2}.

With maximum intensity in the waveguide of 2.5×10^9 W m^{-2}, still more than 2 orders of magnitude lower than the saturation intensity, saturation of absorption is not occurring at our experimental conditions. This is partly due to the relatively large mode area of our waveguide design resulting from strong optical field delocalization. The absence of saturation was also confirmed experimentally by comparing the lineshapes of the waveguide and the free-space configuration, which appear identical. Nevertheless, saturation may become relevant and the saturation condition must be revisited at lower gas pressures or if detection of gases with distinctly stronger transition dipole moment is targeted.

References

1. Visser, T. D., Blok, H., Demeulenaere, B. & Lenstra, D. Confinement factors and gain in optical amplifiers. *IEEE J. Quantum Electron.* **33**, 1763–1766 (1997).
2. Robinson, J. T., Preston, K., Painter, O. & Lipson, M. First-principle derivation of gain in high-index-contrast waveguides. *Opt. Express* **16**, 16659–16669 (2008).
3. Ottonello-Briano, F. *et al.* Carbon dioxide absorption spectroscopy with a mid-infrared silicon photonic waveguide. *Opt. Lett.* **45**, 109 (2020).
4. Kogelnik, H. Theory of Optical Waveguides. in *Guided-Wave Optoelectronics* (ed. Tamir, T.) vol. 26 7–88 (Springer Berlin Heidelberg, 1988).
5. Webster, M. A., Pafchek, R. M., Mitchell, A. & Koch, T. L. Width Dependence of Inherent TM-Mode Lateral Leakage Loss in Silicon-On-Insulator Ridge Waveguides. *IEEE Photonics Technol. Lett.* **19**, 429–431 (2007).
6. Tsige Dullo, F., Tinguely, J.-C., Andre Solbo, S. & Helleso, O. G. Single-Mode Limit and Bending Losses for Shallow Rib Si_3N_4 Waveguides. *IEEE Photonics J.* **7**, 1–11 (2015).
7. Zhang, X. *et al.* Guiding of visible photons at the ångström thickness limit. *Nat. Nanotechnol.* 1–7 (2019) doi:10.1038/s41565-019-0519-6.
8. Demtröder, W. Widths and Profiles of Spectral Lines. in *Laser Spectroscopy: Basic Concepts and Instrumentation* (ed. Demtröder, W.) 78–114 (Springer, 1981). doi:10.1007/978-3-662-08257-7_3.
9. Castrillo, A., Tommasi, E. D., Gianfrani, L., Sirigu, L. & Faist, J. Doppler-free saturated-absorption spectroscopy of CO_2 at 4.3 μm by means of a distributed feedback quantum cascade laser. *Opt. Lett.* **31**, 3040–3042 (2006).
10. Shimoda, K. Line broadening and narrowing effects. in *High-Resolution Laser Spectroscopy* (ed. Shimoda, K.) 11–49 (Springer, 1976). doi:10.1007/3540077197_18.
11. Absorption and Emission of Light. in *Laser Spectroscopy: Vol. 1 Basic Principles* (ed. Demtröder, W.) 5–60 (Springer, 2008). doi:10.1007/978-3-540-73418-5_2.
12. Gordon, I. E. *et al.* The HITRAN2016 molecular spectroscopic database. *J. Quant. Spectrosc. Radiat. Transf.* **203**, 3–69 (2017).

Paper II

Single-Mode Porous Waveguides through Sol-Gel Chemistry: A New Platform for Gas Sensing

S. Alberti, A. Datta, M. Vlk, and J. Jágerská

Optics Letters, submitted

Single-mode porous waveguides through sol-gel chemistry: a new platform for gas sensing

SEBASTIÁN ALBERTI[1], ANURUP DATTA[1], MAREK VLK[1], JANA JÁGERSKÁ[1]

[1]Department of Physics and Technology, UiT The Artic University of Norway, Klokkargårdsbakken 35, 9019 Tromsø, Norway
**Corresponding author: Sebastian.alberti@uit.no*

Received XX Month XXXX; revised XX Month, XXXX; accepted XX Month XXXX; posted XX Month XXXX (Doc. ID XXXXX); published XX Month XXXX

Permeable enrichment claddings have improved the gas sensing performance of optical waveguides significantly, however, most of the optical field still resides within the core of the waveguide and remains inaccessible to the analyte. A material platform where the waveguide core plays an active role in the sensing is thus highly desirable. We designed and manufactured a highly porous (38%) single-mode rib waveguide and demonstrated its performance for gas sensing using selective and sensitive tunable diode laser absorption spectroscopy. We proved experimentally that molecules diffusing through the pores interact with the optical mode inside the core material, leading to almost an order of magnitude enhancement of interaction with the analyte compared to identical waveguides with a solid core.

1. Introduction

On-chip photonics for infrared (IR) absorption spectroscopy has attracted increasing interest in the recent years as a means to miniaturize free-space-based spectroscopic instrumentation [1], [2]. Since the introduction of ATR crystals for characterization of highly absorbent liquids and solids in the IR, optical fibers and lately integrated waveguides have received growing attention as a route to increased light–analyte interaction and thus extended the applicability of the technique to weakly absorbing gaseous analytes. Despite numerous advantages this strategy holds, low evanescent field confinement factor and limited pathlengths of waveguides due to mid-IR absorption and scattering have limited their applications. To override these challenges, the scientific community has introduced sophisticated waveguide designs such as slot or self-standing waveguides [3], [4] and a careful selection of the materials and processes [5], [6]. An alternative strategy, used so far mainly in label-free refractive index and Raman sensors, uses an adsorptive layer on top of the waveguide with the ability to preconcentrate the analyte of interest, thus increasing the sensitivity and selectivity [7], [8].

Two main approaches for the design of an adsorptive layer have been followed. Specific recognition sites can be tethered to the surface as monolayers, i.e. antibodies, enzymes, receptors, aptamers or nucleic acids [9], [10]. Alternatively, gas-permeable claddings capable of increasing the residence time of the molecules of interest near the surface within the extent of the evanescent field have been used. In particular, the last scheme was appraised by the use of polymer claddings, and sol-gel porous thin films. Both were introduced as cover layers over ATR crystals to increase the detection limit due to absorption and capillary condensation during the first half of 90' decade by the group of Lubbers and Dunbar respectively, and Lopez years later [11]–[13]. Surprisingly, although the advantages were first suggested in 1993 by MacCraith [14], it was not before recent years a similar approach was followed for integrated waveguides for spectroscopic sensing [15],.

Despite the improvement of the detection limit through the use of properly engineered claddings, results can still ameliorate substantially if the analyte molecules are able to diffuse into the core of the waveguide and interact with the optical mode within. Based on this idea, polymers and hydrogels have been used as the main constituent for ATR sensing and multimode waveguide sensor designs [16], [17]. Although versatile and simple, this approach holds several disadvantages, which are detrimental for spectroscopy applications as elaborated below. Multimode waveguides are prone to cross-coupling between several modes leading to inferior signal to noise ratio than that of single mode waveguides. Additionally, longer pathlengths and therefore smaller footprints are limited in case of multimode waveguides where bending losses play an important role. From a material point of view, polymers are soft materials, which structure, thickness, and refractive index can change during the measurement due to environment conditions. Additionally, diffusion of the analyte within the polymer may be slow, increasing the response time of the sensors [18]. In this context, porous sol-gel layers present a promising alternative as a material platform for single-mode gas permeable waveguide designs [19].

In this work, we present the first single-mode titanium oxide rib waveguide with a mesoporous-core layer synthesized through sol-gel chemistry. The porous core allows for high interaction between the analyte and the optical field. The degree of light-matter interaction with gaseous analyte in the porous core is experimentally verified through tunable diode laser absorption spectroscopy (TDLAS) with acetylene as a calibration gas. To the best of our knowledge, no attempt to create such a waveguide for spectroscopy sensing has been reported so far.

2. Results and discussion

Mesoporous titanium oxide thin film layers were deposited through sol-gel chemistry following minimally adapted protocols that were previously reported in [20]. An ethanolic solution of TiCl4 and pluronic F127 with a final molar ratio Ti:H$_2$O:EtOH:F127 of 1:10:40:0.005 was spin-coated at 1800 rpm and heated stepwise to 60, 130 and 350 °C, for 2 hours. The structure of the layer was characterized by Atomic force microscopy (AFM), Scanning electron microscope (SEM), and Quartz crystal microbalance (QCM). A single titanium oxide layer is limited in thickness to approx. 310 nm as micro cracks start to develop for thicker films creating an undesirable source of light scattering. Although such layer can support a guided mode, a substantial portion of the guided mode travels in the silica substrate, limiting the confinement in the porous core. A thicker film is required to better confine light in the vertical direction, which we achieved by deposition of two thinner consecutive layers: The first layer was treated to 200 °C for two hours and the additional layer was spin-coated on top, resulting in a total of 440 nm thickness. The average pore size was calculated from AFM (Cypher S AFM from oxford instruments) and SEM (Carl Zeiss, Merlin) images as shown in Fig. 1a and Fig. 1b, respectively. Both methods gave a median pore diameter of approximately 10 nm. Pore size and porous volume were additionally calculated from water vapour adsorption isotherm in nitrogen measured with a QCM (MicroVacuum Ltd. QCM-I) (Fig. 1c) [21], [22]. For this purpose, films were deposited under identical conditions over a quartz crystal sensor and their weight variation was tracked upon exposure to nitrogen flow of controlled humidity. The increase in weight with increasing humidity is attributed to adsorption and capillary condensation of water in the porous layer (Fig 1c). Capillary condensation leads to the hysteresis in the water adsorption isotherm, which it is characteristic of a mesoporous structure. Pore size distribution with a median size of 8 nm in diameter (Fig. 1d) was calculated from the isotherm based on a modified kelvin equation [23]. The accessible porous volume calculated from the total weight of the adsorbed water was 38%, in agreement with similar measurements done by ellipsometry for the same protocol [24]. The refractive index can be estimated from the effective medium approximation theory proposed by Bruggeman. Bulk amorphous titanium oxide refractive index and air refractive index can be used to calculate the effective medium refractive index of the porous material if its porous volume is known. The refractive index of the amorphous bulk titanium oxide of n = 2.09 at 1520 nm was considered. It was determined from ellipsometry measurements done for a similar layer based on the same synthesis protocol measured at 630 nm [24] and recalculated for 1520 nm by accounting for titania dispersion. The resulting refractive index of the porous layers was found equal to n = 1.68.

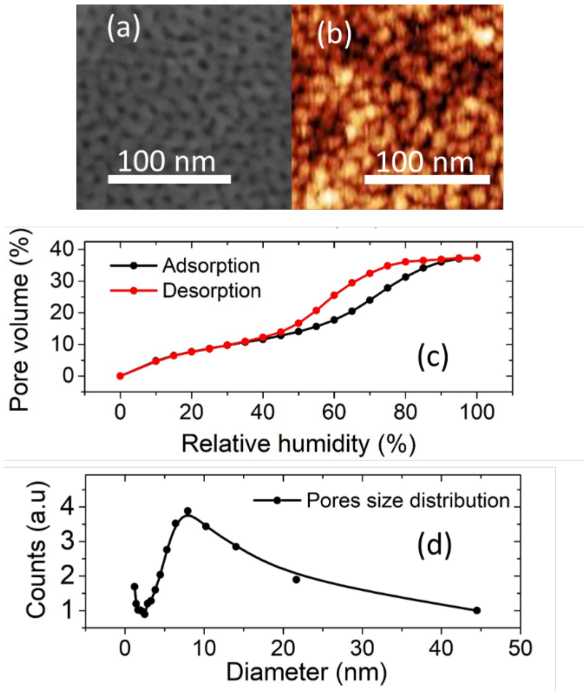

Fig. 1. High magnification SEM (a) and AFM (b) image of the mesoporous titania thin film. c) Water adsorption isotherm measured with QCM. d) Pore size distribution calculated from the isotherm in (c).

The structural dimensions of the rib waveguides (rib width, w, and rib height, s) were designed using Lumerical MODE software to guarantee single mode performance and minimum bending losses for TE polarization (Fig. 2a). The optimum waveguide rib width was found to be 3 μm for both layer thicknesses. 70 nm rib height was chosen for the single layer (Fig. 2b) and 100 nm for the double layer to simultaneously avoid excessive bending losses and minimize the side wall scattering. A single step standard UV-lithography process followed by ICP–RIE etching (Oxford Instruments, Plasmalab 100) with CHF$_3$/O$_2$ gas mixture were used to pattern the waveguides. AFM and SEM (Fig. 2c) show a 67.5 and 100 nm step for the single- and double-layer designs, respectively, and the width of 3 μm in agreement with the design. The surface roughness measured by AFM was 0.4 and on the top surface of the rib and 0.6 nm on the etched horizontal surfaces. Straight waveguides and spirals with a total length of 1, 2, and 3.15 cm were patterned on a chip with 1 × 1 cm^2 footprint (Fig. 2d), using a minimum variation curve for the spiral pattern to minimize transition losses [25]. The guiding and sensing performance of the waveguides were characterized in an end-fire configuration in a combined imaging and spectroscopy setup shown in Fig. 3a. A TE-polarized PM-fiber-coupled diode laser (Exfo, T100S-HP) continuously tunable from 1500 to 1680 nm (5952–6666 cm-1) was used as the light source. The fiber output from the laser was collimated using a parabolic mirror (Thorlabs, MPD00M9-P01) and was subsequently coupled into the waveguides

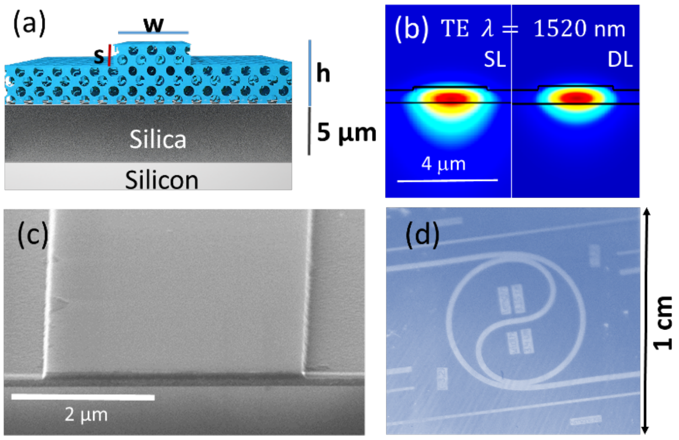

Fig. 2. a) Schematics of the porous rib waveguide with the main geometrical features: h (layer thickness), w (rib width) and s (step height). b) Simulated electric field distribution in the cross section of a single-layer (SL) and double layer (DL) sample for 1520 nm and TE polarization. c) SEM image of the cross section of the rib waveguide for a single-layer sample. d) Photograph for a 3.15 cm long rib waveguide spiral.

through an antireflection-coated aspheric lens (NA = 0.5, Thorlabs, C240TMD-C). Another similar aspheric lens was used to collect the transmitted light, which was then spatially cleaned by passing through an iris and finally focused on a Ge photodiode power sensor (Thorlabs, S132C). A NIR camera (Raptor Photonics, Ninox 640) was used to image the waveguide surface, aid the in-coupling to the waveguide, and determine the propagation loss from the decay of the out-of-plane scattered light. For the 310 nm thick single layer waveguide design, as measured on straight waveguides, the propagation loss was found to be 2.2 dB/cm at 1520 nm while it was 13 dB/cm for the 440nm thick double layer design (Fig 3b). For the single layer structure, the loss is mainly attributed to material absorption and substrate leakage (Fig. 2b). Although absorption of bulk TiO_2 is 10 times lower than that of silicon at 1520 nm, the presence of –OH or adsorbed water in the porous network increase the absorption loss [26][27]. This issue was to a large degree addressed by annealing the sample before the measurements at 275 °C; However, more permanent solution such as hydrophobic postgrafting functionalization is required for practical applications. Higher loss in the double layer structure is a direct consequence of a larger overlap of the optical mode with the porous layer (Fig 2b) and a visibly increased scattering due to inhomogeneity at the interface between the two layers. Losses due to lithography processing and pore dimensions are considered low as can be deduced from negligible scattering in the single layer waveguides, which is also supported by the low roughness obtained from the AFM measurements.

TDLAS-based spectroscopic measurements with a probe gas of known concentration were performed to prove that the pore structure leads to an increase in the interaction between the optical mode confined in the waveguide and the analyte molecules. The interaction strength between the optical field and the analyte can be quantitatively expressed in terms of a confinement factor given as

$$\Gamma_i = \frac{n_g}{\mathrm{Re}\{n_\mathrm{i}\}} \frac{\iint_\mathrm{i} \varepsilon |\mathbf{E}|^2 dxdy}{\iint_{-\infty}^{\infty} \varepsilon |\mathbf{E}|^2 dxdy},$$

where Γ_i is the confinement factor in the layer i, n_g is the group index of the guided mode, n_i is the refractive index of the layer i, $\varepsilon(x, y)$ is the permittivity, and $\mathbf{E}(x, y)$ is the electric field. For the porous waveguide structure, the analyte is able to interact with the field within the core as well as with the evanescent field in air above the core, and, hence, the total confinement factor, Γ_{tot} can be written as $\Gamma_{tot} = \Gamma_{core} V_p + \Gamma_{air}$, where V_p is the accessible porous volume. As the light travels through the waveguide and interacts with the analyte, the transmitted intensity is governed by the modified form of the Lambert–Beer's law which accounts for the confinement factor as given by $I = I_0 \exp[-\alpha \Gamma_{tot} L]$. Here, I is the transmitted intensity of light, I_0 is the incident intensity of light, α is the absorption coefficient of the surrounding environment, and L is the total interaction length. When the spectral characteristics of the transmitted light through the waveguide are compared with the expected theoretical spectrum for the free space obtained e.g. from the HITRAN database [28], the information about the underlying confinement factor Γ_{tot} can be revealed.

For the realization of the spectroscopy experiment and in order to provide a controlled environment in terms of gas concentration and pressure, the sensing area for a 1 × 1 cm^2 chip was enclosed in a 0.6 cm long custom gas flow cell and sealed with a PDMS ring as depicted in Fig. 3a. In this configuration, the active length of the waveguide in contact with the gas is by 0.4 cm shorter than the nominal length of the waveguide, leaving 0.2 cm on each side of the cell open to the ambient for in-coupling and outcoupling purposes. Calibrated mixture of acetylene (10% C_2H_2 in N2) with its $\nu_1 + \nu_3$ combination absorption band at 1510 – 1540 nm was chosen as the analyte and supplied to the gas cell at a constant flow of 10 ml/min. The TDLAS setup was then operated between 6576 and 6581 cm^{-1} (1519.6 – 1520.6 nm) to scan across a strong acetylene absorption peak near 6578.6 cm^{-1} (1520 nm). The experimental transmission spectrum for a nominally 2 cm long double layered spiral waveguide is shown in Fig. 3c. The raw spectrum was first corrected for the background and then fitted with the reference spectrum from the HITRAN database to precisely quantify the amplitude of the absorption peak. This amplitude, scaled by the active waveguide length of 1.6 cm, yields the concentration of the analyte seen by the waveguide, which resulted in a value of 2.6%. Since the reference concentration of C_2H_2 is 10%, this means that 26% of the waveguide field interacts with the surrounding gas molecules. This is in excellent agreement with a theoretical value of Γ_{tot} = 24.7% obtained from simulations for the same waveguide dimensions and the pore volume. In an identical non-porous waveguide structure, the total confinement factor comes only from the contribution of the evanescent field above the waveguide surface, which was simulated to be 3.5%. Thus, our result indicates a 9-fold improvement in the interaction capability of the porous waveguide with the analyte as compared to a non-porous one. Similar TDLAS experiment performed for a single layer waveguide yielded the confinement factor of 9%., which agrees well with the simulated Γ_{tot} = 10% and gives about 3-fold improvement over an identical non-porous device.

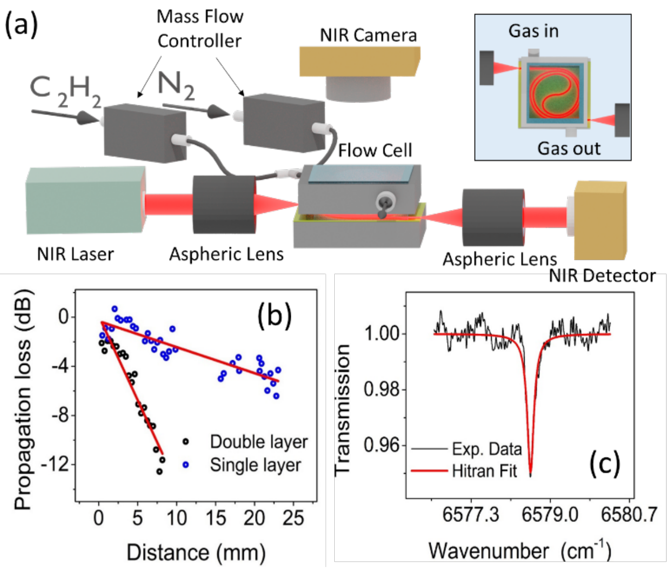

Fig. 3. a) Schematics of combined spectroscopy and loss characterization setup. b) Losses for a single layer (2.2 dB/cm) and a double layer (13 dB/cm) waveguide measured from the decay of out-of-plane scattering. c) Transmission spectrum for acetylene measured in a 2 cm-long double layer waveguide with a HITRAN fit corresponding to a confinement factor of 26%.

3. Conclusions

In this work, we demonstrated the first single-mode sol-gel mesoporous waveguide for gas sensing applications. The interconnected porous structure of the waveguide facilitates rapid diffusion of analyte gas molecules directly into the waveguide core, thus increasing the light-matter interaction capability of the waveguide by about one order of magnitude as compared to analogous conventional thin film waveguides. This was verified through TDLAS detection of acetylene, where the experimental air confinement factor of 26% was found to be in a close agreement with simulations based on nominal waveguide dimensions and the independently measured pore volume of 38%. Further, our transmission measurements confirmed that the sub 10 nm pores do not induce substantial scattering at 1520 nm, as was concluded from the low losses (2.2 dB/cm) measured in the single layer waveguides. Nevertheless, notable scattering on interfaces in multilayer devices as well as absorption due to presence of –OH or adsorbed humidity inside the porous network need to be addressed to make these structures fit for real-world applications.

We believe that our demonstrated mesoporous waveguide platform would complement and advance the outstanding performance of mesoporous thin films typically used as claddings in previous reports. Taking advantage not only from the high pore volume but also from the large surface area of the porous network (150-250 m^2/g) we envision applications combining surface adsorption enrichment with Raman scattering or absorption spectroscopy. Proper surface functionalization will suppress unwanted signal from residual humidity, and incorporate specific recognition sites to increase sensitivity and selectivity towards targeted analytes. With these improvements, we expect the mesoporous waveguides to find applications in industrial gas detection and defense, and to become an alternative to current lab-on-a-chip devices.

Funding sources and acknowledgments. This project has received funding from the European Research Council (ERC) under the European Union's Horizon 2020 research and innovation program (grant agreement 758973). The work was also supported by the Research Council of Norway (grant no. 262608) and Tromsø Research Foundation (project ID 17_SG_JJ). The Research Council of Norway is further acknowledged for the support to the Norwegian Micro- and Nano-Fabrication Facility, NorFab, project number 295864.

Acknowledgments. The authors wish to thank Jan Torgersen, Stephanie Burgmann and Chia-Yun Lai for their help. We would also like to acknowledge Pål Vevang and UiT mechanical workshop for the fabrication of the gas flow cells.

Disclosures. The authors declare no conflicts of interest.

References

[1] T. Schädle and B. Mizaikoff, *Appl. Spectrosc.*, vol. 70, no. 10, pp. 1625–1638, Oct. 2016.
[2] A. Messica, A. Greenstein, and A. Katzir, *Appl. Opt.*, vol. 35, no. 13, p. 2274, May 1996.
[3] F. Ottonello-Briano, C. Errando-Herranz, H. Rödjegård, H. Martin, H. Sohlström, and K. B. Gylfason, *Opt. Lett.*, vol. 45, no. 1, p. 109, Jan. 2020.
[4] M. Vlk, A. Datta, S. Alberti, H. D. Yallew, V. Mittal, G. S. Murugan, and J. Jágerská, *Light Sci. Appl.*, vol. 10, no. 1, p. 26, Dec. 2021.
[5] C. Chaneliere, J. L. Autran, R. A. B. Devine, and B. Balland, *Mater. Sci. Eng.*, vol. 22, pp. 269–322, 1998.
[6] G. Beshkov, S. Lei, V. Lazarova, N. Nedev, and S. S. Georgiev, vol. 69, pp. 301–305, 2003.
[7] G. Orellana and D. Haigh, *Curr. Anal. Chem.*, vol. 4, no. 4, pp. 273–295, 2008.
[8] M. Janotta and B. Mizaikoff, vol. 4616, no. 404, pp. 1–8, 2002.
[9] M. D. Marazuela and M. C. Moreno-Bondi, *Anal. Bioanal. Chem.*, vol. 372, no. 5–6, pp. 664–682, 2002.
[10] X. J. Wu and M. M. F. Choi, *Glucose Sens.*, no. July 2005, pp. 201–236, 2007.
[11] P. Heinrich, R. Wyzgol, B. Schrader, A. Hatzilazaru, and D. W. Lubbers, *Appl. Spectrosc.*, vol. 44, no. 10, pp. 1641–1646, 1990.
[12] Y. Lu, L. Han, C. J. Brinker, T. M. Niemczyk, and G. P. Lopez, *Sensors Actuators, B Chem.*, vol. 36, no. 1–3, pp. 517–521, 1996.
[13] J. I. Dulebohn, S. C. Haefner, K. A. Berglund, and K. R. Dunbar, *Chem. Mater.*, vol. 4, no. 3, pp. 506–508, May 1992.
[14] B. D. MacCraith, *Sensors Actuators B Chem.*, vol. 11, no. 1–3, pp. 29–34, Mar. 1993.
[15] N. T. Benéitez, B. Baumgartner, J. Missinne, S. Radosavljevic, D. Wacht, S. Hugger, P. Leszcz, B. Lendl, and G. Roelkens, *Opt. Express*, vol. 28, no. 18, p. 27013, Aug. 2020.
[16] H. Ma, A. K.-Y. Jen, and L. R. Dalton, *Adv. Mater.*, vol. 14, no. 19, pp. 1339–1365, Oct. 2002.
[17] J. Guo, M. Zhou, and C. Yang, *Sci. Rep.*, no. April, pp. 1–8, 2017.
[18] B. Pejcic, L. Boyd, M. Myers, A. Ross, Y. Raichlin, A. Katzir, R. Lu, and B. Mizaikoff, *Org. Geochem.*, vol. 55, pp. 63–71, Feb. 2013.
[19] S. Alberti and J. Jágerká, *Front. Mater.*, 2021.
[20] S. Alberti, P. Y. Steinberg, G. Giménez, H. Amenitsch, G. Ybarra, O. Azzaroni, P. C. Angelomé, and G. J. A. A. Soler-Illia,, *Langmuir*, vol. 35, no. 19, pp. 6279–6287, May 2019.
[21] R. Etchenique and V. L. Brudny, *Langmuir*, vol. 16, no. 11, pp. 5064–5071, May 2000.
[22] P. Schön, R. Michalek, and L. Walder, *Anal. Chem.*, vol. 71, no. 16, pp. 3305–3310, 1999.
[23] C. Boissiere, D. Grosso, S. Lepoutre, L. Nicole, A. B. Bruneau, and C. Sanchez, *Langmuir*, vol. 21, no. 26, pp. 12362–71, Dec. 2005.
[24] B. Auguié, M. C. Fuertes, P. C. Angelomé, N. L. Abdala, G. J. A. A. Soler Illia, and A. Fainstein, *ACS Photonics*, vol. 1, no. 9, pp. 775–780, Sep. 2014.
[25] T. Chen, H. Lee, J. Li, and K. J. Vahala, vol. 20, no. 20, pp. 555–562, 2012.
[26] A. Kanta, R. Sedev, and J. Ralston, *Langmuir*, vol. 21, no. 6, pp. 2400–2407, Mar. 2005.
[27] J. Guo, X. Cai, Y. Li, R. Zhai, S. Zhou, and P. Na, *Chem. Eng. J.*, vol. 221, pp. 342–352, 2013.
[28] I. E. Gordon *et al.*, *J. Quant. Spectrosc. Radiat. Transf.*, vol. 203, pp. 3–69, Dec. 2017.

Paper III

Free-Standing Waveguides for Sensing Applications in the Mid-Infrared

M. Vlk, A. Datta, S. Alberti, G. S. Murugan, A. Aksnes, and J. Jágerská

Optical Materials Express, submitted

Free-Standing Waveguides for Sensing Applications in the Mid-Infrared

MAREK VLK,[1,*] ANURUP DATTA,[1] SEBASTIÁN ALBERTI,[1] GANAPATHY SENTHIL MURUGAN,[2] ASTRID AKSNES,[3,1] AND JANA JÁGERSKÁ,[1,3,**]

[1]*Department of Physics and Technology, UiT The Arctic University of Norway, NO-9037 Tromsø, Norway*
[2]*Optoelectronics Research Centre, University of Southampton, Southampton, SO17 1BJ, UK*
[3]*Department of Electronic Systems, Norwegian University of Science and Technology, 7491 Trondheim, Norway*
**marek.vlk@uit.no, **jana.jagerska@uit.no*

Abstract: Typical applications of integrated photonics in the mid-infrared (MIR) are different from near-infrared (telecom) range and, in many instances, they involve chemical sensing through MIR spectroscopy. Such applications necessitate tailored designs of optical waveguides. Both cross-sectional designs and processing methods of MIR waveguides have been a subject of extensive research, where material transparency and substrate leakage of guided modes have been the most common challenges. Both these challenges can be solved simultaneously with air-suspended waveguides. In this paper, tantalum pentoxide (Ta_2O_5, tantala) thin films deposited on silicon were tested for two different dry under-etching procedures, XeF_2 and SF_6 plasma, with both of them facilitating selective removal of silicon. We analyze the advantages and limitations of these two methods and optimize the processing for fabricating membranes with arbitrary length and cross-sectional aspect ratio over 300. The performance of these high-aspect-ratio membranes as a framework for single-mode waveguides is rigorously analyzed at 2566 nm wavelength. With tantala being transparent up to 10 µm wavelength, such waveguides are particularly well suited for gas sensing in MIR.

1. Introduction

Integrated mid-infrared (MIR) photonics holds promise for new applications outside of telecom such as chemical and biological sensing [1]. However, as a young area of study, it presents researchers with several challenges in the development of both active and passive components. Material transparency, being the major challenge, is limited by the onset of phonon absorption at longer wavelengths, requiring careful material selection. Optical materials have been recently reviewed showing multiple candidates for adoption in MIR such as chalcogenide glasses, semiconductors, or metal oxides [2–4]. However, besides the intrinsic absorption mechanisms, materials may often contain residuals which cause additional propagation loss. Particularly in amorphous materials, the most detrimental residuals are water [5–7] and hydroxyl groups in oxides [8], as well as N–H bonds in nitrides [9–11]. Fortunately, their content can be reduced by improving material packing density and by annealing. Material challenges in optical waveguides, mainly absorption, can also be solved by careful design. Optical waveguides can be engineered to minimize light confinement in a lossy material. It has been reported that the silicon-on-insulator (SOI) platform can be used beyond the silica transparency edge at ~3.6 µm with strong light confinement in a relatively thick silicon waveguide core [12]. Nevertheless, if the optical mode is nearly entirely confined in the solid core, the interaction with the surrounding environment is minimal and such waveguides are then ill-suited for applications in sensing.

Another common obstacle at longer wavelengths is substrate leakage. Commercially available wafers, originally intended for telecom applications, exhibit bottom claddings too thin relative to the wavelength and light distribution in the MIR and fail to isolate the guided mode from the substrate. Suspending the waveguide in air can directly avoid this issue. Such an architecture allows for a maximum refractive index contrast, keeping the light further away from the substrate. In this context, much attention has been given to the SOI material platform, where silicon waveguides have been suspended via selective removal of SiO_2 by HF etching [13–16]. Free-standing germanium waveguides have been made in a similar way from either germanium-on-insulator (GOI) [17] or Ge-on-SOI [18]. In an alternative approach, silicon has been removed directly from below the device layer, allowing the air cladding to be extended as much as needed in contrast to the limited oxide thickness. Diamond waveguides have been under-etched in SF_6 plasma [19] while dry etch with XeF_2 has been used to release SiO_2 microdisks [20] and silicon waveguides on thin oxide membrane [21] for operation in the near-infrared (NIR) domain. Moreover, the MIR transparency range of silicon has been fully exploited by wafer bonding [22]: The air cladding has been first defined as trenches in a silicon wafer and a silicon device layer has been bonded over the wafer. Waveguides have been finally patterned onto the membranes, which resulted in an all-silicon structure. However, the full protocol is rather complex.

In this paper, we report on processing tantalum pentoxide (Ta_2O_5, tantala) into air-suspended waveguides to tackle the challenges of core material absorption and substrate leakage. We chose a design of a free-standing membrane with a rib waveguide [13,17–19,22,23] and optimized its dimensions for spectroscopic detection with TM-polarized light in the MIR. The optical field is strongly delocalized, which has the following consequences: The light–matter interaction in air is unprecedently strong and the field extends far from the waveguide core, requiring large air buffer between the waveguide and the substrate. In the present approach, the device layer rests directly on top of a silicon wafer which is then selectively, locally removed from below the waveguides and results in thick air cladding, which isolates the guided light from the substrate. For the purpose of the under-etching, we compare spontaneous etching with XeF_2 gas and plasma etching with SF_6 in terms of material selectivity, suitable masking materials, etch profile, and ease of processing.

2. Design

Air-suspended waveguides can effectively remove substrate leakage and, if sufficiently thin, they can increase the overlap of the guided light with the surrounding air cladding. Our waveguide (Fig. 1) is formed by a shallow rib in the tantala membrane. It was modeled with finite-difference eigenmode solver MODE (Lumerical) to determine appropriate dimensions for the TM-polarized light at 2566 nm. We identified four figures of merit that depend on the dimensions and thus allow finding the optimal design in terms of light–analyte interaction and propagation loss. First, it is the external confinement factor Γ_{ext} [23–27], which quantifies the interaction strength outside the waveguide core. It depends mainly on the membrane thickness T and remains unaffected by the rib width W or etch depth E. Second, the lateral leakage, characteristic for TM modes in rib waveguides [28], shows minima dependent on the rib width W while the magnitude is driven by the etch depth E. Third, bending loss is a function of all dimensional parameters but mainly E. Fourth, and last, the waveguide needs to support a single mode at the selected polarization. While Γ_{ext} is nearly the same for different TM modes in multimode devices, propagation loss due to the lateral leakage and bends varies. Intermodal interaction leads to increased noise, and in some cases completely hinders a correct interpretation of the transmission signal.

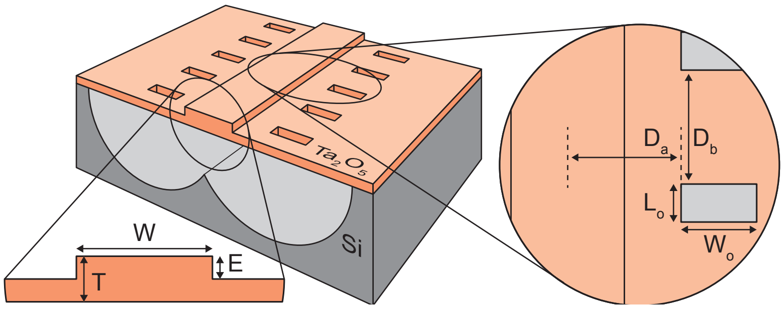

Fig. 1. Schematics of the air-suspended tantala waveguide. The cross-sectional parameters include the as-deposited layer thickness T, rib width W, and etch depth E. The top view shows etching openings, which facilitate the under-etching. $W_o \times L_o$ are the openings dimensions and D_a and D_b are the lateral and longitudinal spacings.

For tantala as the waveguide core material, Γ_{ext} reaches maximum of 109 % around 400 nm device layer thickness T for the wavelength of 2566 nm (Fig. 2a). Fig. 2b indicates the positions of lateral loss minima for T = 400 nm and etch depth E = 50 nm. Fig. 2c shows the single-mode condition in the E–W parameter space where only a single mode is supported anywhere below the curve. Based on these calculations, we targeted the loss minimum around 4.7 µm rib width with 50 nm etch depth close to the single-mode threshold in order to maintain the bending loss below 0.1 dB per 90° for 1 mm radius of curvature. A higher etch depth decreases the bending loss further but also increases the maximum lateral leakage [29]. The model for T = 400 nm, E = 50 nm, and W = 4.7 µm also predicts a uniquely low end-fire in-coupling loss (Fig. 2d) with a minimum of 0.65 dB for a 4.2 µm beam diameter.

The under-etching is done from the front side and therefore necessitates etching openings through the device layer. The openings must be positioned sufficiently far from the waveguide not to disturb the guided mode. We approximated the effect by placing perfectly matched layers (absorbing boundary conditions) on the sides of the simulation domain and varied the domain width. The effect should be negligible already around $D_a = 20$ µm. The dimensions of the etching openings were determined experimentally as discussed later.

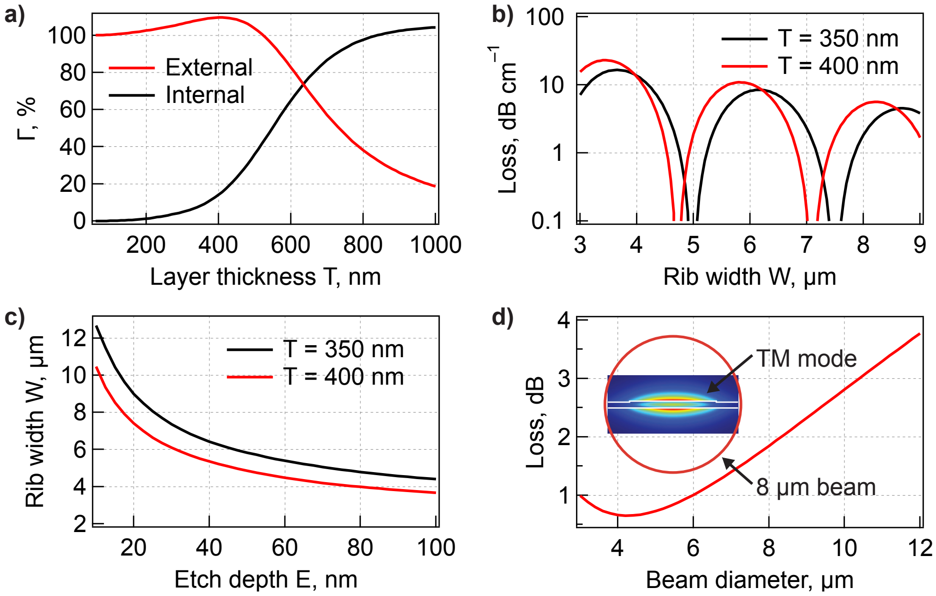

Fig. 2. Waveguide model results for TM polarization and at 2566 nm wavelength for E = 50 nm, and $n_{Ta2O5} = 2.1$. Layer thickness and rib width are T = 400 nm and W = 4.7 µm if not stated otherwise. **a)** Confinement factor Γ in air

(external, Γ_{ext}) and in the core material (internal, Γ_{int}) as a function of layer thickness T. **b)** Propagation loss due to lateral leakage of the rib waveguide guided TM mode. **c)** Single-mode condition in the E–W parameter space. **d)** In-coupling loss between a free-space beam and the fundamental TM mode. Inset illustrates the overlap between the TM mode power (P_z) distribution and Gaussian beam focus of 8 µm diameter, where the ring indicates 1/e power level.

3. Processing

Tantala thin films can be prepared by various methods [30] such as physical vapor deposition (PVD) [6,7,31–34], chemical vapor deposition (CVD) [35], or from a solution [36–38], and it features high refractive index, typically around 2.1 in the NIR. The potential of tantala in integrated optics has been manifested by low-loss optical waveguides of 0.78 dB cm^{-1} at 660 nm [37], and 0.65 dB cm^{-1} at 1600 nm [33], and its transparency ranges approximately from 0.5 to 10 µm. Above 10 µm wavelength, suboxides TaO and TaO_2 together with Ta–O–Ta stretching cause absorption [36]. However, the broad transparency window is often obscured by wide water and OH absorption bands, one being centered at 3 µm [6–8,36].

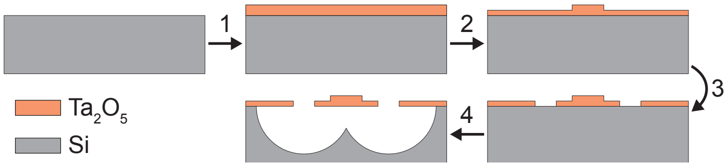

Fig. 3. Process flow for fabrication of suspended waveguides. Film deposition (1) is followed by consecutive patterning of waveguides (2) and etching openings (3). In the final step, the waveguide is under-etched (4).

The process flow for fabricating the suspended waveguides is illustrated in Fig. 3. It begins with deposition of the tantala device layer (step 1) onto a standard <100> Si wafer. We prepared 3 samples in this study as listed in Table 1 with the tantala films deposited by RF magnetron sputtering (A1, in-house), plasma-assisted e-beam evaporation (A2, purchased from Helia Photonics), and sol-gel (A3, in-house).

Following the deposition, the patterning was performed in two steps to accommodate for the difference in the etch depths of the ribs and the etching openings: The ribs are relatively shallow, up to 50 nanometers, while the etching openings need to penetrate the whole device layer(s). Table 1 lists the target values of E and W. Sample A1 was patterned with a positive tone photoresist and UV photolithography (Süss MA-6, λ = 385 nm) in hard contact mode followed by Argon ion beam milling (IBM, Oxford Instruments Ionfab 300+). Further details on the fabrication of sample A1 have been reported in [23]. For the processing of samples A2 and A3, we used mask-less lithography (Heidelberg Instruments MLA150, λ = 405 nm) followed by pattern transfer with inductively coupled plasma reactive ion etching (ICP–RIE, Plasmalab System 100 ICP–RIE 180). Plasma chemistries of CF_4 [37], C_4F_8/O_2 [32], CHF_3/Ar [38] have been reported for tantala etching and we optimized CHF_3/O_2 chemistry with flow rates 48/2 sccm, 20 mTorr pressure, 100 W RF and 1000 W ICP powers.

Table 1. Summary of processing methods and target dimensions for samples A1–A3.

Sample	Deposition method	Target layer thickness T	Shallow etching	Target dimensions		Under-etching method
				Rib width W	Etch depth E	
A1	Magnetron sputtering	350 nm	Ar IBM	4.5 µm	30 nm	XeF_2 gas
A2	E-beam evaporation	400 nm	CHF_3/O_2 ICP-RIE	4.9, 5.3, 5.7 µm	50 nm	SF_6 plasma
A3	Sol-gel	400 nm	CHF_3/O_2 ICP-RIE	—	—	SF_6 plasma

3.1 Under-etching

Two different methods of under-etching, namely XeF_2 molecular gas etching and inductively coupled plasma with SF_6, were tested and compared. Both gases primarily serve as sources of fluorine, which is highly reactive and forms volatile compounds with Si and many transition metals. Notably, XeF_2 etches Si spontaneously while SF_6 needs an external supply of energy to release fluorine radicals and ions. The etch rates with respect to the under-cut depth are functions of pressure [39–42] and aperture size [41–43] and they are nonlinear in time with respect to the under-cut depth [43].

XeF_2 dry etching was applied for under-etching of sample A1. The compound has been studied since the late 1970s for Si etching [44] and the reaction equation reads [39,45]

$$2\mathrm{XeF_2} + \mathrm{Si} \longrightarrow 2\mathrm{Xe} + \mathrm{SiF_4}.$$

Si is etched rapidly and selectively over some materials like SiO_2, Si_3N_4, Al_2O_3, or photoresists [44,46,47], rendering them suitable as mask materials. To the best of our knowledge, XeF_2–Ta_2O_5 interaction has not been studied before and therefore we tested the selectivity between the two materials. The instrument (Xactix) was operated in a pulsed mode with alternating etch steps, with XeF_2/N_2 mixture, and purge steps with N_2. Both materials were exposed from the top and we varied the XeF_2:N_2 ratio and etch pulse duration in the experiment. Total pressure and delay between the pulses were kept constant.

Samples A2 and A3 were under-etched in SF_6 plasma in ICP–RIE. Unlike the XeF_2 etcher, the ICP–RIE system operates continuously and SF_6 flow rate, process pressure, and RF and ICP powers are all variable, and can be tuned for optimum etch rate. For isotropic etching, RF source is not used (0 W power). The reactions between liberated fluorine and silicon lead again to the formation of SiF_4, but fluorine is released in the plasma by several dissociation steps

$$\begin{aligned} e + \mathrm{SF}_x &\longrightarrow \mathrm{SF}_{x-1}^- + \mathrm{F} \\ &\longrightarrow \mathrm{SF}_{x-1} + \mathrm{F}^- \\ &\longrightarrow \mathrm{SF}_{x-1} + \mathrm{F} + e \end{aligned}$$

where x = 4–6 [48]. The selectivity towards other materials is similar to that of XeF_2.

Top passivation of tantala was mandatory in both processing methods because tantala does not withstand direct exposure to the etchants. Bottom passivation was also studied by depositing thin layers of more resistant dielectrics below tantala, and the requirements were found to differ for both methods. Besides passivation, optimization of the processes was done in terms of the total etching duration, etching openings dimensions ($W_o \times L_o$), and pressures.

4. Results

Under-etching of tantala was conducted successfully with both XeF_2 in sample A1 and SF_6 plasma in sample A2. Nevertheless, notable differences were observed in the processing methods and they are discussed in the following sections in detail. After the processing was optimized, we patterned the tantala films with rib waveguides in the final fabrication rounds.

4.1 XeF_2

The Si:Ta_2O_5 selectivity was found to lie between 210 ± 40 with no clear dependence on the XeF_2:N_2 ratio or etch step duration. The large deviation is attributed to a low homogeneity of the etch rate over the etching chamber area. In addition, Fig. 4a demonstrates that tantala is removed rapidly also during under-etching. It is therefore unlikely that the recipe can be optimized for sufficient selectivity, and bottom passivation is required to make membranes with aspect ratio of 300 and more as required for the selected waveguide design. Fig. 4b shows a result with a 10 nm thick SiO_2 passivation layer inserted between silicon and tantala, which was then protected over a lateral distance of a few micrometers. Although the etch rate ratio of silicon to SiO_2 is reportedly high, ranging from less than 1000 [45] up to near infinity [44,46,49,50], it did not prove sufficient in our processing scenario. Possible causes are the quality of the oxide [51], and etching Si in proximity of SiO_2 because the XeF_2–Si reaction facilitates the release of fluorine radicals, which further attack SiO_2 [52]. Moreover, exposure through small openings has been shown to deteriorate the selectivity [45]. On the other hand, passivation with 30 nm aluminum oxide (Al_2O_3, alumina) on top of a 30 nm buffer SiO_2 layer for improved adhesion between alumina and silicon showed excellent performance with no observed degradation of the alumina film as captured in Fig. 4c.

The progression of the under-etching strongly depends on the dimensions of the openings. Early experiments showed that openings of 3×3 µm^2 (Fig. 4a,b) with D_a being either 34 or 24 µm and $D_b = 7$ µm significantly limited the etch rate. The openings were therefore enlarged to 10×5 µm^2 (Fig. 4c) and the spacings adjusted to $D_a = 24$ µm and $D_b = 25$ µm to enable complete under-etching. Final process conditions were set to 270 cycles of 5 s etch pulses with XeF_2/N_2 pressures of 3/2 Torr and 10 s purging with N_2. The resulting profile of the under-etching appears perfectly isotropic as seen in the cross section in Fig. 6a, and the membrane appears homogenous in a top view as seen with an optical microscope in Fig. 7a.

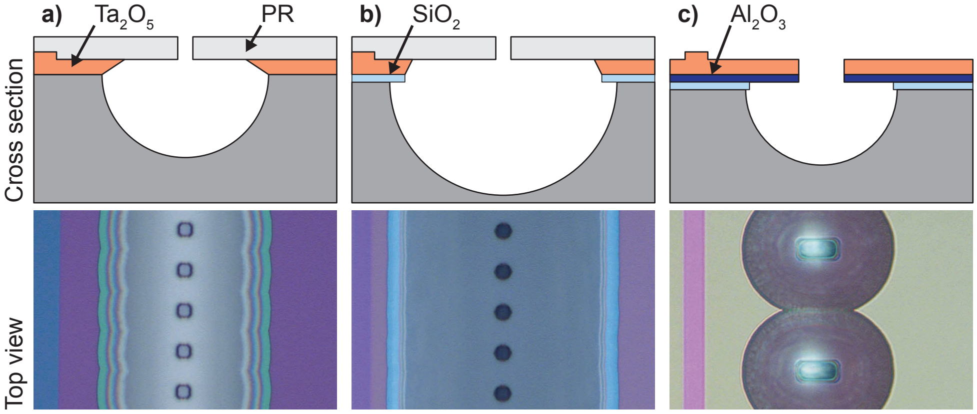

Fig. 4. Gradual inclusion of passivation layer in XeF_2 under-etching of Ta_2O_5. The etching in these images was not completed and only a single row of etching openings is displayed. Cross section provides schematics corresponding to the top view images acquired with an optical microscope. **a)** The sample was etched with no bottom passivation while the top was protected by a photoresist (PR). **b)** 10 nm SiO_2 passivation was used in the bottom. **c)** 30 nm Al_2O_3 passivation and 30 nm SiO_2 adhesion layers were used to aid the processing. The top photoresist was removed.

4.2 SF_6

The most critical parameter in the SF_6 plasma isotropic etching through small openings is the process pressure, and 50 mTorr maintained a sufficient etch rate. Fig. 5 shows samples of an under-etching progression with varying longitudinal spacing D_b and openings dimensions $W_o \times L_o$ after 30 min with 100 sccm SF_6, 50 mTorr, 1500 W ICP power. The lateral spacing $D_a = 30$ µm was fixed and followed from the numerical model. Based on this empirical test, we chose 15×7.5 µm^2 openings and $D_b = 40$ µm and extended the etching time to 60 min. The final recipe was 50 mTorr, 100 sccm SF_6 flow, 1500 W and 0 W of ICP and RF power respectively. The substrate can heat up during the process and cause the photoresist used as a mask to burn. It is therefore imperative to perform the etching in shorter sequences to let the substrate cool down. In this study, 5 min periods of etching were interlaced with 3 min plasma-less N_2 flow (50 sccm, 40 mTorr).

This recipe was applied for processing of samples A2 and A3. Sample A2, which featured SiO_2 adhesion layer and Al_2O_3 passivation layer, was successfully under-etched as shown in Figs. 6b and 7b. Sample A3, prepared with no backside passivation, also resisted the SF_6 plasma. However, high film stress resulted in cracking of the membrane and therefore the process was interrupted already after 10 min (Fig. 7c).

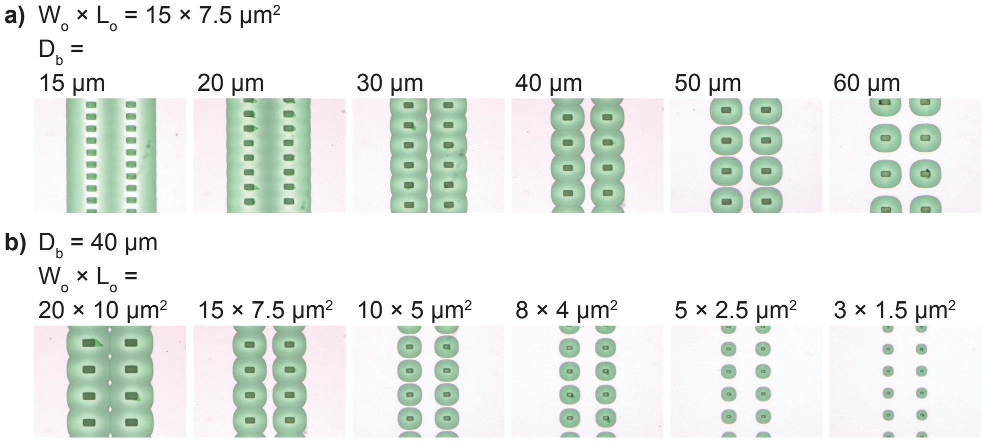

Fig. 5. Result of under-etching test in SF_6 plasma after 30 min with lateral spacing $2 \times D_a = 60$ μm between openings. **a)** Effect of different longitudinal spacings of the etching openings with dimensions 15×7.5 μm² ($W_o \times L_o$). **b)** Effect of different openings sizes with a constant longitudinal spacing $D_b = 40$ μm.

After completing the under-etching of sample A2, we observed residues on the membrane backside. These are likely leftovers of the etched materials, which were passivated against the etching by photoresist contamination in the plasma [41,53]. Stylus profiler (KLA Tencor, 2 μm diameter stylus) measurement revealed that they are about 400 nm high, and energy-dispersive X-ray spectroscopy (EDS) showed a high silicon content. It was possible to remove them with a low concentration (~1 %) tetramethyl ammonium hydroxide (TMAH) solution [19]. The TMAH also removed the passivation layers of SiO_2 and Al_2O_3, leaving a single-layer free-standing Ta_2O_5 membrane shown in Fig. 7b.

4.3 Comparison of the etching methods

Although both isotropic methods rely on producing volatile SiF_4, there are significant differences. First, the two methods result in different profiles. XeF_2 gave highly isotropic, hemispherical etch profiles as seen in Fig. 6a. Reactive species are allowed to distribute homogeneously within the forming cavity because the process is dominated by physisorption and dissociation at room temperature [46]. Meanwhile, SF_6 plasma exhibited a lower degree of isotropicity. Such quasi-isotropic profile (Fig. 6b) has also been reported elsewhere [41]. It is likely a result of the etching being dominated by direct impact of fluorine radicals [43], where any site not in the line of sight of the radical is etched slower. This effect, named neutral shadowing [54], has a visible impact on etching through small openings.

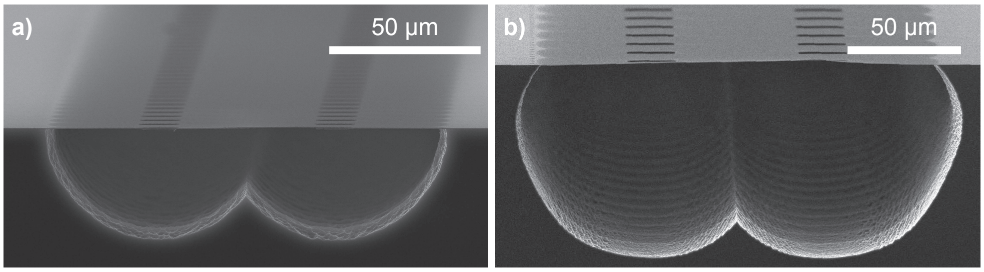

Fig. 6. Etch profiles: device layers under-etched in **a)** XeF_2 and **b)** SF_6 plasma.

The passivation requirements in the two methods were also found to differ. Both methods were tested with and without bottom passivation and gave different under-etching selectivities, and the complete stack of layers used in the processing in all samples is listed in Table 2. This can be explained by the same mechanisms responsible for the dissimilar etch profiles. In XeF_2, tantala cannot be under-etched directly and a bottom passivation with a more resistant material, ideally Al_2O_3, is necessary (Fig. 4). XeF_2 molecules have enough time to diffuse to the tantala backside surface because silicon etching is limited by a physisorbed layer. In contrast, SF_6 plasma facilitates direct under-etching of tantala as evidenced by sample A3. Most of reactive species entering through an opening are immediately spent on the silicon etching and do not reach the device layer. Tantala is still slowly etched from the backside but this effect is not significant and does not impair for the required membrane aspect ratio. Al_2O_3 passivation can be again used if the tantala over-etching is not affordable.

Table 2. Summary of the deposited layers and waveguide patterning on samples A1–A3.

Sample	Ta_2O_5 device layer thickness T	Al_2O_3 passivation layer thickness	SiO_2 adhesion layer thickness	Patterned waveguides
A1	350 nm	30 nm	30 nm	Yes
A2	400 nm	20 nm	20 nm	Yes
A3	400 nm	—	—	No

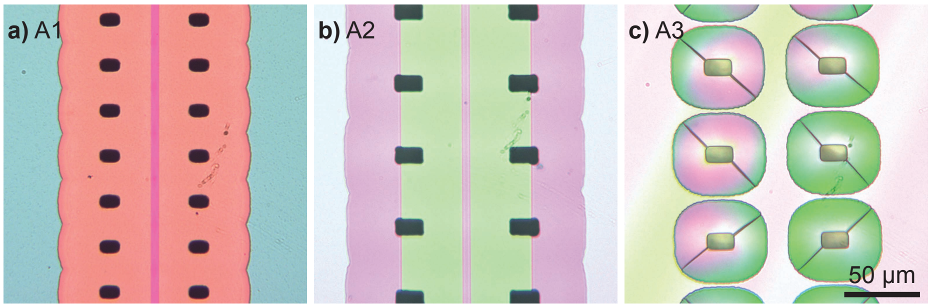

Fig. 7. Optical microscope images of the fabricated membranes. **a)** Sample A1 under-etched in XeF_2 with SiO_2 and Al_2O_3 layer stack for passivation. **b)** Sample A2 under-etched in SF_6 plasma after the TMAH treatment, which removed the SiO_2/Al_2O_3 layer stack. The shallow etching, which defines the waveguides, only extends to the openings. **c)** Sample A3 also under-etched in SF_6 plasma. The scale bar in **(c)** applies to all images.

The top side of the device layer can be passivated with a photoresist in XeF_2 processing. In SF_6 plasma, the photoresist is etched, as discussed above, and it can burn due to accumulated heat. Either way can lead to exposing the device layer, which is highly detrimental. In addition, it has been hypothesized that the photoresist contaminates the plasma and the etched surfaces [41]. These issues could be circumvented by using a metal mask, which can be removed by liquid processing.

4.4 Mechanical stability of thin-film membranes

Thin films can develop compressive or tensile stress with respect to the substrate. If the stress magnitude is critical, bending or cracking of the membranes will occur. Deposition processes of samples A1 and A2 produced low-stress films, and their mechanical stability was further tested with a stylus profiler. The membranes were laterally scanned with the stylus with loads of 0.5, 1, and 2 mg without getting damaged. This shows that the mechanical stability is satisfactory for membranes with aspect ratio over 300. Contrarily, sample A3 could not be under-etched because cracks started developing in the layer soon after the processing initiated (Fig. 7c). This was likely caused by a high tensile stress in the layer, which is a consequence of the deposition from a solution.

4.5 Waveguide patterning

Profilometer measurements revealed that the rib shallow etch depth E was about 32 nm in sample A1, close to the targeted 30 nm. The Argon IBM results in partial redeposition of the material [55,56]. The deposits are visible on edges of the waveguides in the profilometer scan in Fig. 8. This can cause local inhomogeneities and thus contribute to propagation loss by scattering. The processing method was therefore changed to RIE in sample A2 where the etched material is chemically transformed into volatile compounds and discharged from the reactor. The shallow reactive etching with CHF_3/O_2 on sample A2 gave approximately 45–50 nm, again matching well to the intended 50 nm etch depth E. In this case, material redeposition was significantly suppressed (Fig. 8).

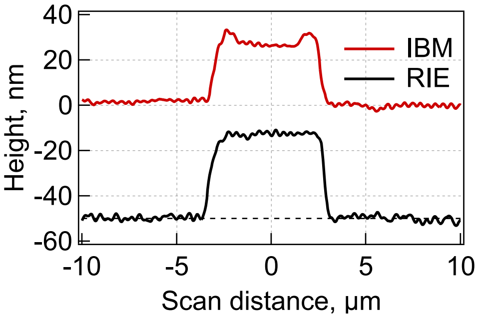

Fig. 8. Stylus profiler scans of waveguides samples A1 (red curve) and A2 (black curve). A1 was patterned via Ar IBM and shows residues of redeposition on the waveguide edges. A2 was patterned via RIE and no redeposition was observed. The downward spike and different levels on left and right in the black curve are profiler measurement artefacts resulting from the plasticity of the membrane. See **Data Files 1 and 2** for underlying data.

5. Application: Suspended Nanophotonic Waveguides

As discussed in detail in the Design section, the principal benefit of the fabricated suspended rib waveguides is their ability to accommodate a strongly vertically delocalized field. In this context, operating the waveguides in TM polarization is beneficial despite the limits of lateral leakage, facilitating remarkably high Γ_{ext} [57] and thus strong light–matter interaction (Fig. 2a). Previously, we experimentally confirmed the high confinement factor of 107 ± 2 % in sample A1 [23]. Note that both A1 and A2 designs lead to a similar external confinement factor, while A1 exhibits less interaction with the core material (and, hence, potentially lower propagation loss due to absorption) at the cost of possibly lower mechanical stability.

The waveguide pathlength L represents another mean of controlling the interaction with analyte as can be understood from a generalized Lambert–Beer law

$$I = I_0 \exp[-\alpha\Gamma L]$$

with α being the bulk absorption coefficient. The possible pathlength that can be achieved is principally limited by the propagation loss. This in turn comes from intrinsic material absorption, impurity and residual absorption, scattering, and lateral leakage.

Propagation loss of waveguides on sample A1 were characterized from out-of-plane light scattering because the scattered signal was sufficient to quantify the decay. We retrieved loss of 6.8 dB cm^{-1} at 2566 nm. This figure was achieved after annealing the sample at 600 °C for 3 h. Without annealing, the loss was approximately 12 dB cm^{-1}. We therefore attribute the relatively high loss to residual water and OH absorption because 2566 nm wavelength coincides with a wing of the water absorption band at 3 µm [5]. Annealing is expected to remove water and improve condensation reactions of adjacent O–H groups [8].

Waveguides in sample A2 did not visibly scatter light and therefore the loss was measured via the cutback method with three different waveguide lengths. The lowest loss of 9.5 dB cm^{-1} was achieved with 5.1 µm wide waveguides (see Table 3). The increase in loss for both narrower and wider waveguides is most likely due to the lateral leakage. No annealing was performed with sample A2 and the relatively high loss can be a result of both absence of the annealing step and stronger light confinement in the core material. Nevertheless, the evaporated layers are expected to have a higher packing density than the sputtered layers, thus leaving less space for water. Lower losses are expected after annealing, which needs to be performed prior to membrane processing in order not to damage the membranes.

The TM mode of the fabricated waveguides has several characteristics that remind of a free space beam. The field is strongly delocalized (see inset of Fig. 2d), leading to a low effective index of approximately 1.1 for a 400 nm device layer. Consequently, both the facet reflections and the coupling losses in an end-fire configuration are remarkably low. With our characterization setup and the coupling objective lens with NA = 0.56, we get the minimum coupling spot of 8–10 µm in diameter, which corresponds to a theoretical 1.8–2.8 dB in-coupling loss for a 4.7 µm wide waveguide (Fig. 2d). The influence of the rib width W between 4.9 and 5.7 µm on the coupling loss is negligible. The experimental coupling loss per facet values for the samples A1 and A2 are between 2.3 and 2.7 dB, which is in a good agreement with the theory.

Table 3: Waveguide dimensions and loss measurement at 2566 nm. The dimensions were measured with a scanning electron microscope (Zeiss Zigma). See Data Files 3 and 4 for loss measurement underlying data.

Sample	Width [µm]		Loss		Reference
	Nominal	Measured	Propagation [dB cm^{-1}]	Coupling [dB]	
A1	4.5	4.8	6.8	2.3	Our group in [23]
A2	4.9	4.6	12.1	2.3	This work
A2	5.3	5.1	9.5	2.7	This work
A2	5.7	5.5	14.1	–	This work

6. Conclusion

We demonstrated two dry-etch methods for the under-etching of tantala membranes for the purpose of fabricating air-suspended optical waveguides. There are significant differences in the etching results. With an Si to Ta_2O_5 selectivity of 210 ± 40, XeF_2 does not allow direct processing of tantala and a bottom passivation layer with more resistant material (Al_2O_3) is necessary. In contrast, SF_6 plasma facilitates direct under-etching of tantala with no need for passivation. However, the different selectivities during the under-etching result from etch rate limiting mechanisms rather than from difference in actual material selectivities: Reactive species are depleted faster in SF_6 plasma than in XeF_2, and probabilities to reach the tantala layer backside are therefore different. Photoresist was found to be a convenient top side passivation against XeF_2 but not against SF_6 plasma. This is due to photoresist etching in the plasma and residues on the membrane backside, which were linked to fluorocarbon contamination. A hard mask, such as chromium, would be more suitable. The relaxed requirements on the backside passivation in SF_6 plasma makes the process appealing for use on other dielectrics such as TiO_2, or Si_3N_4, while Al_2O_3 can be processed either way. The resulting etch profiles (Fig. 6) favor SF_6 plasma processing, which leads to more pronounced separation between the device layer and the substrate. This is beneficial to preventing the delocalized guided light from leaking into the substrate.

Stylus profiler loading and wet processing of the membranes further demonstrated that fabricated membranes with an aspect ratio of up to 400 are mechanically stable. However, thin films with high tensile stress such as films deposited from wet solutions cannot be directly processed into membranes because they start cracking in an early phase of the under-etching process. The films thus need to be prepared low-stress, while annealing can potentially alleviate compressive stress [34].

We further demonstrated that the processed membranes can be successfully utilized as a backbone for air-suspended rib waveguides. This waveguide design is very attractive for optical sensing applications, especially in the MIR molecular fingerprint region. Waveguiding was studied at 2566 nm, where, e.g., trace amounts of acetylene and HF gas can be detected. In the configuration with TM polarization, we demonstrated several advantages of this waveguide: i) Strong light–matter interaction of up to 109 % as compared to a free-space beam; ii) reduced requirements for material transparency due to weak light interaction with the waveguide core material, nominally 14 % for T = 400 nm and 9 % for T = 350 nm; and iii) low coupling loss in an end-fire configuration down to 2.3 dB per facet without any tapers. Nevertheless, minimum experimental propagation losses are still rather high, 6.8 dB cm^{-1}, which likely comes from water and OH absorption in the tantala material. The material transparency needs to be improved to allow longer pathlengths and thus better interaction for sensitivity-critical applications such as trace gas spectroscopy. Future work will thus focus on reducing the material absorption and new cross-sectional designs suppressing the lateral leakage, while making use of the versatile SF_6 plasma etching process.

Apart from sensing, the membrane waveguides with extended evanescent field can be tailored for a variety of other applications such as chip-based microscopy where the evanescent field is used to excite biological samples on the waveguide surface at visible wavelengths [58,59]. Here, penetration depths of 100–200 nm provide an ideal optical cross-section for high contrast images. The membrane processing is also applicable beyond nanophotonics. Thin membranes are found in various MEMS devices like thermal sensors [60], optical filters [61], or pressure sensors [62]. Similar processing has been used for wafer-scale preparation of transmission electron microscope specimens [63] and for constructing cages for DNA trapping [64].

Funding. This work was supported by the Research Council of Norway through project no. 262608 and through the Norwegian Micro- and Nano-Fabrication Facility, NorFab (project no. 295864), the European Research Council (grant no. 758973), the Tromsø Research Foundation (project ID 17_SG_JJ), the Norwegian PhD Network on Nanotechnology for Microsystems (contract no. 221860/F60), and “The Future Photonics Hub” (EPSRC grant EP/N00762X/1).

Acknowledgements. The authors thank to Jens Høvik, Jong Wook Noh, and Mukesh Yadav (NTNU, Trondheim, Norway) for help with processing, Vinita Mittal (ORC, Southampton, UK) for conducting the XeF_2 etching and Jan Torgersen (NTNU, Trondheim, Norway) for helpful discussions within material processing.

Disclosures. The authors declare no conflicts of interest.

Data availability. Data underlying the results presented in this paper are available in Data Files 1–4.

References

1. R. Soref, "Mid-infrared photonics in silicon and germanium," Nat. Photonics **4**, 495–497 (2010).
2. T. Schädle and B. Mizaikoff, "Mid-Infrared Waveguides: A Perspective," Appl. Spectrosc. **70**, 1625–1638 (2016).
3. H. Lin, Z. Luo, T. Gu, L. C. Kimerling, K. Wada, A. Agarwal, and J. Hu, "Mid-infrared integrated photonics on silicon: a perspective," Nanophotonics **7**, 393–420 (2017).
4. D. Marris-Morini, V. Vakarin, J. M. Ramirez, Q. Liu, A. Ballabio, J. Frigerio, M. Montesinos, C. Alonso-Ramos, X. Le Roux, S. Serna, D. Benedikovic, D. Chrastina, L. Vivien, and G. Isella, "Germanium-based integrated photonics from near- to mid-infrared applications," Nanophotonics **7**, 1781–1793 (2018).
5. H. D. Downing and D. Williams, "Optical constants of water in the infrared," J. Geophys. Res. **80**, 1656–1661 (1975).
6. E. Franke, C. L. Trimble, M. J. DeVries, J. A. Woollam, M. Schubert, and F. Frost, "Dielectric function of amorphous tantalum oxide from the far infrared to the deep ultraviolet spectral region measured by spectroscopic ellipsometry," J. Appl. Phys. **88**, 5166–5174 (2000).

7. T. J. Bright, J. I. Watjen, Z. M. Zhang, C. Muratore, A. A. Voevodin, D. I. Koukis, D. B. Tanner, and D. J. Arenas, "Infrared optical properties of amorphous and nanocrystalline Ta_2O_5 thin films," J. Appl. Phys. **114**, 083515 (2013).
8. Z. Yongheng and G. Zhenan, "The study of removing hydroxyl from silica glass," J. Non-Cryst. Solids **352**, 4030–4033 (2006).
9. G. Beshkov, S. Lei, V. Lazarova, N. Nedev, and S. S. Georgiev, "IR and Raman absorption spectroscopic studies of APCVD, LPCVD and PECVD thin SiN films," Vacuum **69**, 301–305 (2002).
10. S. C. Mao, S. H. Tao, Y. L. Xu, X. W. Sun, M. B. Yu, G. Q. Lo, and D. L. Kwong, "Low propagation loss SiN optical waveguide prepared by optimal low-hydrogen module," Opt. Express **16**, 20809 (2008).
11. X. Wu, J. Feng, X. Liu, and H. Zeng, "Effects of rapid thermal annealing on aluminum nitride waveguides," Opt. Mater. Express **10**, 3073 (2020).
12. S. A. Miller, M. Yu, X. Ji, A. G. Griffith, J. Cardenas, A. L. Gaeta, and M. Lipson, "Low-loss silicon platform for broadband mid-infrared photonics," Optica **4**, 707 (2017).
13. Z. Cheng, X. Chen, C. Y. Wong, K. Xu, and H. K. Tsang, "Mid-infrared Suspended Membrane Waveguide and Ring Resonator on Silicon-on-Insulator," IEEE Photonics J. **4**, 1510–1519 (2012).
14. J. S. Penades, A. Ortega-Moñux, M. Nedeljkovic, J. G. Wangüemert-Pérez, R. Halir, A. Z. Khokhar, C. Alonso-Ramos, Z. Qu, I. Molina-Fernández, P. Cheben, and G. Z. Mashanovich, "Suspended silicon mid-infrared waveguide devices with subwavelength grating metamaterial cladding," Opt. Express **24**, 22908 (2016).
15. J. S. Penadés, A. Sánchez-Postigo, M. Nedeljkovic, A. Ortega-Moñux, J. G. Wangüemert-Pérez, Y. Xu, R. Halir, Z. Qu, A. Z. Khokhar, A. Osman, W. Cao, C. G. Littlejohns, P. Cheben, I. Molina-Fernández, and G. Z. Mashanovich, "Suspended silicon waveguides for long-wave infrared wavelengths," Opt. Lett. **43**, 795–798 (2018).
16. W. Zhou, Z. Cheng, X. Wu, X. Sun, and H. K. Tsang, "Fully suspended slot waveguide platform," J. Appl. Phys. **123**, 063103 (2018).
17. T.-H. Xiao, Z. Zhao, W. Zhou, C.-Y. Chang, S. Y. Set, M. Takenaka, H. K. Tsang, Z. Cheng, and K. Goda, "Mid-infrared high-Q germanium microring resonator," Opt. Lett. **43**, 2885 (2018).
18. A. Osman, M. Nedeljkovic, J. Soler Penades, Y. Wu, Z. Qu, A. Z. Khokhar, K. Debnath, and G. Z. Mashanovich, "Suspended low-loss germanium waveguides for the longwave infrared," Opt. Lett. **43**, 5997 (2018).
19. A. Abdou, P. Panduranga, J. Richter, E. L. H. Thomas, S. Mandal, O. A. Williams, J. Witzens, and M. P. Nezhad, "Air-clad suspended nanocrystalline diamond ridge waveguides," Opt. Express **26**, 13883–13890 (2018).
20. T. J. Kippenberg, J. Kalkman, A. Polman, and K. J. Vahala, "Demonstration of an erbium-doped microdisk laser on a silicon chip," Phys. Rev. A **74**, (2006).
21. S. Sridaran and S. A. Bhave, "Nanophotonic devices on thin buried oxide Silicon-On-Insulator substrates," Opt. Express **18**, 3850 (2010).
22. N. Nader, A. Kowligy, J. Chiles, E. J. Stanton, H. Timmers, A. J. Lind, F. C. Cruz, D. M. B. Lesko, K. A. Briggman, S. W. Nam, S. A. Diddams, and R. P. Mirin, "Infrared frequency comb generation and spectroscopy with suspended silicon nanophotonic waveguides," Optica **6**, 1269 (2019).
23. M. Vlk, A. Datta, S. Alberti, H. D. Yallew, V. Mittal, G. S. Murugan, and J. Jágerská, "Extraordinary evanescent field confinement waveguide sensor for mid-infrared trace gas spectroscopy," Light Sci. Appl. **10**, 26 (2021).
24. T. D. Visser, H. Blok, B. Demeulenaere, and D. Lenstra, "Confinement factors and gain in optical amplifiers," IEEE J. Quantum Electron. **33**, 1763–1766 (1997).
25. J. T. Robinson, K. Preston, O. Painter, and M. Lipson, "First-principle derivation of gain in high-index-contrast waveguides," Opt. Express **16**, 16659–16669 (2008).
26. F. Ottonello-Briano, C. Errando-Herranz, H. Rödjegård, H. Martin, H. Sohlström, and K. B. Gylfason, "Carbon dioxide absorption spectroscopy with a mid-infrared silicon photonic waveguide," Opt. Lett. **45**, 109 (2020).
27. G. J. Veldhuis, O. Parriaux, H. J. W. M. Hoekstra, and P. V. Lambeck, "Sensitivity enhancement in evanescent optical waveguide sensors," J. Light. Technol. **18**, 677–682 (2000).
28. M. A. Webster, R. M. Pafchek, A. Mitchell, and T. L. Koch, "Width Dependence of Inherent TM-Mode Lateral Leakage Loss in Silicon-On-Insulator Ridge Waveguides," IEEE Photonics Technol. Lett. **19**, 429–431 (2007).
29. F. Tsige Dullo, J.-C. Tinguely, S. Andre Solbo, and O. G. Helleso, "Single-Mode Limit and Bending Losses for Shallow Rib Si3N4 Waveguides," IEEE Photonics J. **7**, 1–11 (2015).
30. C. Chaneliere, J. L. Autran, R. A. B. Devine, and B. Balland, "Tantalum pentoxide (Ta_2O_5) thin films for advanced dielectric applications," Mater. Sci. Eng. R Rep. **22**, 269–322 (1998).
31. W. M. Paulson, F. S. Hickernell, and R. L. Davis, "Effects of deposition parameters on optical loss for rf-sputtered Ta_2O_5 and Si_3N_4 waveguides," J. Vac. Sci. Technol. **16**, 307–310 (1979).
32. M. F. A. Muttalib, R. Y. Chen, S. J. Pearce, and M. D. B. Charlton, "Anisotropic Ta_2O_5 waveguide etching using inductively coupled plasma etching," J. Vac. Sci. Technol. Vac. Surf. Films **32**, 041304 (2014).
33. A. Z. Subramanian, G. S. Murugan, M. N. Zervas, and J. S. Wilkinson, "Spectroscopy, Modeling, and Performance of Erbium-Doped Ta_2O_5 Waveguide Amplifiers," J. Light. Technol. **30**, 1455–1462 (2012).
34. C. Christensen, R. de Reus, and S. Bouwstra, "Tantalum oxide thin films as protective coatings for sensors," J. Micromechanics Microengineering **9**, 113 (1999).
35. D. Briand, G. Mondin, S. Jenny, P. D. van der Wal, S. Jeanneret, N. F. de Rooij, O. Banakh, and H. Keppner, "Metallo-organic low-pressure chemical vapor deposition of Ta_2O_5 using $TaC_{12}H_{30}O_5N$ as precursor for batch fabrication of microsystems," Thin Solid Films **493**, 6–12 (2005).

36. D. Saygin-Hinczewski, K. Koc, I. Sorar, M. Hinczewski, F. Z. Tepehan, and G. G. Tepehan, "Optical and structural properties of Ta_2O_5–CeO_2 thin films," Sol. Energy Mater. Sol. Cells **91**, 1726–1732 (2007).
37. G. Li, T. Maruyama, and K. Iiyama, "Low-propagation-loss Ta_2O_5 optical waveguides on silica substrate," Jpn. J. Appl. Phys. **53**, 04EG12 (2014).
38. M. F. A. Muttalib, R. Y. Chen, S. J. Pearce, and M. D. B. Charlton, "Optimization of reactive-ion etching (RIE) parameters for fabrication of tantalum pentoxide (Ta_2O_5) waveguide using Taguchi method," EPJ Web Conf. **162**, 01003 (2017).
39. K. Sugano and O. Tabata, "Reduction of surface roughness and aperture size effect for etching of Si with XeF_2," J. Micromechanics Microengineering **12**, 911–916 (2002).
40. S. Frederico, C. Hibert, R. Fritschi, P. Fluckiger, P. Renaud, and A. M. Ionescu, "Silicon sacrificial layer dry etching (SSLDE) for free-standing RF MEMS architectures," in *The Sixteenth Annual International Conference on Micro Electro Mechanical Systems, 2003. MEMS-03 Kyoto. IEEE* (IEEE, 2003), pp. 570–573.
41. K. P. Larsen, D. H. Petersen, and O. Hansen, "Study of the Roughness in a Photoresist Masked, Isotropic, SF_6-Based ICP Silicon Etch," J. Electrochem. Soc. **153**, G1051 (2006).
42. T. Zhu, P. Argyrakis, E. Mastropaolo, K. K. Lee, and R. Cheung, "Dry etch release processes for micromachining applications," J. Vac. Sci. Technol. B Microelectron. Nanometer Struct. **25**, 2553 (2007).
43. P. Panduranga, A. Abdou, Z. Ren, R. H. Pedersen, and M. P. Nezhad, "Isotropic silicon etch characteristics in a purely inductively coupled SF_6 plasma," J. Vac. Sci. Technol. B **37**, 061206 (2019).
44. H. F. Winters and J. W. Coburn, "The etching of silicon with XeF_2 vapor," Appl. Phys. Lett. **34**, 70–73 (1979).
45. D. Xu, B. Xiong, G. Wu, Y. Wang, X. Sun, and Y. Wang, "Isotropic Silicon Etching With XeF_2 Gas for Wafer-Level Micromachining Applications," J. Microelectromechanical Syst. **21**, 1436–1444 (2012).
46. D. E. Ibbotson, D. L. Flamm, J. A. Mucha, and V. M. Donnelly, "Comparison of XeF_2 and F-atom reactions with Si and SiO_2," Appl. Phys. Lett. **44**, 1129–1131 (1984).
47. M. M. Winterkorn, A. L. Dadlani, Y. Kim, J. Provine, and F. B. Prinz, "ETCH “sandbox”: Controlled release dimensions through atomic layer deposition etch stop with trench refill and polish," in *2015 Transducers - 2015 18th International Conference on Solid-State Sensors, Actuators and Microsystems (TRANSDUCERS)* (IEEE, 2015), pp. 2272–2275.
48. R. d’Agostino and D. L. Flamm, "Plasma etching of Si and SiO_2 in SF_6–O_2 mixtures," J. Appl. Phys. **52**, 162–167 (1981).
49. D. E. Ibbotson, J. A. Mucha, D. L. Flamm, and J. M. Cook, "Plasmaless dry etching of silicon with fluorine-containing compounds," J. Appl. Phys. **56**, 2939–2942 (1984).
50. P. B. Chu, J. T. Chen, R. Yeh, G. Lin, J. C. P. Huang, B. A. Warneke, and S. J. Pister, "Controlled pulse-etching with xenon difluoride," in *Proceedings of International Solid State Sensors and Actuators Conference (Transducers ’97)* (IEEE, 1997), Vol. 1, pp. 665–668.
51. K. R. Williams, K. Gupta, and M. Wasilik, "Etch rates for micromachining processing-Part II," J. Microelectromechanical Syst. **12**, 761–778 (2003).
52. J.-F. Veyan, M. D. Halls, S. Rangan, D. Aureau, X.-M. Yan, and Y. J. Chabal, "XeF_2-induced removal of SiO_2 near Si surfaces at 300 K: An unexpected proximity effect.," J. Appl. Phys. **108**, 114914 (2010).
53. S. Leopold, C. Kremin, A. Ulbrich, S. Krischok, and M. Hoffmann, "Formation of silicon grass: Nanomasking by carbon clusters in cyclic deep reactive ion etching," J. Vac. Sci. Technol. B Nanotechnol. Microelectron. Mater. Process. Meas. Phenom. **29**, 011002 (2011).
54. R. A. Gottscho, "Microscopic uniformity in plasma etching," J. Vac. Sci. Technol. B Microelectron. Nanometer Struct. **10**, 2133 (1992).
55. R. Smith, M. Tagg, and J. Walls, "Deterministic models of ion erosion, reflection and redeposition," Vacuum **34**, 175–180 (1984).
56. K. P. Müller and J. Pelka, "Redeposition in ion milling," Microelectron. Eng. **7**, 91–101 (1987).
57. G. J. Veldhuis, O. Parriaux, H. J. W. M. Hoekstra, and P. V. Lambeck, "Sensitivity enhancement in evanescent optical waveguide sensors," J. Light. Technol. **18**, 677–682 (2000).
58. J.-C. Tinguely, Ø. I. Helle, and B. S. Ahluwalia, "Silicon nitride waveguide platform for fluorescence microscopy of living cells," Opt. Express **25**, 27678–27690 (2017).
59. Ø. I. Helle, F. T. Dullo, M. Lahrberg, J.-C. Tinguely, O. G. Hellesø, and B. S. Ahluwalia, "Structured illumination microscopy using a photonic chip," Nat. Photonics **14**, 431–438 (2020).
60. P. M. Sarro, A. W. van Herwaarden, and W. van der Vlist, "A silicon-silicon nitride membrane fabrication process for smart thermal sensors," Sens. Actuators Phys. **42**, 666–671 (1994).
61. M. Ghaderi and R. F. Wolffenbuttel, "Design and fabrication of ultrathin silicon-nitride membranes for use in UV-visible airgap-based MEMS optical filters," J. Phys. Conf. Ser. **757**, 012032 (2016).
62. S. Lorenzo and O. Solgaard, "Optical Fiber-Facet Multiplexed Monolithic Silicon Pressure Sensors," IEEE Sens. J. **20**, 10598–10606 (2020).
63. T. S. English, J. Provine, A. F. Marshall, A. L. Koh, and T. W. Kenny, "Parallel preparation of plan-view transmission electron microscopy specimens by vapor-phase etching with integrated etch stops," Ultramicroscopy **166**, 39–47 (2016).
64. X. Liu, M. M. Skanata, and D. Stein, "Entropic cages for trapping DNA near a nanopore," Nat. Commun. **6**, 6222 (2015).

A

Variation Theorem for Dielectric Waveguides

Section 2.1.3 introduced how the light–matter interaction in optical waveguides is quantified. The rigorous derivation of the expression for confinement factor is provided therein based on (110; 34). It was also discussed that different approach appeared in (37), where the starting point was a variation theorem for dielectric waveguides. The purpose of this appendix is to show the origin of this theorem following (111).

The theorem follows directly from Maxwell equations for monochromatic fields [ref maxwell]. We outline the approach on equation (15). To obtain the variation theorem, we first take a differential of [ref maxewell for E] and form a dot product with $\mathbf{H}^*$

$$(\nabla \times \delta \mathbf{E}) \cdot \mathbf{H}^* = -j\delta(\omega\mu)\mathbf{H} \cdot \mathbf{H}^* - j\omega\mu(\delta \mathbf{H}) \cdot \mathbf{H}^*. \tag{A.1}$$

We can proceed with a small leap. $\mathbf{H}^*$ in the last term gets substituted from [ref maxwell for H], and the same steps need to be followed for [ref maxwell for H] to get a similar expression. By subtracting the two resulting equations, that is A.1 and its analogue for $\mathbf{H}$, and using the vector product identity

$$\nabla \cdot (\mathbf{A} \times \mathbf{B}) = \mathbf{B} \cdot (\nabla \times \mathbf{A}) - \mathbf{A} \cdot (\nabla \times \mathbf{B}), \tag{A.2}$$

we get the variation theorem

$$\nabla \cdot (\mathbf{E}^* \times \delta \mathbf{H} + \delta \mathbf{E} \times \mathbf{H}^*) = -j\left[\delta(\omega\epsilon)|\mathbf{E}|^2 + \delta(\omega\mu)|\mathbf{H}|^2\right]. \tag{A.3}$$

This theorem relates variations of electric and magnetic fields to variations in ω, ϵ, and μ, that is to changes in material properties.

Variations in the propagation constant β can be related to the variations in ϵ, which in turn reflects the material loss. Taking the solutions 2.18, the variations of **E** and **H** are

$$\{\delta\mathbf{E}, \delta\mathbf{H}\} = (\{\delta\tilde{\mathbf{E}}, \delta\tilde{\mathbf{H}}\} - jz\delta\beta\{\tilde{\mathbf{E}}, \tilde{\mathbf{H}}\}) \exp[-j\beta z]. \tag{A.4}$$

We insert these solutions into A.3 and obtain

$$\nabla_\perp \cdot \mathbf{g} - j\delta\beta S_z = -j[\delta(\omega\epsilon)|\tilde{\mathbf{E}}|^2 + \delta(\omega\mu)|\tilde{\mathbf{H}}|^2], \tag{A.5}$$

where $\nabla_\perp$ is the transverse differential operator,

$$\mathbf{S} = \tilde{\mathbf{E}} \times \tilde{\mathbf{H}}^* + \tilde{\mathbf{E}}^* \times \tilde{\mathbf{H}} \tag{A.6}$$

is the time-averaged Poynting vector, and

$$\mathbf{g} = \tilde{\mathbf{E}}^* \times \delta\tilde{\mathbf{H}} + \delta\tilde{\mathbf{E}} \times \tilde{\mathbf{H}}^* - j\delta\beta z\mathbf{S}. \tag{A.7}$$

Finally, we integrate A.5 over the waveguide cross section. The integral over $\nabla_\perp \cdot \mathbf{g}$ vanishes; A divergence theorem implies that the result is 0 for a guided mode (111). Therefore, we are left with

$$\delta\beta \iint_{-\infty}^{\infty} S_z dxdy = \iint_{-\infty}^{\infty} [\delta(\omega\epsilon)|\tilde{\mathbf{E}}|^2 + \delta(\omega\mu)|\tilde{\mathbf{H}}|^2] dxdy \tag{A.8}$$

Adding a small imaginary part to the refractive index $\Delta n''$, which relates to a change in permittivity as $\Delta\epsilon = (-j2n'\Delta n'' + (\Delta n'')^2)$, we obtain the corresponding variation in the propagation constant

$$\Delta\beta = \frac{2\omega \iint_{-\infty}^{\infty} \Delta\epsilon|\tilde{\mathbf{E}}|^2 dxdy}{\mathrm{Re}\{\iint_{-\infty}^{\infty} (\tilde{\mathbf{E}} \times \tilde{\mathbf{H}}) \cdot \mathbf{e}_z dxdy\}}. \tag{A.9}$$

Equation A.9 is the variation theorem for dielectric waveguides and allows to obtain variations in the propagation constant β from variations in the permittivity ϵ.

B

Confinement Factor Implementation for Lumerical

It was necessary to implement the confinement factor calculation manually in Lumerical. The following script calculates the confinement factor for a selected mode. A filter matrix needs be defined first, to select the area in which the calculate the confinement factor. This is conveniently done based on a refractive index value.

```
##############################################################
# This script finds the confinement factor of a mode.
#=============================================================


#=============================================================
# your input parameters
#=============================================================


# Enter refractive index value of the medium in which
# you want to calculate the confinement factor; e.g. 1 for air.
index_val = 1;
# select your mode
mode = "mode1";



#=============================================================
```

```
# create a binary mask to define c.f. region
#================================================================

# get the actual index data
index_x = real(pinch(getdata("FDE::data::material","index_x")));
eps_mat = index_x * index_x * eps0;
# retrieve the matrix size
x = pinch(getdata("FDE::data::material","x"));
nx = length(x);
y = pinch(getdata("FDE::data::material","y"));
ny = length(y);
# define the mask matrix
filter = matrix(nx,ny);
# define the mask; put values into mask matrices
rel_dif = 0.01; # something like an error for the ref. index
index_val_mat = ones(nx,ny)*index_val;
filter(1:nx,1:ny) =
    almostequal(pinch(index_x), index_val_mat, rel_dif);

# clear unnecessary data
clear(index_x, nx, ny, rel_dif, index_val_mat);


#================================================================
# calculate the confinement factor
#================================================================

# retrieve the field data of a given mode
Ex = pinch(getdata("FDE::data::"+mode,"Ex"));
Ey = pinch(getdata("FDE::data::"+mode,"Ey"));
Ez = pinch(getdata("FDE::data::"+mode,"Ez"));
Hx = pinch(getdata("FDE::data::"+mode,"Hx"));
Hy = pinch(getdata("FDE::data::"+mode,"Hy"));
# calculate Pz and |E| squared
Pz = (Ex*conj(Hy) - Ey*conj(Hx));
# factor 0.5 is important due to complex fields
Enorm2 = Ex*conj(Ex) + Ey*conj(Ey) + Ez*conj(Ez);
Enorm = sqrt(Enorm2);
```

```
# apply a mask to |E| squared
Pz_f = Pz*filter;
Enorm2_f = Enorm2*filter;
Enorm_f = Enorm*filter;

# confinement factor calculation and acquisition
intP = integrate(real(Pz), [1,2], x, y);
intP_f = integrate(real(Pz_f), [1,2], x, y);
intE = integrate(real(Enorm), [1,2], x, y);
intE_f = integrate(real(Enorm_f), [1,2], x, y);
intE2 = integrate(real(Enorm2), [1,2], x, y);
intE2_f = integrate(real(Enorm2_f), [1,2], x, y);
intepsE2 = integrate(real(eps_mat*Enorm2), [1,2], x, y);
intepsE2_f = integrate(real(eps_mat*Enorm2_f), [1,2], x, y);

CF = c * eps0 * index_val * intE2_f / intP;
Pfrac = intP_f/intP;
Efrac = intE_f/intE;
E2frac = intE2_f/intE2;
epsE2frac = intepsE2_f/intepsE2;
ng = c * intepsE2 / intP;



# clear unnecessary data
clear(index_val, x, y, Ex, Ey, Ez, Hx, Hy, Pz,
    Enorm2, Enorm2_f, intP, intE_f);

?mode + "␣confinement␣factor␣is␣" + num2str(CF*100) + "%";
```

/C

Silicon Slot Waveguide Model

Slot waveguides have become popular for their strong field localisation in the low refractive index slot as measured by the confinement factor. This localisation occurs when the light polarisation is perpendicular to the slot as shown earlier in Fig. 2.5c. Slots can be horizontal, which is convenient for devices with gain (37), and they need to be defined by deposition methods (112). Vertical slots are patterned into an existing device layer, and they are suited better for gas sensing because the slot is primarily filled with air. Indeed, slot waveguides have been used for methane spectroscopy (82) and label-free sensing with a surface functionalisation (113; 80). A cavity based on an air-slot waveguide has been also employed for refractive index sensing (81).

Silicon-on-sapphire platform (114), TiO_2 (99), chalcogenide (115), and SOI (116; 49), have all been used for slot waveguide fabrication, and some slot waveguides have been made free-standing(117; 58). Moreover, a polymer filling in the slot has been used for making temperature-insensitive ring resonators (116).

As a part if this work, slot waveguides were considered for CH_4 detection around 3250 nm. Fig. C.1 shows a waveguide schematics and a TE_{00} mode field distribution in the waveguide. It was discussed in section 2.1.2 that the TM polarisation has no particularly useful properties and hence the choice of the TE polarisation is straightforward. The waveguide can be used with direct exposure to air or with polymer claddings on top. Polymers often allow the small molecules of methane to diffuse in and increase the concentration due to lower mobility. They can also serve as a matrix for specific cage-like molecules known as cryptophanes, which further increase the concentration (118).

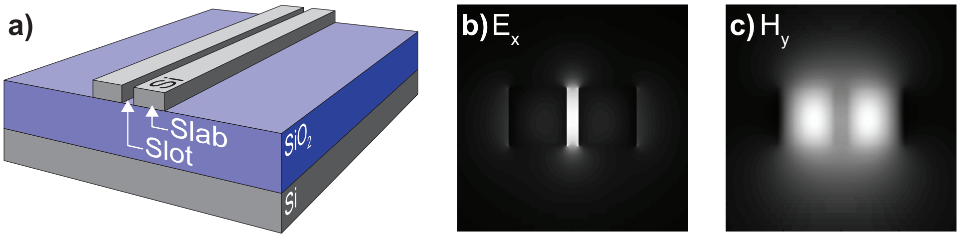

Figure C.1: Schematics of the studied slot waveguide **(a)**, and distributions of the field components E_x **(b)** and H_y **(c)** at 3250 nm wavelength. The device layer was set to 500 nm thickness, slabs were 500 nm wide and the slot was 100 nm.

The waveguide was modelled with FIMMWAVE and mainly the confinement factor and propagation losses were studied. The refractive indices were set to 3.43 for silicon and 1.43 for silica, while air and polymer refractive indices were 1 and 1.4 respectively. The device layer thickness was fixed as 500 nm and silica cladding as 3 µm,[1] and slab/slot widths were variables. Propagation loss components modelled in this study were the substrate leakage and a material absorption in silica. The former was simulated by including a 50 nm thin layer of silicon below the BOx, to account for the Si–SiO_2 interface, and followed by a PML medium. The silica absorption was modelled by assigning a $0.15\,\mathrm{cm}^{-1}$ absorption coefficient (119) ($0.65\,\mathrm{dB\,cm}^{-1}$) to the bottom cladding.

Results from the model are displayed in Fig. C.2. One of the requirements on waveguides for absorption spectroscopy is to support only a single mode (see the attached Papers for a discussion, particularly III). The SM condition is not shown explicitly, but the plots of the effective index of the TE_{00} mode only show data for an SM waveguide. Wider slabs than those shown were supporting a TE_{10} mode. The air-exposed waveguide exhibits an additional cut-off for narrow slabs because the effective index drops below the SiO_2 light line. Cladding the top with a polymer evidently shifts the SM condition towards narrower waveguides.

The confinement factor in air or the polymer cladding Γ can reach relatively exceptional values. Air-cladded waveguides show confinement factors over 80 % for 500 nm and no more than 120 nm wide slots. Other configurations also yield high confinement factors, but this is where propagation losses need to be considered, in particular the substrate leakage. Configurations with the highest confinement factors are especially prone to a strong substrate leakage. This can be mitigated by using a thicker silica cladding, which can, however, become costly due to long oxidation times in SOI wafer production. Including the polymer on top can also decrease the attenuation to affordable levels, say below $1\,\mathrm{dB\,cm}^{-1}$ as captured in Fig. C.2b.

Losses due to the silica absorption were discriminated by modelling the waveguide both with

---

[1] These dimensions are relatively common and they are offered by the CORNERSTONE consortium in their MPWs.

a) Top cladding n = 1

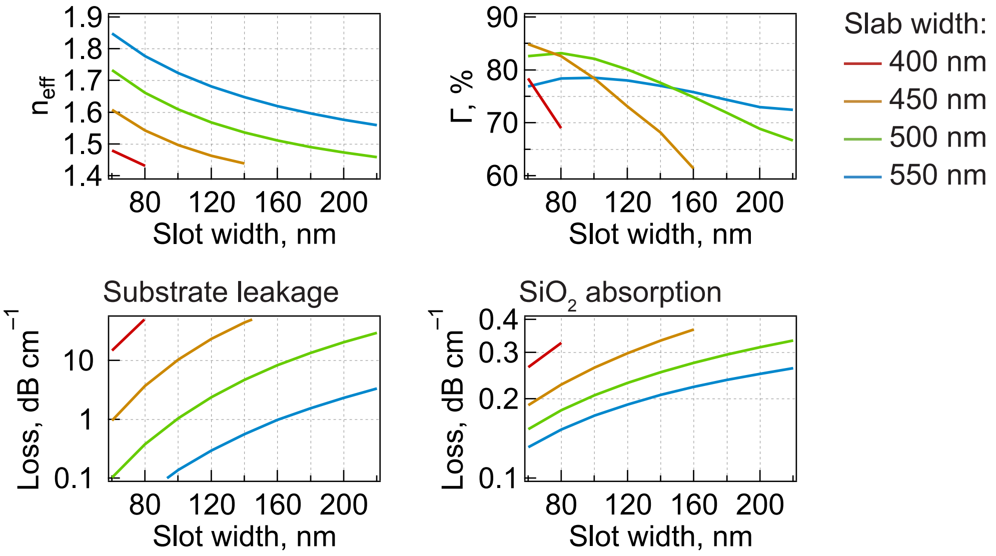

b) Top cladding n = 1.4

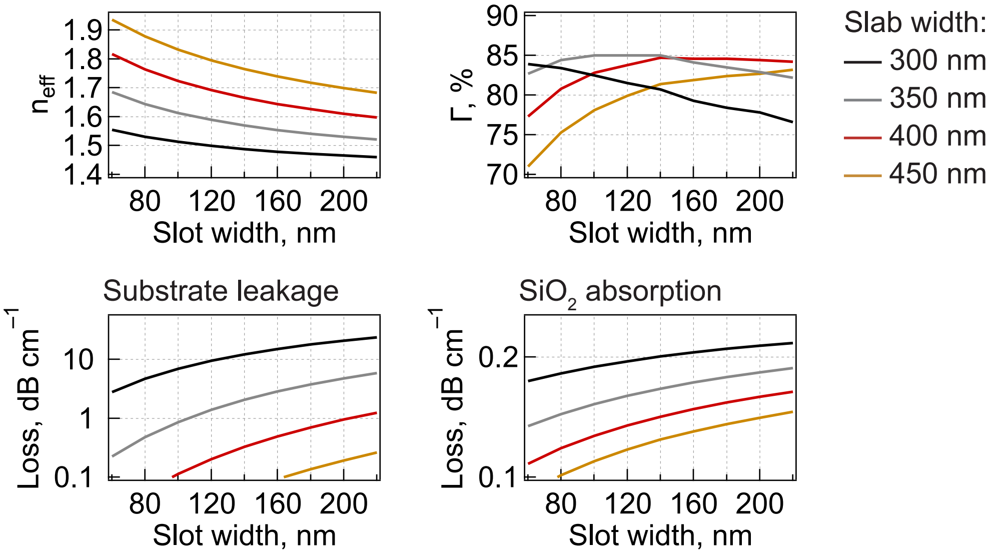

Figure C.2: Results of the Si slot waveguide model in the SOI platform with **a)** air and polymer **b)** top claddings. The graphs show the mode effective index, confinement factor Γ, and propagation losses due to substrate leakage and silica absorption (0.65 dB cm^{-1}).

and without loss assigned to silica and subtracting results for the two models. Compared to the substrate leakage, the silica absorption is of little concern but it can be negatively affected by a lower silica quality and a higher content of hydroxyl groups as discussed in Paper III. Remarkably, Penades *et al.* (49) have measured a total propagation of 1.4(2) dB cm^{-1} at 3.8 µm wavelength with an air-exposed slot waveguide in the same SOI platform considered here.

Finally, the analysis captured in Fig. C.2 allows to select suitable dimensions. Nevertheless, there are practical constraints in the fabrication, which is further a subject of chapter 4. Firstly, the patterning requires lithography with high enough resolution, and for example standard UV lithography does not facilitate the slot dimensions. Waveguides with 78 nm slots have been fabricated with e-beam lithography (49) and deep UV lithography can yield slots down to 100 nm (113). Secondly, the etching process needs to be selective enough in order not to etch in silica, and this requirement grows with aspect ratio of the device layer thickness to the slot width.

This analysis was used for selecting dimensions for fabrication by the CORNERSTENO foundry, and it was further followed by my colleague Henock Demessie Yallew (PhD candidate).

/D

Python Script – Clothoidal Curves for Adibatic Waveguide Connections

This appendix provides a part of the script used to generate the adiabatic connections described in section 3.2.2. Scripting was done in Python 3 and it uses object-based programming, which allowed the code to remain relatively compact while the data manipulation is user-friendly. Late versions of the masks were supported by a library of more than 700 hundreds lines. Therefore, only less trivial parts are provided here. A general class is defined first and then adopted in specific implementations of the MVC up to a third and fourth order in the curvature κ.

```
import numpy as np
from scipy.integrate import quad
from scipy.misc import derivative
from scipy.optimize import fsolve
from scipy.optimize import ridder
from scipy.interpolate import interp1d
from numpy.linalg import norm

## global variables
# overall rotation angle
rot = 0
```

```
# overall derivative increment
# can be overridden either globally or for a specific cases
delta = 0.000001

# rotation functions; good to have it global
def x_rot(x_prime, y_prime):
    return x_prime * np.cos(rot) + y_prime * np.sin(rot)

def y_rot(x_prime, y_prime):
    return - x_prime * np.sin(rot) + y_prime * np.cos(rot)

# class: base functions for the generalized clothoid
class Generalized_clothoid_base:
    def __init__(self, x0, y0, x1, y1, k1, dk1, th1,
    th0=0, dx=delta):
        # attribute the variables to the class
        (self.x0, self.y0, self.x1, self.y1) = (x0, y0, x1, y1)
        (self.k1, self.dk1, self.th1) = (k1, dk1, th1)

        # create new attributes of the class
        self.th0 = th0
        self.a1 = 0
        self.a2 = 0
        self.a3 = 0
        self.a4 = 0
        self.s1 = 0

        self.dx = dx

    # update and override a3
    def f_a3(self):
        self.a3 = ( 12 * (self.th1 - self.th0) / self.s1**4
                  - 8 * self.k1 / self.s1**3
                  + 2 * self.dk1 / self.s1**2
                  - (12/5.0) * self.a4 * self.s1
                  )

    # update and override th0
    def f_th0(self):
```

```
        self.th0 = (self.th1
                    - (2/3.0) * self.k1 * self.s1
                    + (1/6.0) * self.dk1 * self.s1**2
                    - (1/12.0) * self.a3 * self.s1**4
                    - (1/5.0) * self.a4 * self.s1**5
                    )

    # update and override a2 and a1
    def update_parameters(self):
        self.a2 = (- self.k1 / self.s1**2
                   + self.dk1 / self.s1
                   - 2 * self.a3 * self.s1
                   - 3 * self.a4 * self.s1**2
                   )
        self.a1 = (self.dk1
                   - 2 * self.a2 * self.s1
                   - 3 * self.a3 * self.s1**2
                   - 4 * self.a4 * self.s1**3
                   )

    # define the integrands for x and y, they are damn long
    def x_integrand(self, s):
        integrand = np.cos(self.th0
                           + (1/2.0) * self.a1 * s**2
                           + (1/3.0) * self.a2 * s**3
                           + (1/4.0) * self.a3 * s**4
                           + (1/5.0) * self.a4 * s**5
                           )
        return integrand

    def y_integrand(self, s):
        integrand = np.sin(self.th0
                           + (1/2.0) * self.a1 * s**2
                           + (1/3.0) * self.a2 * s**3
                           + (1/4.0) * self.a3 * s**4
                           + (1/5.0) * self.a4 * s**5
                           )
        return integrand
```

```
# calculate x and y for given parameters and bound. conditions
# function 'quad' does not take arrays, iterate manually
def f_x(self, s):
    f_x, err_x = quad(self.x_integrand, 0, s)
    return self.x0 + f_x

def x_prime(self, s):
    if np.ndim(s) == 0:
        x = self.f_x(s)
    else:
        x = []
        for t in s:
            x.append(self.f_x(t))
    return np.asarray(x)

def f_y(self, s):
    f_y, err_y = quad(self.y_integrand, 0, s)
    return self.y0 + f_y

def y_prime(self, s):
    if np.ndim(s) == 0:
        y = self.f_y(s)
    else:
        y = []
        for t in s:
            y.append(self.f_y(t))
    return np.asarray(y)

# x, y coordinates (rotated)
def x(self, s):
    return x_rot(self.x_prime(s), self.y_prime(s))

def y(self, s):
    return y_rot(self.x_prime(s), self.y_prime(s))

# the tangent angle
def tg_angle(self, s):
    arg = self.y_integrand(s) / self.x_integrand(s)
    return np.arctan(arg)
```

```
    # curvature, clothoid
    def kappa(self, s):
        k = (self.a1 * s
             + self.a2 * s**2
             + self.a3 * s**3
             + self.a4 * s**4
             )
        return k

    # curvature derivative, clothoid
    def d_kappa(self, s):
        dk = (self.a1
             + 2 * self.a2 * s
             + 3 * self.a3 * s**2
             + 4 * self.a4 * s**3
             )
        return dk


# class: clothoid with a polynom of 3rd order
#        mainly for inputs / outputs
class Clothoid_order3(Generalized_clothoid_base):
    # __init__() inherited without changes

    # equations for (x, y) with the boundary conditions (x1, y1)
    def eq_xy(self, args):
        self.a3 = args[0]
        self.s1 = args[1]
        self.f_th0()
        self.update_parameters()
        eq_x = self.x(self.s1) - self.x1
        eq_y = self.y(self.s1) - self.y1
        return (eq_x, eq_y)

    # try to solve the equations
    def solve_eq_xy(self, a3_est, s1_est):
        fsolve(self.eq_xy,
               [a3_est, s1_est]
```

```
               )


# class: clothoid with a polynom of 4th order
#        mainly for inputs / outputs
class Clothoid_order4(Generalized_clothoid_base):
    # __init__() inherited without changes

    # equations for (x, y) with the boundary condition (x1, y1)
    def eq_xy(self, args):
        self.a4 = args[0]
        self.s1 = args[1]
        self.f_a3()
        self.update_parameters()
        eq_x = self.x(self.s1) - self.x1
        eq_y = self.y(self.s1) - self.y1
        return (eq_x, eq_y)

    # try to solve the equations
    def solve_eq_xy(self, a4_est, s1_est):
        fsolve(self.eq_xy,
               [a4_est, s1_est]
               )
```

E

Python Script – Offset Paths and Etching Openings

This appendix provides a scripting functions from the library introduced in the previous Appendix. Discussed in section 3.2.3, these functions allows to define offset paths and etching openings, but they are not limited to this application.

```
import numpy as np
from scipy.integrate import quad
from scipy.misc import derivative
from scipy.optimize import fsolve
from scipy.optimize import ridder
from scipy.interpolate import interp1d
from numpy.linalg import norm

## global variables
# overall rotation angle
rot = 0
# overall derivative increment
# can be overridden either globally or for a specific cases
delta = 0.000001

# rotation functions; good to have it global
def x_rot(x_prime, y_prime):
```

```
    return x_prime * np.cos(rot) + y_prime * np.sin(rot)

def y_rot(x_prime, y_prime):
    return - x_prime * np.sin(rot) + y_prime * np.cos(rot)



# function: clone arbitrary curve
# "sep" is a distance from the original curve to the clone
# in the normal direction
def clone(x, y, s, sep, dx=delta):
    # create splines
    f_x = interp1d(s, x, kind='cubic', fill_value='extrapolate')
    f_y = interp1d(s, y, kind='cubic', fill_value='extrapolate')

    sep = sep/1000.0 # convert um into mm

    # path tangent angle
    dx = derivative(f_x, s, dx=dx)
    dy = derivative(f_y, s, dx=dx)
    th = np.arctan(dy / dx)
    for i in range(0, np.size(th)):
        if dx[i] < 0.0:
            th[i] += np.pi
        elif dx[i] == 0.0 and dy[i] < 0.0:
            th[i] = np.arctan(-np.inf)
        elif dx[i] == 0.0 and dy[i] > 0.0:
            th[i] = np.arctan(np.inf)

    # path normal angle
    th += np.pi / 2.0

    # get sideline
    x_off = f_x(s) + sep * np.cos(th)
    y_off = f_y(s) + sep * np.sin(th)

    # rescale path vector
    s_off_total = length(x_off, y_off)
    s_total = length(x, y)
    s_off = s * s_off_total / s_total
```

```
    return x_off, y_off, s_off



# function: measure arbitrary curve length
#           provide reasonable discretisation
def length(x, y):
    s = 0.0

    for i in range(1, np.size(x)):
        arg_x = (x[i] - x[i-1]) ** 2
        arg_y = (y[i] - y[i-1]) ** 2
        s += np.sqrt(arg_x + arg_y)

    return s

def length_plus(x, y):
    s_total = 0.0
    s =[0.0]

    for i in range(1, np.size(x)):
        arg_x = (x[i] - x[i-1]) ** 2
        arg_y = (y[i] - y[i-1]) ** 2
        s_total += np.sqrt(arg_x + arg_y)
        s.append(s_total)

    return s_total, np.asarray(s)



# class: holes
class holes:
    def __init__(self, x, y, s, h2h, h2w, dx=delta):
        self.s = s

        self.x = interp1d(self.s, x, kind='cubic', fill_value='extrapolate')
        self.y = interp1d(self.s, y, kind='cubic', fill_value='extrapolate')

        # enter these two values in um; it will get converted to mm here
        self.h2h = h2h / 1000.0
```

```
        self.h2w = h2w / 1000.0

        self.dx = dx


    # path tangent angle
    def tg_angle(self, s):
        dx = derivative(self.x, s, dx = self.dx)
        dy = derivative(self.y, s, dx = self.dx)
        th = np.arctan(dy / dx)

        for i in range(0, np.size(th)):
            if dx[i] < 0.0:
                th[i] += np.pi
            elif dx[i] == 0.0 and dy[i] < 0.0:
                th[i] = np.arctan(-np.inf)
            elif dx[i] == 0.0 and dy[i] > 0.0:
                th[i] = np.arctan(np.inf)

        return th

    # define sidelines; points
    def origin_left(self, s, sep):
        # normal angle
        self.lth = self.tg_angle(s) + np.pi / 2.0

        self.lx = self.x(s) + sep * np.cos(self.lth)
        self.ly = self.y(s) + sep * np.sin(self.lth)

    def origin_right(self, s, sep):
        # normal angle
        self.rth = self.tg_angle(s) - np.pi / 2.0

        self.rx = self.x(s) + sep * np.cos(self.rth)
        self.ry = self.y(s) + sep * np.sin(self.rth)

    # define sidelines; interpolate the previously obtained points
    def f_left(self, s):
        self.f_lx = interp1d(s, self.lx,
```

```
                             kind='cubic',
                             fill_value='extrapolate')
        self.f_ly = interp1d(s, self.ly,
                             kind='cubic',
                             fill_value='extrapolate')
        self.f_lth = interp1d(s, self.lth,
                             kind='cubic',
                             fill_value='extrapolate')

    def f_right(self, s):
        self.f_rx = interp1d(s, self.rx,
                             kind='cubic',
                             fill_value='extrapolate')
        self.f_ry = interp1d(s, self.ry,
                             kind='cubic',
                             fill_value='extrapolate')
        self.f_rth = interp1d(s, self.rth,
                             kind='cubic',
                             fill_value='extrapolate')

    # these functions are meant to be used in conjunction
    # with the interpolated curves just above this; thus they DEPEND
    def depend_left(self, s):
        self.lx = self.f_lx(s)
        self.ly = self.f_ly(s)
        self.lth = self.f_lth(s)

    def depend_right(self, s):
        self.rx = self.f_rx(s)
        self.ry = self.f_ry(s)
        self.rth = self.f_rth(s)

    # create a vector of hole positions in terms of path s
    def hole_pos(self, s_total):
        s_vector = []
        s_count = 0.0

        while s_count < s_total:
            s_vector.append(s_count)
```

```
            s_count += self.h2h

        return np.asarray(s_vector)

    # drill the holes; define their positions in terms of (x,y)
    def drill(self, Mode='Central', n_points=3000):
        if Mode == 'Central':
            # read the total curve length
            s_total = np.abs(self.s[-1] - self.s[0])
            #print(s_total)

            # first, find positions along waveguide
            # second, determine the hole positions on left and right
            position = self.hole_pos(s_total) - np.abs(self.s[0])
            self.origin_left(position, self.h2w)
            self.origin_right(position, self.h2w)

        elif Mode == 'Side':
            #N = np.linspace(0.0, 1.0, np.size(self.s))

            # create a new s vector; should be quite finely spaced
            s = np.linspace(self.s[0], self.s[-1], n_points)

            # first, points on side to be interpolated
            # second, measure length and acquire
            # positions along lines of holes
            # third, interpolate
            # forth, get positions of holes on their lines
            # fifth, get holes' coordinates
            self.origin_left(s, self.h2w)
            ls_total, ls = length_plus(self.lx, self.ly)
            self.f_left(ls)
            lp = self.hole_pos(ls_total)
            self.depend_left(lp)

            # repeat for the right side of waveguide
            self.origin_right(s, self.h2w)
            rs_total, rs = length_plus(self.rx, self.ry)
            self.f_right(rs)
```

```
            rp = self.hole_pos(rs_total)
            self.depend_right(rp)
```